From single pixel to continental scale: using AVHRR and MODIS to study land surface parameters in mountain regions

Inauguraldissertation

der Philosophisch-naturwissenschaftlichen Fakultät

der Universität Bern

vorgelegt von

Fabio Matteo Andrea Fontana

von Bruzella, TI

Leiter der Arbeit:

Dr. Stefan Wunderle

Geographisches Institut, Universität Bern

From single pixel to continental scale: using AVHRR and MODIS to study land surface parameters in mountain regions

Inauguraldissertation

der Philosophisch-naturwissenschaftlichen Fakultät

der Universität Bern

vorgelegt von

Fabio Matteo Andrea Fontana

von Bruzella TI

Leiter der Arbeit:

Dr. Stefan Wunderle

Geographisches Institut, Universität Bern

Von der Philosophisch-naturwissenschaftlichen Fakultät angenommen.

Bern, den 15. Oktober 2009   Der Dekan:

Prof. Dr. U. Feller

To my parents, for giving me the motivation, knowledge, and support needed to succeed; to Luzia, for the walk along the river and the wonderful years that followed.

Summary

The significance of mountain environments for the Earth's system has been widely recognized. Due to their particular sensitivity to changes in the climatic system, mountain regions have gained increasing attention in the global climate change discussion. In this regard, satellite remote sensing was identified as an important part of the monitoring strategies, since it can provide information on various land surface parameters in these areas on a wide range of spatial and temporal scales.

In this context, this thesis makes a contribution and revises the applicability of two medium spatial resolution satellite sensors, AVHRR and MODIS, for studies of land surface parameters in mountain regions on various spatial scales. The AVHRR sensor was chosen in view of its unique value for long-term climate impact studies. The MODIS sensor, as a newer generation sensor specifically designed for, inter alia, terrestrial applications, was chosen since it provides the opportunity for observations at higher spatial and spectral resolution compared to AVHRR. The focus was thereby entirely set on mountain vegetation as well as snow and ice, as these three land surface types belong to the most important components of many mountain environments.

However, complex topography significantly affects the quality of satellite data, since observed targets are displaced depending on their elevation and the viewing geometry at the time of observation. This displacement can be corrected for through the process of orthorectification. With regard to the generation of satellite-based climate data records in mountain regions, the benefit obtained from such a correction for the quality of AVHRR-derived land surface parameter datasets was, therefore, quantified. This was done based on maximum Normalized Difference Vegetation Index (NDVI) composite data at 1 km, 4 km, 5 km, and 8 km spatial resolution in August 1989, 1990, and 2001 to 2003. Distinct differences between orthorectified and non-orthorectified NDVI composites were obtained at various spatial scales, even though they were reduced for coarse resolution data. Apart from large differences at single-pixel scale, systematic average positive biases were identified in the non-orthorectified case at regional scale. A validation with accurately georeferenced composite data from the MODIS sensor revealed the high accuracy of the orthorectified NDVI com-

posites and emphasized the great importance of orthorectification for data quality in rugged terrain. Neglecting the terrain displacement effect may lead to important biases and additional noise in time series at various spatial scales. In addition, uncertainties due to the AVHRR Global Area Coverage (GAC) sampling scheme were analyzed with regard to the future use of GAC-based NDVI datasets in studies of vegetation photosynthetic activity in mountain regions. Uncertainties due to the GAC sampling scheme were found to introduce a systematic average positive bias, which can at least partially explain the systematic average positive biases we observed relative to our results in AVHRR GAC-based composites from the Global Inventory Modeling and Mapping Studies (GIMMS) and Polar Pathfinder (PPF) datasets. These results suggest that GAC-based NDVI datasets should be used with caution in future studies of vegetation dynamics in mountain regions.

With respect to the need for ground validation of satellite-derived surface parameters in mountain regions, the ability to track grassland growth phenology in the Swiss Alps with AVHRR NDVI time series at 1 km spatial resolution was evaluated. Validation was performed with in situ measurements at 15 alpine and subalpine grassland sites for the period from 2001 to 2005. Three grassland growth parameters were investigated: Melt-Out (MO), Start Of Growth (SOG), and End Of Growth (EOG). We estimated these phenological dates from yearly NDVI time series by identifying dates, where certain fractions (thresholds) of the maximum annual NDVI amplitude were crossed for the first time. For this purpose, the NDVI time series were smoothed using two common approaches (Fourier adjustment or alternatively Savitzky-Golay filtering). Additional validation was performed with data from two newer generation sensors, MODIS and VEGETATION. All remote sensing NDVI time series were highly correlated with single point ground measurements and showed similar thresholds, and therefore accurately represented growth dynamics of alpine grassland. For our purpose, the Fourier adjustment algorithm created higher quality NDVI time series than the Savitzky-Golay filter, since latter appeared to be more sensitive to short-term fluctuations in NDVI time series. Findings show that the application of various thresholds to NDVI time series allows the observation of the temporal progression of vegetation growth at the selected alpine grassland sites with high consistency. Hence, we believe these results help to better understand large-scale vegetation growth dynamics above the tree line in the European Alps.

Finally, with regard to the importance of snow and ice for the hydrological cycle and the surface energy balance in many mountain environments, interannual variations of perennial snow and ice (PSI) in nine mountain regions of interest (ROI) were quantified. For this purpose, we used a novel MODIS dataset processed at the Canada Centre for Remote Sensing (CCRS). The dataset covers the Arctic circumpolar area at 250 m spa-

tial resolution in all seven land bands (MODIS bands B1-B7) between 2000 and 2008. PSI extent was found to undergo significant interannual variations depending on the ROI. For some ROIs, strong negative relationships between PSI extent and positive degree-days (threshold 0°C) during the summer months were obtained, which may in part be explained by the strong snow-albedo feedback in mountain regions. Furthermore, PSI extent was highly correlated with net glacier mass balances in the European Alps and Scandinavia, which showed that MODIS-derived PSI extent at 250 m spatial resolution could serve as an indicator of net glacier mass balances in these areas. Comparison of PSI extent with two commonly used land surface classifications (LSC) in 2000 and 2005 revealed clear misrepresentation of PSI extent in both LSCs. With regard to the use of LSCs to set up boundary conditions for climate and land surface process models, this is a potential source of error to be investigated in future studies.

In summary, it was shown that medium spatial resolution satellite sensors such as the AVHRR and the MODIS are a valuable source of information for studies of land surface parameters in mountain regions. Where available at the full spatial resolution of 1 km, data from the AVHRR uniquely enable the detection and analysis of long-term trends and variations of land surface features in mountain regions. The novel MODIS processing technology developed at the CCRS can, if the MODIS sensor continues to operate until the end of 2009, provide a decade-long dataset at a high spatial resolution in accordance with the requirements of the Global Climate Observing System (GCOS). Together, these sensor systems bare great potential to increase our understanding of complex and sensitive mountain environments in the context of the global climate change discussion.

Contents

List of Figures

List of Tables

Abbreviations

Institutions, scientific programs and projects

CCRS	Canada Centre for Remote Sensing
CEOS	Committee on Earth Observing Satellites
CLASS	Comprehensive Large Array data Stewardship System
CTI	Canadian Centre for Topographic Information
DAAC	Distributed Data Archive Center
DLR	The German Aerospace Center
EC	European Commission
ECMWF	European Centre for Medium Range Weather Forecasts
EOS	Earth Observing System
ESA	European Space Agency
FAO	Food and Agriculture Organisation
FU	Freie Universität Berlin
GCOS	Global Climate Observing System
GIMMS	Global Inventory Modeling and Mapping Studies
GLIMS	Global Land Ice Measurements from Space
IMIS	Interkantonales Mess- und Informationssystem
IGBP	International Geosphere-Biosphere Programme
IPY	International Polar Year
IYM	International Year of Mountains
JRC	Joint Research Centre
LCCS	Land Cover Classification System
LP DAAC	Land Processes Distributed Active Archive Center
NARR	North American Regional Reanalysis

NESDIS	National Environmental Satellite Data and Information Service
NOAA	National Oceanic and Atmospheric Associations
NSIDC	National Snow and Ice Data Centre
PAL	Pathfinder AVHRR Land
POES	Polar Orbiting Environmental Satellites
PPF	Polar Pathfinder
PPS	Polar Platform System
RSGB	Remote Sensing Research Group Bern
SAFNWC	Satellite Application Facility to support Nowcasting and very ShortRange Forecasting
SLF	Swiss Federal Institute for Snow and Avalanche Research
UNCED	United Nations Conference on Environment and Development
UNEP	United Nations Environment Programme
WGMS	World Glacier Monitoring Service
WMO	World Meteorological Organization

Variables and parameters

α	Sensor scan angle
β	Satellite elevation angle
γ	Geocentric angle between satellite and pixel location
b_n	Net glacier mass balance
CI	Cloudiness Index
CV	Coefficient of Variation
EOG	End of Growth
ECV	Essential Climate Variable
f	Fourier series
FOV	field of view
FPAR	Fraction of Absorbed Photosynthetically Active Radiation
h	certain surface elevation
i	Compositing interval
IFOV	Instantaneous Field Of View
LAI	leaf area index
MO	Melt-out

$\overline{OD}$	Mean temporal offset in days
NDSI	Normalized Difference Snow Index
NDVI	Normalized Difference Vegetation Index
p	Summed power of NDVI composites
P	Percentiles
PSI	Perennial Snow and Ice
r	Correlation Coefficient
R	Reflectance
SCA	Snow Covered Area
SOG	Start of Growth
σ	Standard deviation
SZA	Sun Zenith Angle
T	Temperature
th	Threshold
VZA	View Zenith Angle
W	Weights in Fourier adjustment
Δx	Terrain displacement

Satellites and satellite sensors

ASTER	Advanced Spaceborne Thermal Emission and Reflection Radiometer
AVHRR	Advanced Very High Resolution Radiometer
ENVISAT	Environmental Satellite
MERIS	Medium Resolution Imaging Spectrometer
METOP	Meteorological Operational Satellite System
MODIS	Moderate Resolution Imaging Spectroradiometer
MSS	Multispectral Scanner
SPOT	Système Pour l'Observation de la Terre
TIROS	Television and Infrared Observation Satellite
TM	Thematic Mapper
VGT	VEGETATION

Other abbreviations

ACA	Arctic Circumpolar Area

BI	Bilinear Interpolation
BISE	Best Index Slope Extraction
BRDF	Bidirectional Reflectance Distribution Function
CAPS	Canadian AVHRR Processing System
CASPR	Cloud and Surface Parameter Retrieval
DEM	Digital Elevation Model
EASE	Equal Area Scalable Earth
GAC	Global Area Coverage
GCM	Global Circulation Model
GCPs	Ground Control Points
GLC	Global Land Cover
GSHHS	Global Self-consistent, Hierarchical, High-resolution Shoreline
HRPT	High Resolution Picture Transmission
LAC	Local Area Coverage
LAEA	Lambert Azimuthal Equal Area
LCC	Lambert Conformal Conic
LSC	Land Surface Cassifications
MEDOKADS	Mediterranean Extended Daily One Kilometer AVHRR Data Set
MVC	Maximum Value Composite
NN	Nearest Neighbor
RCM	Regional Circulation Model
ROI	Regions of Interest
SD	Solar Diffuser
SDSM	Solar Diffuser Stability Monitor
SIN	Sinusoidal
SM	Status Map
SPARC	Separation of Pixels Using Aggregated Rating over Canada
SRF	Spectral Response Function
TG	Time Grid
TOA	Top Of Atmosphere

Chapter 1

Introduction

1.1 Overview

Mountain regions are an important component of the Earth's system from a wide range of environmental and socioeconomic aspects. To name a few, mountain regions greatly influence the global hydrological cycle (Viviroli et al., 2007), affect large scale atmospheric circulation patterns (Whiteman, 2000), are characterized by high levels of biodiversity (Körner and Spehn, 2002), and serve as recreation areas for an increasing number of people (Godde et al., 2000). In addition, while covering approximately 25% of the Earth's continental surface (Kapos et al., 2000), they directly provide resources essential for living, such as fresh water, to one-fourth of the world's population and indirectly to more than half (Beniston et al., 1997). Figure 1.1 gives an impression of the large continental area covered by mountain areas, which are widely dispersed over the entire globe (marked in red color). The complexity of the topography was used as an indicator of mountain regions and extracted from a global digital elevation model (DEM; see the figure caption for more information).

The importance of mountain regions has, however, only recently been emphasized. According to Beniston (2003), it was first in 1992 at the United Nations Conference on Environment and Development (UNCED) in Rio de Janeiro that the importance of mountain regions was officially recognized and documented in the final agreement, called "Agenda 21", negotiated by the participating governments (United Nations, 1992). In chapter 13 of Agenda 21 this is highlighted as follows (modified from United Nations, 1992):

> *Mountains are an important source of water, energy and biological di-*
> *versity. As a major ecosystem representing the complex and interrelated*
> *ecology of our planet, mountain environments are essential to the survival*

of the global ecosystem but are rapidly changing and highly vulnerable to human and natural ecological imbalance. Hence, the proper management of mountain resources and socioeconomic development of the people deserves immediate action.

As a consequence, studies of mountain environments have become increasingly important within the ongoing global change discussion. Research frameworks and initiatives such as the Mountain Research Initiative (MRI) were set up with the aim of designing strategies to identify signs of global change in mountain environments and of working towards sustainable resource management at various spatial scales (Becker, 2001). With the International Year of Mountains (IYM) in 2002 additional notice was attracted to the topic.

There is now global consensus that changes in the climatic system projected for the future will significantly affect mountain environments and, as a direct consequence, surrounding low-lands depending on mountain-based resources (Christensen et al., 2007). These concerns are affirmed with regard to mountain regions repeatedly being
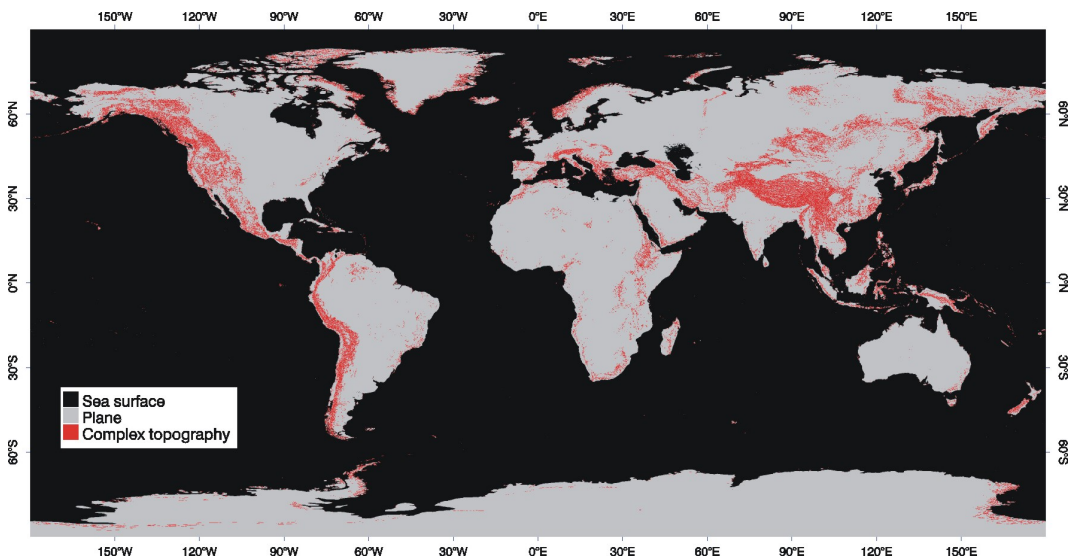
Figure 1.1: *Continental areas characterized by complex topography (marked in red) based on a 1 km spatial resolution digital elevation model (DEM) aggregated to 0.1°. Five morphometric features (peak, ridge, pass, channel, and pit) were combined in one class (red) to represent mountain regions. These were determined by calculating the slope and curvatures of the surface. Spatially homogeneous high elevation areas such as Greenland and Antarctica are not considered by this approach. The DEM was downloaded from http://www.ngdc.noaa.gov/mgg/topo/globe.html; date: August 20, 2009. Image design by F. Hüsler.*

described as particularly sensitive to such changes (Huber et al., 2005). Moreover, modifications in general temperature and precipitation patterns may be enhanced in mountain areas such as the European Alps (Giorgi et al., 1997; Wanner et al., 1997), the Andes (Urrutia and Vuille, 2009), or the Rocky Mountains (Fyfe and Flato, 1999).

The enhanced sensitivity to changes in the climatic system makes mountain regions highly suitable for climate change impact studies: strong altitudinal gradients lead to a sequence of different climatic zones on small horizontal scales, which is otherwise only observed over scales of hundreds to thousands of kilometers. As a result, global change phenomena occur and may be studied at relatively small spatial scales (Beniston, 2003). In addition, due to mountain regions being widely dispersed over the globe, comparative studies can provide valuable information on varying responses of different (mountain) regions to changes in the climate system.

Among a multitude of possible climate change effects, modifications in the hydrological cycle are predicted to become particularly strong due to the involvement of seasonal snow cover and glaciers: as key players in the hydrological cycle in many mountain regions, snow cover and glaciers naturally serve as a storage for water in the frozen state and buffer seasonal and interannual water shortage in mountains and far beyond (Viviroli et al., 2003; Diaz et al., 2003). As a result, minor (future) changes in temperature, determining whether precipitation falls as snow or rain in certain areas or elevation zones, will significantly affect seasonal run-off patterns by changing the amount of water temporarily retained in these reservoirs. Modified seasonal run-off patterns, again, are likely going to – and have already been observed to – have severe environmental and socioeconomic consequences in some regions (Barnett et al., 2005). Furthermore, snow cover and glaciers exert large influence on climate at various spatial scales because of the typically high albedo and cooling of the atmosphere (Groisman and Davies, 1999; Kotlarski, 2007; UNEP, 2007) and thus directly or indirectly act on other components of mountain ecosystems and vice versa. For example, snow cover largely affects mountain vegetation through the influence of the physical snowpack characteristics on micro-environmental conditions of many alpine plant species (Pauli et al., 2003) and determines the boundary conditions for the annual growth cycle (Cayan et al., 2001). The latter effect is of particular importance with regard to future climate change scenarios: changes in snow cover duration, i.e. changes in the start (and/or possibly end) of the growing season, likely result in modifications of the species composition in alpine plant habitat zones, since various plant species react differently to altered growth conditions (Keller et al., 2005). Similarly, climate change is known to affect the growing season length in areas not dominated by seasonal snow cover due to the close dependence of plant phenology on air temperature variations (Menzel and Fabian, 1999; Stöckli and Vidale, 2004). Accurate knowledge

about the on- and offset of seasonal vegetation growth is generally a prerequisite for the assessment of land surface–atmosphere interactions (Sellers et al., 1996b,a), because vegetation significantly influences the surface energy budget mainly through the contributions of evapotranspiration and albedo (Bonan, 2000). Moreover, vegetation cover plays a key role in providing nourishment resources for mountain population, livestock farming, and wild animals, as well as in helping to reduce soil erosion and to decrease the risk of natural hazards such as landslides (Beniston, 2003).

Together, vegetation, snow, and glaciers represent critical components of many mountain environments that are strongly involved in cycles of energy and matter through a large number of complex feedback mechanisms on various spatial scales (Denman et al., 2007; Lemke et al., 2007). In this respect, studies of past, present, and future variations of these land surface types in mountain areas are essential and deserve particular attention within the ongoing global climate change discussion. The following section (Section 1.2) gives an overview of different monitoring methodologies, which all aim at increasing our understanding of sensitive mountain environments. The focus is thereby entirely set on vegetation, snow, and glaciers due to their importance for many mountain regions as addressed above. For a comprehensive overview of possible climate change impacts from a wide range of other environmental *as well as* socioeconomic aspects, the author refers to Huber et al. (2005) and Beniston (2003).

1.2 Quantifying environmental changes in mountain regions

Each of the three subsequently discussed approaches, in situ observations, modelling, and satellite observations, has its own strengths and weaknesses. Exploiting the advantages of each methodology will increase our knowledge of sensitive mountain environments.

1.2.1 In situ measurements

In situ observations can, where available, provide valuable information on various surface parameters in mountain areas. Regarding vegetation systems, in situ data include information on the phenology of plant species (obtained from phenological networks; Studer et al., 2005), on changes in their abundance over time (Grabherr et al., 1994; Walther et al., 2005), on their behavior under certain climatic conditions (Signabieux and Feller, 2008), on the involvement of vegetation in ecosystem fluxes of energy and matter (Rogiers et al., 2008), or on vegetation biomass (Yang et al., 2009). Combin-

ing in situ data on snow cover, temperature, precipitation, and vegetation growth can give interesting insights into possible future patterns of alpine vegetation dynamics (Jonas et al., 2008, see also Chapter 4). Other possible applications of in situ measurements in mountain environments include the assessment of long-term variability of snow cover (Stähli and Gustafsson, 2006), the evaluation of the spatial variability in snow water equivalent (Anderton et al., 2004), or, in synergy with space borne observations, the mapping of snow depth (Foppa et al., 2007b). In the context of glacier monitoring, in situ data primarily provide information on the mass and surface energy balance of glaciers, which can be used to quantify the dynamic response of glaciers to changing climatic conditions (Zemp et al., 2009). Furthermore, in situ data may be used as input for high resolution RCMs as described below, or used as a source of validation for surface parameters retrieved from satellite data (cf. Chapter 4).

Even though in situ datasets in mountain regions extend back in time (e.g. phenological networks in the Swiss Alps back to 1951; Studer et al., 2005), their usefulness may be limited due to the sparse spatial coverage often observed for measurement networks: while measurement networks for variables such as snow cover are relatively dense in some mountain regions, e.g. the European Alps, this is certainly not the case in other, more remote, areas such as the Himalaya. Another drawback is their limited explanatory power in the spatial domain. Given the topographical complexity with abruptly changing climatic conditions due to slope, aspect, and elevation variations, data obtained at a measurement site may only be representative at local scale, i.e. of the site itself and its immediate surroundings. Measured parameters can be interpolated between the sites, but this will likely lead to errors due to the virtual impossibility to capture the highly variable mountain environments.

1.2.2 Modelling approaches

Information provided here follows considerations made by Bugmann et al. (2007), who provide a review of modelling methodologies for biophysical impact studies in mountain biosphere reserves. Modelling approaches may be separated into two classes: models providing scenarios for global change over large time scales (e.g. climate models), and models to project the impacts of these scenarios to the behavior of a mountain environment and its major components.

As for the climate models, projections of future climate change specific for mountain regions are of major importance. The problem is, however, that in Global and even Regional Circulation Models (GCM and RCM, respectively) topography is greatly smoothed and, as a result, the spatial information is too coarse to adequately reflect small-scale processes governing climatic conditions in many mountains (Christensen

et al., 2007). In order to reduce limitations due to the complex topography, statistical downscaling techniques may be used to obtain climate change information for mountainous areas (Hanssen-Bauer et al., 2005). For the simulation of specific processes such as precipitation and surface runoff, RCMs at very high spatial resolutions of only a few kilometers are available (e.g. Walser and Schär, 2004), but their use for simulations at large spatiotemporal scales is limited due to computational considerations (Christensen et al., 2007).

Concerning the impact modelling, there is a wide variety of models available. Vegetation systems may be modelled in terms of vegetation cover dynamics (Bugmann, 2001), growth phenology with regard to the determination of the start and end of the growing season (Stöckli et al., 2008), species distribution (Hirzel et al., 2002), or also annual net primary productivity of mountain ecosystems and its correlation with precipitation and temperature variations (Fagre et al., 2005). For snow cover, they range from simple models, relating snow melt to air temperature (Rango and Martinec, 1995), to complex models, which attempt to describe physical surface processes on local to regional scales (Bartelt and Lehning, 2002). Finally, regarding glacier systems, impact models commonly aim at describing the glacier mass balance or the dynamic response of the glacier's spatial extent to climatic conditions (Oerlemans, 2001).

While these models provide valuable insight into various environmental processes, particularly on large time scales (e.g. >100 years), they may still rely on a set of assumptions and auxiliary data from in situ measurements or remote sensing.

1.2.3 Satellite observations

As mentioned earlier, methodologies using in situ data are concerned with the problem of measurement network densities and potentially low representativeness of the measurements in the spatial domain. Modelling approaches are either limited by the coarse model resolution, underlying model assumptions, or by exceeding computational requirements for large scale applications at high spatial resolution. Finally, while satellite remote sensing (hereafter referred to as 'remote sensing') cannot replace modelling or field based research, it certainly complements these methodologies and contributes significantly to the understanding of various phenomena to be studied on a wide range of temporal and spatial scales.[1] It was, therefore, defined as a key component of global climate monitoring by the World Meteorological Organization (WMO, 2004). The major advantage of remote sensing is that it can provide information on

---

[1]As a complement to spaceborne remote sensing, airborne and terrestrial remote sensing systems may be used for some applications. The discussion of the contributions made by these systems is, however, beyond the scope of this work.

surface parameters even in remote and hardly accessible mountain areas (Weiss and Walsh, 2009).

Regarding the monitoring of vegetation parameters, sensors such as the Landsat Thematic Mapper (TM) with a high spatial resolution (30 m) can provide information on vegetation communities and other land cover characteristics (Frank, 1988). The problem of high spatial resolution sensors is their low ground track repeat cycle (e.g. 16 days for Landsat TM). This is the reason why their use for the monitoring of possibly rapidly changing surface parameters, such as vegetation photosynthetic activity after snow melt in spring and early summer, is limited. Medium spatial resolution satellite sensors with higher temporal (ideally daily) but lower spatial resolution ($\geq$250 m) are, therefore, preferred for investigations of the temporal progression of seasonal vegetation development, e.g. using time series of the Normalized Difference Vegetation Index (NDVI; Tucker and Sellers, 1986, see Chapters 3 and 4). Similarly, these sensors are employed for the analysis of possibly transient phenomena such as mountain snow cover (Foppa et al., 2004; Tekeli et al., 2005, Chapter 5), even though high spatial resolution sensors may be used for validation purposes (Foppa et al., 2007a). With respect to the monitoring of mountain glaciers, sensors such as the Advanced Spaceborne Thermal Emission and Reflection Radiometer (ASTER) with a high spatial resolution (max. 15 m), again, are the data source of choice and are, for example, used to establish global glacier inventories as part of the Global Land Ice Measurements from Space (GLIMS) initiative (Kargel et al., 2005).

The use of remote sensing data for studies of land surface parameters in mountain regions implies, however, considerable difficulties, since significant topography is a well known source of uncertainty in satellite data. To meet the requirements in terms of data geometric and radiometric accuracy defined by the Global Climate Observing System (GCOS) for systematic satellite observations (GCOS, 2006, Appendix 2), additional attention during data processing and analysis is required. This will be the topic of Chapter 2, where challenges imposed on remote sensing applications in mountain regions are discussed in more detail.

In the context of the global climate change discussion, it is particularly interesting to quantify and analyze long-term variations of surface parameters on large spatial scales. The sensor, which can uniquely provide long-term coverage (1981−present) at medium spatial (1 km) and high temporal resolution (daily) is the Advanced Very High Resolution Radiometer (AVHRR) onboard the National Oceanic and Atmospheric Association (NOAA) Polar Orbiting Environmental Satellites (POES) and the European Organisation for the Exploitation of Meteorological Satellites (EUMETSAT) Meteorological Operational-A (METOP-A) satellite. Even though AVHRR was originally designed

for meteorological and oceanographic purposes, its usefulness for other, e.g. terrestrial, applications became apparent shortly after launch (Justice et al., 1985; Gutman, 1988; Liu et al., 1986). The AVHRR sensor has since then proven to be an invaluable source of information for long-term investigations in various fields of research. It will by the end of the projected operation time in 2020 provide a nearly 40 years long time series for the use in climate impact studies. Given the importance to quantify long-term variation of various surface parameters in mountain regions, the AVHRR sensor system was selected as a basic data source for this thesis (see Section 2.3 for a description of the AVHRR sensor system).

In view of to the need for improved satellite data for terrestrial applications, new medium spatial resolution sensors tailored for global change research were launched during the past decade. As an example, the Moderate Resolution Imaging Spectroradiometer (MODIS) has been operational since 2000 and has provided interesting insight into the Earth's system as a whole, with emphasis on interactions between the atmosphere, land, and oceans (Barnes et al., 1998). In addition to a vast range of possible applications, MODIS data may extend or complement AVHRR time series or serve as a source of validation of recent AVHRR data with regard to the long-term analysis of AVHRR-based long-term climate data records (see Chapter 4). The MODIS sensor was therefore, chosen as the second basic data source of this thesis (see Section 2.4 for a description of the MODIS sensor system).

1.3   Aims of the PhD thesis

As outlined above, remote sensing data can provide valuable information for studies of surface parameters in mountain regions. Imbedded in this context, the overall aim of the thesis is

> *to revise the applicability of AVHRR and MODIS imagery for studies of*
> *land surface parameters in mountain regions on various spatial scales and*
> *to make a contribution to the understanding of sensitive mountain regions*
> *in the context of the global climate change discussion.*

In more detail, the aims of the thesis may be summarized as follows:

- at local and regional scale: to quantify the impact of topography on the quality of long-term AVHRR climate data records with regard to the GCOS geolocation accuracy requirements, and to emphasize the necessity to correct for it. This may represent an important step towards the generation of high quality long-term climate data records for mountain regions based on AVHRR data archives.

- at local scale: to extract information on the seasonal progression of alpine grass-land growth from time series of AVHRR data, and to perform a validation with newer generation satellite sensors as well as with in situ measurements of vege-tation development. This should enhance our confidence in the use of medium spatial resolution sensors for such applications in rugged terrain and improve our understanding of vegetation phenology with regard to the analysis of long-term vegetation data in complex alpine environments.

- at regional to hemispherical scale: to use novel MODIS data at 250 m spatial resolution to quantify interannual variability of perennial snow and ice cover in several mountain regions within the Arctic circumpolar area. This should provide interesting insight into variations of these two key players of mountain environ-ments, particularly with respect to their involvement in the hydrological cycle and interactions with regional climate.

Achieving these aims using the two selected sensor systems will help to increase our understanding of sensitive mountain environments with regard to the projected future climate change scenarios.

1.4   Outline of the PhD thesis

Following above considerations, the thesis is structured as follows:

- **Chapter 1** gave a general introduction to the scientific background and frame-work of this thesis. In particular, the importance of mountain regions in the global environment was highlighted. Methodologies available to study these sensitive environments were presented with a focus on vegetation, snow, and ice.

- The focus of **Chapter 2** will be on a number of issues relevant for the processing and the interpretation of remote sensing data in mountain regions. In addition, an overview of the sensor systems employed in this thesis, AVHRR and MODIS, will be given, together with a description of the datasets utilized.

- **Chapter 3** presents the results of a methodological study at local to regional scale in the Mackenzie mountain range in Northwestern Canada, namely the quantification of the influence of geometric distortions on the quality of long-term AVHRR NDVI data. The necessity to correct for these distortions is em-phasized with regard to the generation of high quality long-term climate data records in accordance with geolocation accuracy requirements defined by GCOS.

In addition, the applicability of two commonly used AVHRR datasets for studies of mountain regions is revised.

- Given the need to validate satellite derived surface parameters with ground-measurements, **Chapter 4** describes a comparative study of satellite and ground based phenology at 15 alpine grassland sites in the Swiss Alps. Time series of AVHRR NDVI data are compared to in situ measurements of alpine grassland growth to obtain information on the quality of the satellite-derived parameter at local scale. Two additional, newer generation, satellite sensors are used for validation in this study: MODIS and Système Pour l'Observation de la Terre (SPOT) VEGETATION. This study is relevant with regard to the analysis of long-term variations in vegetation photosynthetic activity in the European Alps.

- In view of the importance of snow and ice for many mountain environments, interannual variations of perennial snow and ice extent in nine mountain regions of interest are quantified in **Chapter 5** based on MODIS data. The dataset used covers the Arctic circumpolar area between 2000 and 2008 at 250 m spatial resolution. In addition, MODIS data are employed to validate the spatial extent of perennial snow and ice in two common land cover classifications. This is of particular importance with regard to the application of land cover classification to set up boundary conditions in climate and land surface process models.

- An overall summary of the results obtained within this project is provided in **Chapter 6**, together with concluding remarks and an overview of forthcoming steps.

References

Anderton, S. P., S. M. White, and B. Alvera (2004). Evaluation of spatial variability in snow water equivalent for a high mountain catchment. *Hydrological Processes* **18**, 435–453.

Barnes, W. L., T. S. Pagano, and V. V. Salomonson (1998). Prelaunch characteristics of the Moderate Resolution Imaging Spectroradiometer (MODIS) on EOS-AM1. *IEEE Transactions on Geoscience and Remote Sensing* **36**, 1088–1100.

Barnett, T. P., J. C. Adam, and D. P. Lettenmaier (2005). Potential impacts of a warming climate on water availability in snow-dominated regions. *Nature* **438** (7066), 303–309.

Bartelt, P. and M. Lehning (2002). A physical SNOWPACK model for the Swiss avalanche warning system. Part I: numerical model. *Cold Regions Science and Technology* **35**, 123–145.

Becker, A. Bugmann, H. (2001). Global Change in Mountain Regions: The Mountain Research Initiative. IGBP Report 49 / GTOS Report 28 / IHDP Report 13. Stockholm, Sweden: Royal Swedish Academy of Sciences.

Beniston, M. (2003). Climatic Change in Mountain Regions: A Review of Possible Impacts. *Climatic Change* **59** (1), 5–31.

Beniston, M., H. F. Diaz, and R. S. Bradley (1997). Climatic Change at High Elevation Sites: An Overview. *Climatic Change* **36** (3/4), 233–251.

Bonan, G. (2000). *Ecological Climatology: Concepts and application*. Cambridge University Press.

Bugmann, H. (2001). A Review of Forest Gap Models. *Climatic Change* **51** (3), 259–305.

Bugmann, H., A. Bjornsen Gurung, F. Ewert, W. Haeberli, A. Guisan, D. Fagre, A. Kääb, and GLOCHAMORE participants (2007). Modeling the Biophysical Impacts of global Change in Mountain Biosphere Reserves. *Mountain Research and Development* **27** (1), 66–77.

Cayan, D. R., S. A. Kammerdierner, M. D. Dettinger, J. M. Caprio, and D. H. Peterson (2001). Changes in the Onset of Spring in the Western United States. *Bullettin of the American Meteorological Society* **82**, 399–415.

Christensen, J., B. Hewitson, A. Busuioc, A. Chen, X. Gao, I. Held, R. Jones, R. Kolli, W.-T. Kwon, R. Laprise, V. Magana, L. Rueda, L. Mearns, C. Menendez, J. Räisänen, A. Rinke, A. Sarr, and P. Whetton (2007). *Regional Climate Projections. In: Climate Change 2007: The Physical Science Basis. Contribution of Working Group I to the Fourth Assessment Report of the Intergovernmental Panel on Climate Change*. Cambridge University Press, Cambridge, United Kingdom and New York, NY, USA.

Denman, K. L., G. Brasseur, A. Chidthaisong, P. Ciais, P. M. Cox, R. E. Dickinson, D. Hauglustaine, C. Heinze, E. Holland, D. Jacob, U. Lohmann, S. Ramachandran, P. L. da Silva Dias, S. C. Wofsy, and X. Zhang (2007). Couplings Between Changes in the Climate System and Biogeochemistry. In S. Solomon, D. Qin, M. Manning, Z. Chen, M. Marquis, K. B. Averyt, M. Tignor, and H. L. Miller (eds.), *Climate Change 2007: The Physical Science Basis. Contribution of Working Group I to the Fourth*

Assessment Report of the Intergovernmental Panel on Climate Change. Cambridge University Press, Cambridge, United Kingdom and New York, NY, USA.

Diaz, H. F., M. Grosjean, and L. Graumilch (2003). Climate variability and change in high elevation regions: past, present and future. *Climatic Change* **59**, 1–4.

Fagre, D., S. Running, R. Keane, and D. Peterson (2005). Assessing climate change effects on mountain ecosystems using integrated models: A case study. In U. M. Huber, H. K. M. Bugmann, and M. A. Reasoner (eds.), *Global Change and Mountain Regions.* Dordrecht, The Netherlands: Springer.

Foppa, N., A. Hauser, D. Oesch, S. Wunderle, and R. Meister (2007a). Validation of operational AVHRR subpixel snow retrievals over the European Alps based on ASTER data. *International Journal of Remote Sensing* **28** (21), 4841–4865.

Foppa, N., A. Stoffel, and R. Meister (2007b). Synergy of in situ and space borne observation for snow depth mapping in the Swiss Alps. *International Journal of Applied Earth Observation and Geoinformation* **9** (3), 294–310.

Foppa, N., S. Wunderle, A. Hauser, D. Oesch, and F. Kuchen (2004). Operational sub-pixel snow mapping over the Alps with NOAA-AVHRR data. *Annals of Glaciology* **38**, 245–252.

Frank, T. (1988). Mapping dominant vegetation communities in the Colorado Rocky Mountain Front Range with Landsat TM. *Photogrammetric Engineering and Remote Sensing* **54** (12), 1727–1734.

Fyfe, J. C. and G. M. Flato (1999). Enhanced Climate Change and Its Detection over the Rocky Mountains. *Journal of Climate* **12** (1), 230–243.

GCOS (2006). Systematic Observation Requirements for Satellite-based Products for Climate: Supplemental details to the satellite-based component of the Implementation plan for the Global Observing System for Climate in support of the UNFCC. GCOS-107, WMO/TD-1338.

Giorgi, F., J. W. Hurrell, M. R. Marinucci, and M. Beniston (1997). Elevation Dependency of the Surface Climate Change Signal: A Model Study. *Journal of Climate* **10** (2), 288–296.

Godde, P., M. F. Price, and F. M. Zimmermann (eds.) (2000). *Tourism and Development in Mountain Regions*. CABI Publishing, Wallingford.

Grabherr, G., M. Gottfried, and H. Pauli (1994). Climate effects on mountain plants. *Nature* **369** (6480), 448–448.

Groisman, P. and T. Davies (1999). Snow cover and the climate system. In *Snow Ecology*. Cambridge University Press, Cambridge, UK.

Gutman, G. (1988). A simple method for estimating monthly mean albedo of land surfaces from AVHRR data. *Journal of Applied Meteorology* **27**, 973–988.

Hanssen-Bauer, I., C. Achberger, R. E. Benestad, D. Chen, and E. J. Forland (2005). Statistical downscaling of climate scenarios over Scandinavia. *Climate Research* **29** (3), 255–268.

Hirzel, A. H., J. Hausser, D. Chessel, and N. Perrin (2002). Ecological-niche factor analysis: How to compute habitat-suitability maps without absence data? *Ecology* **83**, 2027–2036.

Huber, U. M., H. K. M. Bugmann, and M. Reasoner (2005). *Global Change and Mountain Regions: An Overview of Current Knowledge.* Dordrecht, The Nederlands: Springer.

Jonas, T., C. Rixen, M. Sturm, and V. Stöckli (2008). How alpine plant growth is linked to snow cover and climate variability. *Journal of Geophysical Research - BioGeoSciences* **113**, –.

Justice, C. O., J. R. G. Townshend, B. N. Holben, and C. J. Tucker (1985). Analysis of the phenology of global vegetation using meteorological satellite data. *International Journal of Remote Sensing* **6** (8), 1271–1318.

Kapos, V., J. Rhind, M. Edwards, C. Ravilious, and M. F. Price (2000). Developing a Map of the Worlds Mountain Forests. In M. F. Price and N. Butt (eds.), *Forests in a Sustainable Mountain Environment: A state of knowledge report for 2000*, pp. 4–9. CAB International, Wallingford.

Kargel, J. S., M. J. Abrams, M. P. Bishop, A. Bush, G. Hamilton, H. Jiskoot, A. Kääb, H. H. Kieffer, E. M. Lee, F. Paul, F. Rau, B. Raup, J. F. Shroder, D. Soltesz, D. Stainforth, L. Stearns, and R. Wessels (2005). Multispectral imaging contributions to global land ice measurements from space. *Remote Sensing of Environment* **99** (1-2), 187–219.

Keller, F., S. Goyette, and M. Beniston (2005). Sensitivity analysis of snow cover to climate change scenarios and their impact on plant habitats in alpine terrain. *Climatic Change* **72**, 299–319.

Körner, C. and E. M. Spehn (2002). *Mountain Biodiversity. A global assessment*. Parthenon Publishing at CRC press.

Kotlarski, S. (2007). *A Subgrid Glacier Parameterisation for Use in Regional Climate Modelling*. Reports on earth system science (42/2007), Max Planck Institute for Meteorology.

Lemke, P., J. Ren, R. Alley, I. Allison, J. Carrasco, G. Flato, Y. Fujii, G. Kaser, P. Mote, R. Thomas, and T. Zhang (2007). Observations: Changes in Snow, Ice and Frozen Ground. In S. Solomon, D. Qin, M. Manning, Z. Chen, M. Marquis, K. B. Averyt, M. Tignor, and H. L. Miller (eds.), *Climate Change 2007: The Physical Science Basis. Contribution of Working Group I to the Fourth Assessment Report of the Intergovernmental Panel on Climate Change*. Cambridge University Press, Cambridge, United Kingdom and New York, NY, USA.

Liu, Z. K., S. Y. Zheng, and Q. Z. Zeng (1986). Snow survey from meteorological satellite images in the Qilian Mountain Basin in northwest China. *International Journal of Remote Sensing* **7** (10), 1335–1340.

Menzel, A. and P. Fabian (1999). Growing season extended in Europe. *Nature* **397** (6721), 659–659.

Oerlemans, J. (2001). *Glaciers and Climate Change*. Rotterdam, The Netherlands: Balkema.

Pauli, H., M. Gottfried, and G. Grabherr (2003). Effects of climate change on the alpine and nival vegetation of the Alps. *Journal of Mountain Ecology* **7**, 9–12.

Rango, A. and J. Martinec (1995). Revisiting the degree-day method for snowmelt computations. *Journal of the American Water Resources Association* **31**, 657–669.

Rogiers, N., F. Conen, M. Furger, R. Stöckli, and W. Eugster (2008). Impact of past and present land-management on the C-balance of a grassland in the Swiss Alps. *Global Change Biology* **14** (11), 2613–2625.

Sellers, P. J., S. O. Los, C. J. Tucker, C. O. Justice, D. A. Dazlich, G. J. Collatz, and D. A. Randall (1996a). A Revised Land Surface Parametrization (SiB2) for Atmospheric GCMs. Part II. The Generation of Global Fields of Terrestrial Biophysical Parameters from Satellite Data. *Journal of Climate* **9**, 706–737.

Sellers, P. J., D. Randall, G. Collatz, J. A. Berry, C. B. Field, D. A. Datzlich, C. Zhang, G. D. Collelo, and L. Bounoua (1996b). A Revised Land Surface Parametrization (SiB2) for Atmospheric GCMs. Part I: Model Formulation. *Journal of Climate* **9**, 676 – 705.

Signabieux, C. and U. Feller (2008). Effects of an extended drought period on grasslands at various altitudes in Switzerland: a field study. In J. F. Allen, E. Gantt, J. H.

Golbeck, and B. Osmond (eds.), *Photosynthesis. Energy from the Sun. 14th International Congress on Photosynthesis*, pp. 1375–1378. Springer.

Stähli, M. and D. Gustafsson (2006). Long-term investigations of the snow cover in a subalpine semi-forested catchment. *Hydrological Processes* **20**, 411–428.

Stöckli, R., T. Rutishauser, D. Dragoni, J. O'Keefe, P. E. Thornton, M. Jolly, L. Lu, and A. S. Denning (2008). Remote sensing data assimilation for a prognostic phenology model. *Journal of Geophysical Research* **113** (G04021), –.

Stöckli, R. and P. L. Vidale (2004). European plant phenology and climate as seen in a 20 year AVHRR land-surface parameter dataset. *International Journal of Remote Sensing* **25**, 3303–3330.

Studer, S., C. Appenzeller, and C. Defila (2005). Inter-Annual Variability and Decadal Trends in Alpine Spring Phenology: A Multivariate Analysis Approach. *Climatic Change* **73** (3), 395–414.

Tekeli, A. E., Z. Akyürek, A. Arda Sorman, A. Sensoy, and A. Ünal Sorman (2005). Using MODIS snow cover maps in modeling snowmelt runoff process in the eastern part of Turkey. *Remote Sensing of Environment* **97** (2), 216–230.

Tucker, C. J. and P. J. Sellers (1986). Satellite remote sensing of primary production. *International Journal of Remote Sensing* **7** (11), 1395–1416.

UNEP (2007). *Global outlook for snow and ice*. United Nations Environment Programme.

United Nations (1992, June 3-14). Earth Summit: Agenda 21. The United Nations Programme of Action from Rio. The final text of agreements negotiated by governments at the United Nations Conference on Environment and Development (UNCED), Rio de Janeriro, Brazil.

Urrutia, R. and M. Vuille (2009). Climate change projections for the tropical Andes using a regional climate model: Temperature and precipitation simulations for the end of the 21st century. *J. Geophys. Res.* **114**, –.

Viviroli, D., H. H. Duerr, B. Messerli, M. Meybeck, and R. Weingartner (2007). Mountains of the world, water towers for humanity: Typology, mapping, and global significance. *Water Resources Research* **43**, 1–13.

Viviroli, D., Weingartner R., and B. Messerli (2003). Assessing the Hydrological Significance of the Worlds Mountain. *Mountain Research and Development* **23** (1), 32–40.

Walser, A. and C. Schär (2004). Convection-resolving precipitation forecasting and its predictability in Alpine river catchments. *Journal of Hydrology* **288** (1-2), 57–73.

Walther, G. R., S. Beissner, and H. Pauli (2005). Trends in the upward shift of alpine plants. *Journal of Vegetation Science* **16**, 541–548.

Wanner, H., R. Rickli, E. Salvisberg, C. Schmutz, and M. Schuepp (1997). Global climate change and variability and its influence on Alpine climate-concepts and ob-servations. *Theoretical and Applied Climatology* **58** (3-4), 221–243.

Weiss, D. J. and S. J. Walsh (2009). Remote Sensing of Mountain Environments. *Geography Compass* **3** (1), 1–21.

Whiteman, C. D. (2000). *Mountain Meteorology. Fundamentals and applications*. Oxford University Press.

WMO (2004). Implementation Plan for the Global Observing System for Climate in Support of the UNFCCC. GCOS-9; available online at: http://www.wmo.ch/pages/prog/gcos/publications.

Yang, Y. H., J. Y. Fang, Y. D. Pan, and C. J. Ji (2009). Aboveground biomass in Tibetan grasslands. *Journal of Arid Environments* **73**, 91–95.

Zemp, M., M. Hoelzle, and W. Haeberli (2009). Six decades of glacier mass-balance observations: a review of the worldwide monitoring network. *Annals of Glaciology* **70**, 101–111.

Chapter 2

Observing mountains from space

2.1 General considerations

Remote sensing of land surface parameters in mountain regions does not differ from remote sensing elsewhere with respect to a basic underlying principle: land surface types may be discriminated based on their inherent spectral and emittance properties in certain portions of the electromagnetic spectrum (Lillesand et al., 2004). The benefit obtained from a remote sensing sensor thereby largely depends on its spectral resolution, which determines the sensor's capability to resolve spectral features of land surfaces. Figure 2.1 displays the optical properties of various Earth surfaces in the range between 0.4 μm and 2.0 μm, which covers most of the solar reflective part of the electromagnetic spectrum. As a reference, the spectral characteristics of the sensor systems used in this study, AVHRR and MODIS, are listed in Tables 2.1 and 2.2, respectively. Photosynthetically active vegetation (Figure 2.1, a), for example, is characterized by very low reflectance values in the red part of the electromagnetic spectrum (ca. 0.7 μm) due to the absorption of solar radiation by the leaf pigments involved in photosynthesis, and by increased reflectance in the near infrared portion of the spectrum (ca. 0.9 μm) due to reflection of incoming solar radiation at the leaf internal structures (Gitelson and Merzlyak, 1996). In contrast, snow and ice covered surfaces (Figure 2.1, c) are typically characterized by strong reflectance in the visible part of the spectrum (ca. 0.4-0.7 μm) and low reflectance in the short wave infrared part (ca. 1.5 μm; Dozier and Painter, 2004). Such differences in the reflective properties of a surface between certain wavelengths can be employed to compute spectral indices that give an indication of the abundance of a given land cover type within the area covered by a pixel. With regard to the monitoring of terrestrial vegetation, the Normalized Difference Vegetation Index (NDVI; Tucker, 1979) is the most commonly used index and serves as a measure of photosynthetic activity within a certain area (cf.

17
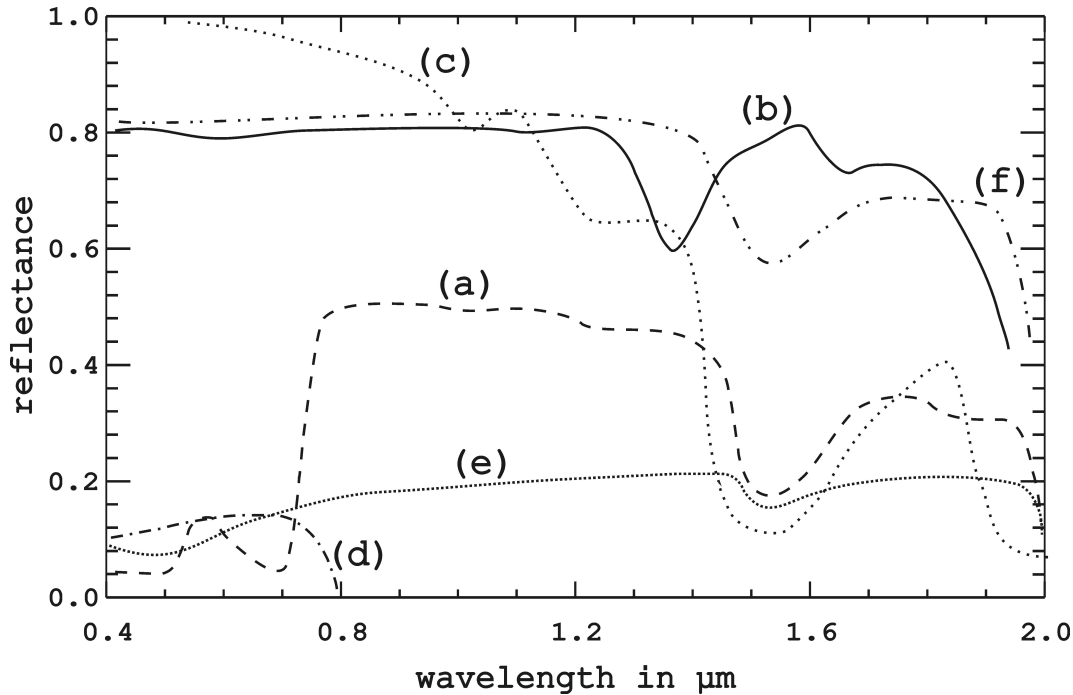
Figure 2.1: *Spectral signatures of different Earth surfaces. (a) Photosynthetically active vegetation, (b) salt flat, (c) snow, (d) water, (e) soil, and optically thick clouds (f). Given the importance to detect clouds in land surface applications, the spectral properties of an optically thick cloud are also provided (adopted and modified from Wildeisen, 2008, and references therein).*

Chapters 3 and 4). Concerning observations of snow and ice covered surfaces, the Normalized Difference Snow Index (NDSI; Salomonson and Appel, 2004) exploits the distinct spectral properties of snow and ice as described above and can be regarded as a measure of these land cover types within the sensor's field of view (cf. Chapter 5). Uncertainties arise in the mixed-pixel case in spatially heterogeneous mountain regions, i.e. if spectral signatures of various land cover types are combined within a single pixel. Methodologies have been developed to account for the mixed signal (Rosenthal and Dozier, 1996) and applied to medium resolution satellite data to obtain information on a certain land cover parameter at sub-pixel scale (e.g. Foppa et al., 2004, for snow cover).

In addition to the spectral resolution, the spatial resolution is a critical factor governing the usefulness of a sensor for the monitoring of a given land surface parameter in mountain regions. While sensors at high spatial resolution are commonly used for studies of small-scale geographic features in substantial detail, coarse spatial resolution sensors are employed to observe relatively large geographic areas (Weiss and Walsh, 2009). As previously addressed in Section 1.2.3, the decision on which sensor to use for a certain application, however, often comes along with a trade-off between the

spatial resolution of the sensor and the temporal resolution of the sensor system, as high spatial resolution sensors are generally characterized by low ground track repeat cycles and vice versa. The AVHRR and MODIS sensors both belong to the category of medium spatial resolution sensors and are characterized by high temporal resolution. This limits their use for observations of small geographic features, but increases their chance to observe a geographic location under cloud free conditions and to capture rapidly changing or transient land surface phenomena. A more detailed description of the characteristics of the AVHRR and the MODIS is included in Sections 2.3 and 2.4, respectively.

Despite the basic principles of remote sensing being the same in mountain regions and in other environments, the impact of complex topography on the quality of AVHRR and MODIS data (and remote sensing data in general) may require additional attention during data processing and interpretation. A short overview of possible impacts of complex topography follows in Section 2.2 as well as in Chapter 3.

2.2   Challenges due to complex topography

Impacts of complex topography on satellite data may be divided into direct and indirect effects. Direct effects include geometric distortions due to elevated topography (Voigt, 2000; Running et al., 1994) and radiometric distortions resulting from aspect-dependent illumination and reflectance conditions (Weiss and Walsh, 2009). Geometric distortions are present in satellite imagery as a consequence of the intertwined effects of surface elevation and observation geometry. They are characterized by the displacement of observed, elevated, targets in the direction of the sensor's scan line. In order to ensure that identical geographic locations are compared at a certain image coordinate in a time series of satellite images, this terrain displacement should be corrected for through the process of orthorectification using a DEM. This is of particular importance with regard to mountain regions often featuring high levels of spatial heterogeneity with rapidly changing land cover types on short horizontal distances. Chapter 3 describes the problem of terrain-induced geometric distortions in AVHRR imagery in more detail and discusses the orthorectification and its impact on climate data records based on AVHRR NDVI data.

Radiometric distortions result from the surface angular anisotropy described by the bidirectional reflectance distribution function (BRDF) of the Earth's surface (Li et al., 1996). While they are also observed over flat terrain, the situation is complicated in mountain areas because complex topography modifies the relative Sun-target-sensor geometry (Holben and Justice, 1980). This basically means that observation geometry

(i.e. zenith and azimuth angles of the Sun and the observing sensor) and terrain slope affect the radiance measured for a particular ground cover (Burgess et al., 1995). Other radiometric topographic effects result from the rugged relief surrounding the area covered by a pixel, which alters the amount of diffuse radiation, creates self- and cast-shadows by blocking the direct solar beam, and produces reflection from the neighboring area (Richter, 1998). Methodologies were developed to consider anisotropy effects, taking into account surface slope (Cihlar et al., 2004) and also the influence of terrain shadowing effects (Sirguey et al., 2009). Illumination effects are, however, also reduced by constraining the observation geometry (Luo et al., 2008) or by calculating spectral indices such as the NDVI from single channel data (Lee and Kaufman, 1986).

On the other hand, mountain regions are often characterized by persistent cloud cover due to orographically induced convection (Kästner and Kriebel, 2001), which may be regarded as an indirect effect of complex topography on the quality of satellite imagery. In order to obtain information on the cloud contamination of a pixel, cloud identification schemes are applied to satellite imagery. These are, depending on the spectral resolution of the sensor and the auxiliary data used, characterized by a varying degree of complexity (described in more detail in Sections 2.3 and 2.4). Even though observations affected by cloud cover are ideally recognized by cloud identification schemes and, therefore, excluded from analyses, supplemental post-processing may be required to correct time series of land surface parameters such as the NDVI for the the influence of persistent cloud cover (cf. Chapter 4).

Another factor indirectly affecting the quality of satellite-derived land surface param- eters in mountain regions is the lack of in situ data for ground validation (Weiss and Walsh, 2009). In complex and remote mountain areas ground data are often limited in number and concentrated along local traffic axis. For this reason, in situ measurements typically do not provide any information on more remote and inaccessible areas of in- terest, also because of the difficulty to extrapolate measured parameters in spatially heterogeneous mountain areas as discussed above. In this respect, validation studies in complex terrain using ground stations widely dispersed over a region of interest can provide important information about the quality of satellite-derived land surface parameters in mountain environments (cf. Chapter 4).

Given above considerations, the following sections describe the AVHRR and MODIS sensor systems as well as the datasets used in this thesis. In addition, an overview of the most important pre-processing steps is given: calibration, geocoding, and cloud/scene identification. Information is provided in particular detail for the AVHRR sensor due to its importance for the RSGB and the in-house processing chain.

2.3 The AVHRR

The following sections give an overview of the AVHRR sensor system, data archives, and pre-processing employed in the thesis. More detailed information is presented in Chapters 3 and 4. General information on the AVHRR sensor system and specific applications is provided in Cracknell (1997), Kidwell (1998), Goodrum et al. (2000), and Robel (2009).

2.3.1 Sensor system

The AVHRR sensor is carried onboard the NOAA POES and the EUMETSAT METOP-A platforms. The latest NOAA satellite, NOAA-19, is the last satellite of the NOAA series. Nevertheless, continuity until 2020 should be provided by the METOP series, which is planned to include two more satellites, METOP-B (scheduled launch: April 2011) and METOP-C (October 2015).

These satellites orbit at approximately 833 km above the Earth's surface with an inclination angle against the equator of 98.9°. Satellites need 102 minutes for one orbit resulting in approximately 14.2 orbits per day. At this altitude the maximum scan angle of $\pm55°$ results in a wide-swath of >2600 km for each satellite pass, which results in daily global coverage. The afternoon satellites are launched in an ascending (northbound) orbit, with an Equator crossing time (EXT) of ≈1500 (TIROS-N), ≈1430 (NOAA-7, -9), ≈1330 (NOAA-11, -14, -18), or ≈1400 (NOAA-16, -19; Ignatov et al., 2004). These orbits descend back from north to south on the dark side of the Earth at ≈0300, 0230, 0130, or 0200, respectively. The morning satellites descend from north to south at ≈0730, and ascend from south to north in the local evening, at ≈1930. NOAA-17 and METOP-A are mid-morning satellites, with descending (southbound) node passing at ≈1000, and ascending (northbound) node occurring at ≈2200. Even though the NOAA satellites were designed to be Sun-synchronous, their orbits evolve in time. Orbital drift causes a platform to systematically progress through different phases of the solar illumination and diurnal cycle of the underlying surface and atmosphere, which should be taken into account when analyzing long-term meteorological and climatological products (Gutman, 1999).

The AVHRR instrument has an instantaneous field-of-view (IFOV) of 1.41 milliradians providing a nominal spatial resolution of 1.1 km at the sub-satellite point, however, spatial resolution decreases significantly with increasing satellite view angle down to 2.4 km×6.5 km at the maximum off-nadir position. The radiometric resolution of the AVHRR is 10 bit, which results in 1024 levels of discrimination in measured response. Regarding the spectral resolution, the first version of the AVHRR (AVHRR/1) with four

Table 2.1: *Spectral characteristics of the different AVHRR sensors onboard various platforms. All values are approximations and might vary from satellite to satellite (Goodrum et al., 2000).*

Channel	TIROS-N, NOAA-6, -8, -10 AVHRR/1 [μm]	NOAA-7, -9, -11, -12, -14 AVHRR/2 [μm]	NOAA-15, -16, -17, -18, -19, Metop-A AVHRR/3 [μm]
1	0.58-0.68	0.58-0.68	0.58-0.68
2	0.73-1.10	0.73-1.10	0.73-1.0
3A	-	-	1.59-1.63
3B	3.55-3.93	3.55-3.93	3.55-3.93
4	10.50-11.50	10.30-11.30	10.30-11.30
5	Ch4 repeated	11.50-12.50	11.50-12.50

spectral bands was launched in October 1978 on board of TIROS-N satellite. It was subsequently improved to a 5-band instrument (AVHRR/2), that was initially carried on NOAA-7 (launched June 1981) and further through NOAA-14. NOAA-15 to -19 and METOP-A carry an enhanced version of the AVHRR (AVHRR/3) with 6 channels. On all three AVHRR sensors, channel 1 (2) is sensitive to reflected solar radiation in the red (near infrared) portion of the electromagnetic spectrum. The bandpass of the near-infrared channel 2 was narrowed on AVHRR/3 to reduce the impact of water vapor absorption and to enhance its sensitivity to vegetation reflectance. Channel 3 of AVHRR/1 and AVHRR/2 is centered at 3.7 μm and is sensitive to both reflected solar and emitted terrestrial radiation. Modifications were again made to AVHRR/3, where channel 3 can be switched between 1.6 μm (channel 3A) and 3.7 μm (channel 3B), depending on the application. However, due to strategic decisions, channel 3A/3B alteration is only enabled for AVHRR/3 onboard NOAA-17 and METOP-A. The thermal channels 4 and 5 are designed to measure emitted terrestrial radiation. The spectral characteristics of the AVHRR sensors carried on various platforms are summarized in Table 2.1. The generation and analysis of long-term AVHRR-based climate data records from different missions may require a correction for differences in the spectral response function between various AVHRR sensors (Trishchenko et al., 2002b; Trishchenko, 2009; Swinnen and Veroustraete, 2008, see also Chapter 3).

2.3.2   Data pre-processing

AVHRR channels 1, 2, and where available 3A are commonly calibrated to top of atmosphere (TOA) reflectances, the thermal channels 3B, 4 and 5 to TOA brightness temperatures. The task of accurately calibrating the AVHRR optical channels is, however, not straightforward due to the lack of an onboard calibration device for these channels. Pre-launch calibration coefficients have shown to be inaccurate after launch and AVHRR optical channels to degrade with time (Rao et al., 1996). As a consequence, several time dependent post-launch calibration methods based on the observation of radiometrically stable targets such as desert sites, bright clouds, and snow- and ice-covered polar regions with known reflectance have been proposed (Rao et al., 1996; Rao and Chen, 1996; Heidinger et al., 2003; Vermote, 1995; Vermote and Saleous, 2006; Loeb, 1997). However, provided calibration coefficients can vary significantly depending on the method, which inevitably results in discrepancies between datasets calibrated using different calibration coefficients (Swinnen and Veroustraete, 2008). Efforts are currently ongoing, aiming at providing a consistent set of calibration coefficients for the entire period of AVHRR coverage (personal communication A. Trishchenko, 2008). Calibration of the thermal channels is somewhat easier due to the onboard calibration device. Nevertheless, additional refinement is needed to correct for detector nonlinearities, noise, and solar blackbody contamination (Goodrum et al., 2000; Walton et al., 1998; Trishchenko, 2002; Trishchenko et al., 2002a). Accurate calibration is of particular interest with regard to the generation of long-term time series of AVHRR data for the use in climate studies; insufficient calibration may lead to artificial trends in AVHRR-based climatological time series (Gutman, 1999).

Regarding georeferencing three major steps should be applied in order to meet high geolocation accuracy: orbit modelling, refinement using Ground Control Points (GCPs), and orthorectification (Khlopenkov et al., 2009). Using orbit models to predict the satellites position, geolocation accuracies of 1–4 km can be achieved (Rosborough et al., 1994). Errors are observed due to inaccuracies in the orbital parameters, satellite clock errors, and deviations of the satellite attitude angles (roll, pitch, and yaw) from the nominal position. In order to improve geolocation accuracy, refinement based on a set of GCPs is necessary (Moreno and Melia, 1993). Distinct features such as continental coasts or shorelines of inland lakes are usually selected as GCPs. Geographic coordinates of the entire image are then adjusted using a polynomial transformation, which minimizes the error of the image chips in the scene to be rectified relative to the reference image. Finally, orthorectification as addressed above and in detail in Chapter 3 should be an integral step of georeferencing to account for the influence

of surface elevation. More information on the achievement of precise geolocation in both datasets used in this thesis is provided below.

Cloud identification as addressed above is of critical importance for land surface applications as it provides information on the contamination of pixels by clouds or cloud shadows. Several different cloud identification schemes of varying complexity have been presented for AVHRR during the past decades (e.g. Saunders and Kriebel, 1988; Baum and Trepte, 1999; Dybbroe et al., 2005a,b; Heidinger, 2007; Key, 2002; Khlopenkov and Trishchenko, 2007). For the discrimination of clouds, the basic principle is that they are brighter than most surfaces in the solar reflective bands (cf. Figure 2.1), but colder in the thermal bands. Difficulties arise over very bright surfaces such as snow and arid areas as shown in Figure 2.1 (b, f), or also for low stratiform clouds in mountain valley inversions, if cloud temperature does not significantly differ from the one of the (snow covered) Earth's surface. In this context, some cloud identification schemes also include information on the presence of snow in the area covered by a pixel (Baum and Trepte, 1999; Khlopenkov and Trishchenko, 2007). In support of the spectral tests, temporal texture test including multiple scenes may be applied to make use of temporal reflectance variations for cloud identification at a certain image coordinate (Key, 2002). A number of cloud identification schemes was developed to also use auxiliary data e.g. on the current state of the atmosphere (Dybbroe et al., 2005a,b) or on land surface temperature to help in cloud identification (Khlopenkov and Trishchenko, 2007). Furthermore, cloud shadows should properly be accounted for, since they are a substantial source of uncertainty in surface property retrievals (Latifovic et al., 2005). Cloud shadow detection algorithms for AVHRR include geometrical considerations by projecting the cloud shadow on the Earth's surface (Khlopenkov and Trishchenko, 2007) or also a combination of geometric and optical constraints in combination with statistical image analysis methods (Simpson and Stitt, 1998).

2.3.3 Data records

Three data types are available from the AVHRR sensor: global area coverage (GAC) and local area coverage (LAC) data, both stored onboard the satellite and transmitted to a specific ground receiving station at the time of overpass, and the direct read-out high-resolution picture transmission (HRPT) format (Cracknell, 1997). While both LAC and HRPT data provide imagery at the full spatial resolution of AVHRR (1.1 km), this is not the case for the GAC format. GAC data are characterized by a reduced spatial resolution, which is achieved through a spatial sampling scheme onboard the satellite in realtime (see Section 3.1.1 for a detailed description of the sampling scheme). Spatial sampling results in a significant reduction of the data volume, which allows much

larger geographic areas to be recorded onboard the satellite before data transmission to a receiving station. As a consequence, GAC AVHRR data are globally available for the entire operational period of AVHRR and have repeatedly served as a basis for the generation of unique global long-term climate data records (Gutman et al., 1995; James and Kalluri, 1994; Tucker et al., 2005; Romanov et al., 2000).

As such, GAC-based datasets have previously been used to study land surface parameters in mountain regions, for example, vegetation photosynthetic activity based on NDVI time series in the European Alps (Stöckli and Vidale, 2004) or Alaska (Jia et al., 2003). Nevertheless, there is a strong need to process AVHRR data at the full spatial resolution of 1 km (CEOS, 2006), since the use of spatially degraded GAC data in heterogeneous mountain areas may lead to important biases in satellite data records (cf. Chapter 3). However, full spatial resolution AVHRR data archives that cover the entire operational period of AVHRR (or major parts of it) are limited in number: based on a comprehensive AVHRR archive hosted at the Canada Centre for Remote Sensing (CCRS), Ottawa, Canada, a long-term dataset (1981 to 2004) at 1 km spatial resolution covering entire Canada was made available for the use in climate studies (Latifovic et al., 2005). Another 1-km dataset was compiled for Southern Africa between 1985 and 1998 to extend a SPOT VEGETATION derived NDVI dataset back in time (Swinnen and Veroustraete, 2008). In Europe, full-resolution AVHRR data for the use in long-term studies of land surface parameters are available from the Mediterranean Extended Daily One Kilometer AVHRR Data Set (MEDOKADS) (Koslowsky, 2003) as well as at the German Aerospace Centre (DLR; Dech et al., 1998). Another comprehensive archive for the period from 1984 to present covering the European Alps is hosted at the Remote Sensing Research Group (RSGB), University of Bern, Switzerland (Hüsler et al., 2009). Two of these comprehensive full resolution AVHRR datasets served as a basis for this thesis (described in more detail below): the dataset hosted at the CCRS is employed in Chapter 3, and the dataset hosted at the RSGB, which is used in Chapter 4.

The CCRS AVHRR dataset

Information on the archive and processing steps provided here follows detailed descriptions in Latifovic et al. (2005), Khlopenkov and Trishchenko (2007), Khlopenkov and Trishchenko (2008), and Khlopenkov et al. (2009). The CCRS archive encompasses all AVHRR data ever collected for the area of Canada by several receiving stations within Canada and also by NOAA. Data is available at 1 km spatial resolution in Lambert Conformal Conic (LCC) map projection for an area of the size 5700 km×4800 km centered over Canada. It thereby covers the entire area of Canada including Green-

land, parts of Alaska and the northern part of the conterminous United States (Figure 2.2, top).

Calibration of the optical channels from current missions is performed according to the NOAA recommendations using the monthly updated calibration coefficients. For historical data, the calibration is based on the time-dependent piecewise linear calibration method developed at the CCRS (Cihlar and Teillet, 1995). Calibration of the thermal channels follows Trishchenko (2002), Trishchenko et al. (2002a), and Trishchenko (2006).

With regard to the geolocation accuracy requirements for systematic satellite observations defined by GCOS (GCOS, 2006), a novel and highly efficient georeferencing algorithm was recently developed at the CCRS: the Canadian AVHRR Processing System (CAPS; Khlopenkov et al., 2009). Georeferencing in CAPS includes a number of novel features in support of the three major georeferencing steps as described in Section 2.3.2: (1) image sharpening using the Laplace operator prior to correlation analysis, (2) georeferencing relative to monthly clear-sky composites at 250 m spatial resolution from the MODIS sensor to take advantage of the high accuracy of MODIS image geolocation, (3) orthorectification based on a 250 m spatial resolution DEM in swath projection, (4) an image matching technique in native swath projection based on an automatically generated GCP library including the determination of the satellite state vector and sensor attitude angles to achieve the best fits, and (5) remapping of the imagery from swath to LCC projection using a gradient search method (Khlopenkov and Trishchenko, 2008). The combination of these steps results in a geolocation accuracy of better than 1/3 of the sensor's field of view (FOV) and, hence, provides output in accordance with the requirements of GCOS and the Committee on Earth Observing Satellites (CEOS, 2006). A thorough analysis of CAPS geolocation accuracy over mountain regions will be the subject of Chapter 3.

Scene identification is done based on the Separation of Pixels Using Aggregated Rating over Canada (SPARC) algorithm (Khlopenkov and Trishchenko, 2007). The SPARC algorithm calculates a series of ratings for each pixel based on several spectral tests. Furthermore, surface skin temperatures from the North American Regional Reanalysis (NARR) dataset, which is available at 32 km×32 km spatial resolution, is used as additional input. By combining all the tests, one single rating is calculated, providing a measure of the cloud contamination probability for a pixel. In addition, SPARC provides information on the status of a pixel (cloud shadow, snow/ice, land/water).
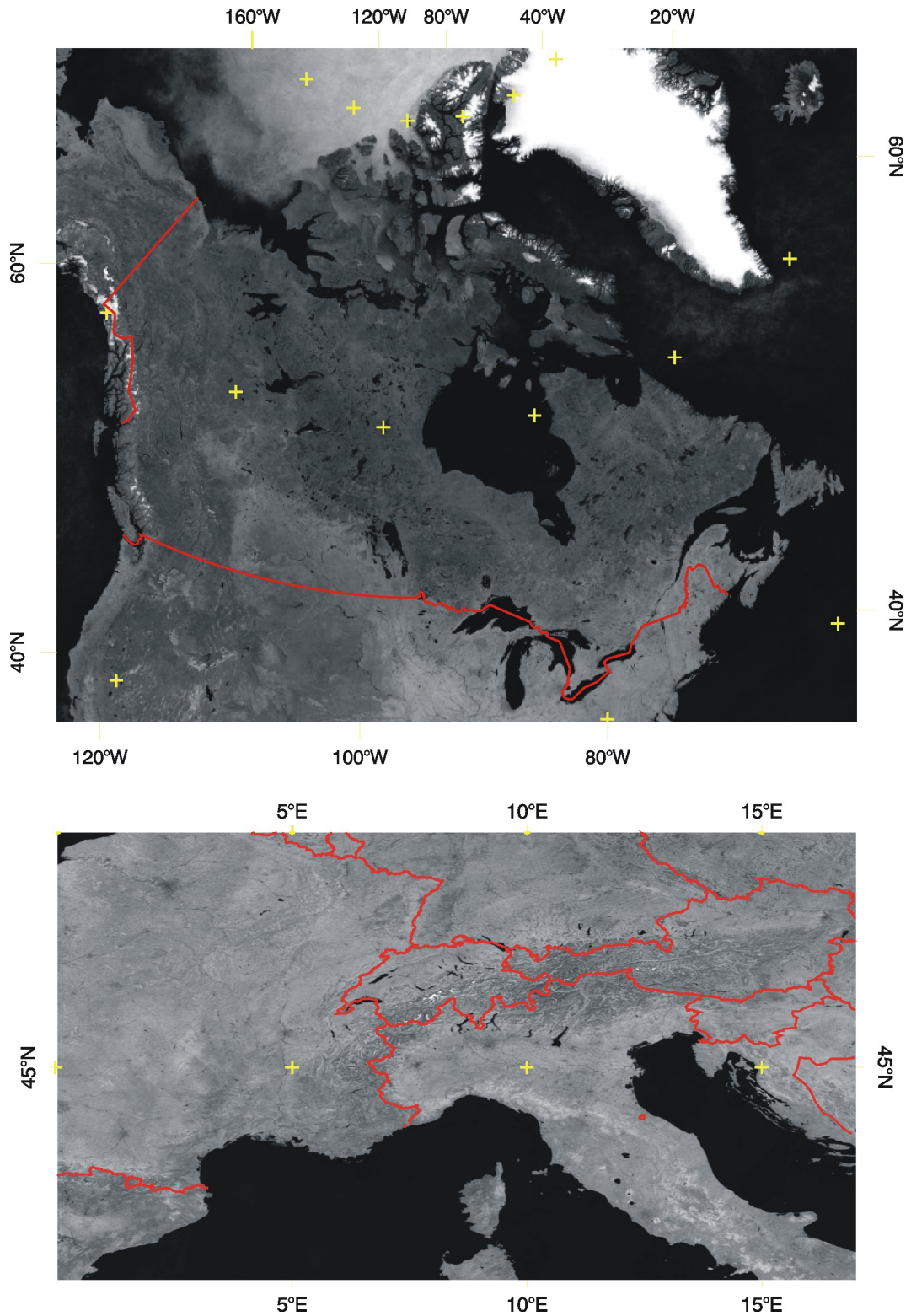
Figure 2.2: *Geographic extent of the CCRS dataset (top) in Lambert Conformal Conic (LCC) projection and the RSGB dataset (bottom) in Equirectangular projection. Political boundaries are delineated in red. The CCRS image corresponds to the CAPS reference image for the month of August based on MODIS band 2 (provided by K. Khlopenkov); the RSGB image corresponds to a MODIS band 2 clear-sky composite for the month of July in 2004 to 2007 (provided by F. Hüsler).*

The RSGB AVHRR dataset

A detailed overview of the RSGB AVHRR dataset and processing is provided in Hüsler et al. (2009). The majority of the archived data were recorded by the receiving facility at the University of Bern, Switzerland (46.93°N, 7.41°E). Contributions from the Comprehensive Large Array data Stewardship System (CLASS) archive, the Freie Universität (FU) Berlin, Germany, and the German Aerospace Centre (DLR) helped to extend the archive back to 1984. At the present moment, there are 25 years of AVHRR data available at the full spatial resolution of 1 km, even though only morning overpasses are archived for the period from 1984 and 1989. Due to the geographic location of Bern, the European Alps have traditionally been in the research focus of the RSGB. As a consequence, data processing is generally constrained to the area between 40.5°N and 50.0°N, and between 0.0°E and 17.0°E (Figure 2.2, bottom) and creates output in Equirectangular projection at 0.01°×0.01° resolution. It is, however, planned to extend processing to the area from 25°N to 75°N and from 15°W to 50°E in the near future to provide a full spatial resolution AVHRR dataset for entire Europe and parts of Northern Africa and Western Asia.

Optical channels from current missions for realtime applications are calibrated according to the NOAA recommendations using the monthly updated calibration coefficients. For the reprocessing of the entire archive, calibration is carried out based on PATMOS-X calibration coefficients that were obtained from A. Heidinger[1] through personal communication (March, 2009). The thermal emissive channels of the AVHRR/3 instrument are calibrated according to the KLM Users Guide (Goodrum et al., 2000). For AVHRR/2, the method suggested by Kidwell (1998) was modified such that the non-linear response of the channels 3B, 4 and 5 is corrected according to Walton et al. (1998).

The automated image navigation scheme implemented at the RSGB follows the three-step procedure as described in Section 2.3.2. In addition, a land feature based correction of image navigation parameters is included to account for errors introduced by non-zero satellite attitude angles (Crawford, 2005). Chip matching is is based on a predefined GCP library, which may be complemented by randomly defined GCPs if the number of GCPs accepted from the library does not exceed a predefined threshold (50 GCPs). Orthorectification is carried out with a DEM at 1 km spatial resolution. Geolocation accuracy to be expected for the RSGB processing chain is ≈0.5 pixel, which has enabled the investigations of small scale features within the European Alps (e.g. surface water temperature of small alpine lakes; Oesch et al., 2005); however,

---

[1]currently at NOAA National Environmental Satellite, Data, and Information Service (NESDIS), Center for Satellite Applications and Research (STAR) as a physical scientist.

additional refinement with regard to the GCOS geolocation accuracy requirements is necessary in the near future.

Cloud masking is provided by the Cloud and Surface Parameter Retrieval (CASPR) algorithm (Key, 2002). The algorithm quality has been proved by Di Vittorio and Emery (2002) and was additionally validated using the cloud detection scheme of the Satellite Application Facility to support Nowcasting and very Short-Range Forecasting/Polar Platform System (SAFNWC/PPS) for the area of central Europe (Wildeisen, 2008). The CASPR output is a binary cloud/clear mask. In addition, the cloud/scene identification scheme implemented at the RSGB includes cloud shadow detection according to Simpson and Stitt (1998).

2.4   The MODIS

The following sections give an overview of the MODIS sensor system, data archives, and pre-processing employed in the thesis. General information on the MODIS and its application for land surface remote sensing is available in Salomonson et al. (1989), Running et al. (1994), Barnes et al. (1998), and Justice et al. (1998).

2.4.1   Sensor system

The MODIS sensor combines characteristics of the AVHRR and the Landsat TM and was designed to improve and complement monitoring of land, ocean, and atmosphere by these previous missions. The sensor is carried onboard the Earth Observing System (EOS) morning (AM1, or TERRA) and afternoon satellites (PM1, or AQUA). Satellites need 102 minutes for one orbit, which results in approximately 14.2 orbits per day. The satellites orbit at $\approx$705 km above the Earth's surface with a Sun-synchronous 98° inclination, where the maximum scan angle of $\pm$55° results in a swath width of 2330 km. This enables the sensor to observe nearly the entire Earth every two days. The morning satellite (TERRA) crosses the Equator descending at 1030, when cloud cover typically is at its daily minimum. The afternoon satellite (AQUA) crosses the Equator in ascending mode at 1330, which in combination with TERRA enables the observation of the diurnal cycle of various components of the Earth's system.

The MODIS provides higher radiometric sensitivity compared to AVHRR. In each of the 36 spectral bands, the 12-bit resolution results in 4096 levels of discrimination in measured response. The bands are sensitive to different portions of the electromagnetic spectrum between 0.46 μm and 14.39 μm at spatial resolutions of 250 m, 500 m, and 1 km, depending on the spectral band. Table 2.2 lists the spectral characteristics

Table 2.2: *Spectral characteristics of the MODIS sensor in the seven land bands (B1 to B7) and the associated spatial resolution (Barnes et al., 1998).*

Band	Bandwidth [μm]	Spatial resolution [m]
B1	0.62 - 0.67	250
B2	0.84 - 0.88	250
B3	0.46 - 0.48	500
B4	0.55 - 0.57	500
B5	1.23 - 1.25	500
B6	1.63 - 1.65	500
B7	2.11 - 2.16	500

of the MODIS bands in the focus of this thesis, bands B1 to B7, which all measure reflected solar radiation and were designed to observe land cover features plus cloud and aerosol properties. A specification of all 36 spectral bands can be found in Barnes et al. (1998).

2.4.2   Data pre-processing

In order to avoid problems with the calibration of the reflective solar bands as described above for AVHRR, MODIS design includes a set of sophisticated onboard calibration modules for the calibration of both the reflective solar as well as thermal emissive bands. The reflective solar bands are calibrated on orbit by a solar diffuser (SD) and a solar diffuser stability monitor (SDSM) system, the thermal emissive bands with wavelengths above 3.7 μm are calibrated by an on-board blackbody. In addition, MODIS views the Moon a few times per year. Given that the brightness of the Moon illuminated by the Sun does not change in time, the Moon provides a valuable radiance source for vicarious calibration similar to the stable targets as described for AVHRR. The output delivered by the MODIS level 1B algorithm includes geolocated at-aperture radiances in all 36 spectral bands. Details on the calibration algorithms and on-orbit performance of MODIS reflective solar and thermal emissive bands is provided in Xiong et al. (2003b,a, 2005).

Earth location data is available at sub-pixel accuracy ($\approx$50 m). This extraordinary geolocation accuracy is achieved due to several reasons (Wolfe et al., 2002, 1995): First, the spacecrafts carrying MODIS are very stable and provide highly precise external orientation knowledge. Second, the MODIS instrument was designed to give precise interior orientation knowledge. Third, an accurate global DEM (Logan, 1999) is used to model

and remove relief-induced distortions as discussed above. Fourth, a global set of GCPs based on Landsat imagery served to determine biases in the sensor orientation, which were finally used to improve geolocation processing.

The standard MODIS cloud identification scheme uses 19 out of 36 available spectral bands to obtain information about the cloud contamination of a scene observed by the sensor (Ackerman et al., 2006, 1998). In addition, the algorithm relies on auxiliary information such as the daily snow and ice maps made available by the National Snow and Ice Data Centre (NSIDC) and NOAA, global ecosystem maps at 1 km resolution, elevation above sea level, land/water mask, and observation geometry. The output of the MODIS cloud detection algorithm is a 46-bit mask containing information on the level of confidence with regard to a pixel assumed to be clear, as well as information on the presence of cloud shadows for clear-sky pixels.

2.4.3   Data records

The geolocated and radiometrically calibrated output of the MODIS Level 1B algorithm serves as a basis for the generation of a large number of scientific datasets for atmospheric, oceanic, and land applications at a wide range of spatial (250 m, 500 m, 1 km, and coarser resolution) and temporal resolutions (daily, 8-day, 16-day, and monthly). An overview of the products made available by the MODIS science teams together with detailed descriptions is provided at http://modis.gsfc.nasa.gov/. Land surface products include, inter alia, snow cover, land cover dynamics, vegetation indices such as the NDVI, or surface reflectance, which is utilized in Chapter 4. MODIS standard products are distributed in sinusoidal (SIN), integerized SIN, or a lat/long grid (for coarse resolution products). These projections were chosen because they are designed for global coverage, although they reveal substantial distortions near polar regions (Khlopenkov and Trishchenko, 2008).

The GCOS has recommended a spatial resolution of 250 m for many Essential Climate Variables (ECVs) intended for terrestrial applications, such as snow cover, leaf area index (LAI), or albedo (GCOS, 2006, Appendix 2). However, only MODIS bands B1 and B2 meet these requirements, even though it would be very beneficial for many land surface applications to have all seven land bands available at this spatial resolution. Hence, to enable studies of long-term variations of various land surface parameters at 250 m spatial resolution consistent with the GCOS requirements for ECVs, a novel MODIS dataset was recently developed at the CCRS. This dataset, which is employed in Chapters 3 and 5, will be introduced in the following section.

The CCRS MODIS dataset

The generation of the CCRS MODIS dataset at 250 m spatial resolution in all seven land bands includes three major steps (the description of the methodology closely follows Luo et al., 2008; Trishchenko et al., 2009; Khlopenkov and Trishchenko, 2008):

1. downscaling of the 500 m spatial resolution bands (B3 to B7) to 250 m for consistency with bands B1 and B2 (Trishchenko et al., 2006)

2. reprojection of the downscaled imagery from swath to LCC projection (Khlopenkov and Trishchenko, 2008), and

3. clear-sky compositing at 250 m spatial resolution (Luo et al., 2008).

In step 1, reflectances in bands B3 to B7 at 250 m resolution are calculated based on the reflectances in bands B1 and B2. The underlying principle is, that bands B1 and B2 contain substantial information on the general shape of the pixel spectrum to be expected for a certain land cover type. As a consequence, bands B3 to B7 can each be correlated to B1, B2, and the NDVI (obtained by combining B1 and B2), assuming a small number of basic scene types. The scene types, vegetation, desert/barren land, snow, water, and cloud, are classified according to their spectral features in bands B1, B2, and B6. First, an adaptive regression model based on 500 m data in all seven bands is built to estimate the regression parameters for a respective scene type. This model is built for each 5-min granule separately, and within a granule for blocks of 541×812 pixels to reduce the impact of latitudinal variation of surface properties and observation geometry effects. The model is then applied to B1 and B2 at 250 m resolution to estimate B3 to B7. Resulting 250 m images are subsequently normalized to the original 500 m imagery to preserve radiometric properties of the original data.

In step 2, images are reprojected from swath to a standard geographic projection. Due to the distortions introduced by the standard projection used for MODIS products, swath data are reprojected to Lambert Azimuthal Equal Area (LAEA) projection (alternatively to LCC projection, depending on the application) to better preserve image information content (see Luo et al., 2008 for the projection parameters). Reprojection is performed based on a gradient search method, which was shown to preserve the absolute geolocation accuracy of MODIS pixels determined by the MODIS geolocation team (Khlopenkov and Trishchenko, 2008; Wolfe et al., 2002).

Finally, clear-sky compositing is done in step 3 based on bands B1, B2, B3, and B6. This is a two-step procedure: First, scene identification is performed at 250 m spatial resolution by combining geometrical and spectral approaches. The product is a mask

delineating cloud cover, cloud shadows, and areas observed under clear-sky conditions. Together with a set of decision rules (described in detail in Luo et al., 2008), this mask is subsequently used as a basis for clear-sky compositing. In addition, to reduce the impact of BRDF effects on the composites, two composites are generated for each composite interval: one for the forward and one for the backward scattering hemisphere. This was shown to significantly enhance the quality of the clear-sky composites.

References

Ackerman, S. A., K. I. Strabala, P. Menzel, R. Frey, C. Moeller, L. Gumley, B. Baum, S. Wetzel Seemann, and Z. Hong (2006). Discriminating clear sky from clouds with MODIS, Algorithm theoretical basis document (MOD35). Available online at: http://modis.gsfc.nasa.gov/.

Ackerman, S. A., K. I. Strabala, W. P. Menzel, R. A. Frey, C. C. Moeller, and L. E. Gumley (1998). Discriminating clear sky from clouds with MODIS. *Journal of Geophysical Research* **103**, –.

Barnes, W. L., T. S. Pagano, and V. V. Salomonson (1998). Prelaunch characteristics of the Moderate Resolution Imaging Spectroradiometer (MODIS) on EOS-AM1. *IEEE Transactions on Geoscience and Remote Sensing* **36**, 1088–1100.

Baum, B. and Q. Trepte (1999). A grouped Threshold Approach for Scene Identification in AVHRR Imagery. *Journal of Atmospheric and Oceanic Technology* **16**, 793–800.

Burgess, D., J.-P. A. Muller, and P. Lewis (1995). Topographic Effects in AVHRR NDVI Data. *Remote Sensing of Environment* **54**, 223–232.

CEOS (2006). Satellite observation of the climate system: The Committee on Earth Observation Satellites (CEOS) response to the implementation plan for the Global Observing System for Climate in support of the UNFCCC. Available online at: http://www.ceos.org/images/PDFs/CEOSResponse_1010A.pdf.

Cihlar, J., R. Latifovic, J. Chena, A. Trishchenko, Y. Duc, G. Fedosejev, and B. Guindona (2004). Systematic corrections of AVHRR image composites for temporal studies. *Remote Sensing of Environment* **89** (2), 217–233.

Cihlar, J. and P. M. Teillet (1995). Forward piecewise linear calibration model for quasi-real time processing of AVHRR data. *Canadian Journal of Remote Sensing* **21**, 20–27.

Cracknell, A. (1997). *The Advanced Very High Resolution Radiometer*. London: Taylor & Francis Ltd.

Crawford, P. (2005). Software Manual Landmark Navigation Correction. Crawford Space Communications Ltd.

Dech, S. W., P. Tungalagsaikhan, C. Preusser, and R. E. Meisner (1998). Operational value-adding to AVHRR data over Europe: methods, results, and prospects. *Aerospace Science and Technology* **2** (5), 335–346.

Di Vittorio, A. V. and W. J. Emery (2002). An automated, dynamic threshold cloud-masking algorithm for daytime AVHRR images over land. *IEEE Transactions on Geoscience and Remote Sensing* **40** (8), 1682–1694.

Dozier, J. and T. H. Painter (2004). Multispectral and hyperspectral remote sensing of alpine snow properties. *Annual Review of Earth and Planetary Science* **32** (1), 465–494.

Dybbroe, A., K. G. Karlsson, and A. Thoss (2005a). NWCSAF AVHRR Cloud Detection and Analysis Using Dynamic Thresholds and Radiative Transfer Modeling. Part I: Algorithm Describtion. *Journal Of Applied Meteorology* **44**, 39–54.

Dybbroe, A., K. G. Karlsson, and A. Thoss (2005b). NWCSAF AVHRR Cloud Detection and Analysis Using Dynamic Thresholds and Radiative Transfer Modeling. Part II: Tuning and Validation. *Journal Of Applied Meteorology* **44**, 55–71.

Foppa, N., S. Wunderle, A. Hauser, D. Oesch, and F. Kuchen (2004). Operational sub-pixel snow mapping over the Alps with NOAA-AVHRR data. *Annals of Glaciology* **38**, 245–252.

GCOS (2006). Systematic Observation Requirements for Satellite-based Products for Climate: Supplemental details to the satellite-based component of the Implementation plan for the Global Observing System for Climate in support of the UNFCC. GCOS-107, WMO/TD-1338.

Gitelson, A. A. and M. N. Merzlyak (1996). Signature analysis of leaf reflectance spectra : Algorithm development for remote sensing of chlorophyll. *Journal of Plant Physiology* **148**, 494–500.

Goodrum, G., K. B. Kidwell, and W. Winston (2000). NOAA KLM user's guide. Technical report, National Environmental Satellite, Data, and Information Services (NESDIS).

Gutman, G., D. Tarpley, A. Ignatov, and S. Olson (1995). The enhanced NOAA Global Land datasets from the Advanced Very High Resolution Radiometer. *Bulletin of the American Meteorological Society* **76**, 1141–1156.

Gutman, G. G. (1999). On the use of long-term global data of land reflectances and vegetation indices derived from the advanced very high resolution radiometer. *Journal of Geophysical Research* **104**, 6241–6256.

Heidinger, A. K. (2007). Clouds from AVHRR Extended (CLAVR-X) research at CIMSS. Available at http://cimss.ssec.wisc.edu/clavr/index.html.

Heidinger, A. K., J. T. Sullivan, and C. R. N. Rao (2003). Calibration of visible and near-infrared channels of the NOAA-12 AVHRR using time series of observations over deserts. *International Journal of Remote Sensing* **24** (18), 3635–3649.

Holben, B. N. and C. O. Justice (1980). The topographic effect on spectral response from nadir-pointing sensors. *Photogrammetric Engineering and Remote Sensing* **46**, 1191–1200.

Hüsler, F., F. Fontana, C. Neuhaus, M. Riffler, and S. Wunderle (2009). NOAA AVHRR archive and processing facility at the University of Bern: A comprehensive 1-km satellite data set for climate change studies in Europe. *submitted to International Journal of Remote Sensing*.

Ignatov, A., I. Laszlo, E. Harrod, K. Kidwell, and G. Goodrum (2004). Equator Crossing Times for NOAA, ERS and EOS Sun-Synchronous Satellites. *International Journal of Remote Sensing* **25** (23), 5255 – 5266.

James, M. and S. Kalluri (1994). The Pathfinder AVHRR land data set: An improved coarse resolution data set for terrestrial monitoring. *International Journal of Remote Sensing* **15**, 3347–3363.

Jia, G. J., H. E. Epstein, and D. A. Walker (2003). Greening of arctic Alaska, 1981–2001. *Geophys. Res. Lett.* **30**, –.

Justice, C. O., E. Vermote, J. R. G. Townshend, R. Defries, D. P. Roy, D. K. Hall, V. V. Salomonson, J. L. Privette, G. Riggs, A. Strahler, W. Lucht, R. B. Myneni, Y. Knyazikhin, S. W. Running, R. R. Nemani, Z. Wan, A. R. Huete, W. van Leeuwen, R. E. Wolfe, L. Giglio, J. Muller, P. Lewis, and M. J. Barnsley (1998). The Moderate Resolution Imaging Spectroradiometer (MODIS): Land Remote Sensing for Global Change Research. *IEEE Transactions on Geoscience and Remote Sensing* **36** (4), 1228–1249.

Kästner, M. and K. T. Kriebel (2001). Alpine cloud climatology using long-term NOAA-AVHRR satellite data. *Theoretical and Applied Climatology* **68** (3), 175–195.

Key, J. (2002). The Cloud and Surface Parameter Retrieval (CASPR) System for Polar AVHRR - User's Guide. Technical report, Cooperative Institute for Meteorolog-

ical Satellite Studies, University of Wisconsin, 1225 West Dayton St., Madison, WI 53562.

Khlopenkov, K. V. and A. P. Trishchenko (2007). SPARC: New cloud, snow, and cloud shadow detection scheme for historical 1-km AVHRR data over Canada. *Journal Of Atmospheric And Oceanic Technology* **24** (3), 322–343.

Khlopenkov, K. V. and A. P. Trishchenko (2008). Implementation and evaluation of concurrent gradient search method for reprojection of MODIS level 1B imagery. *IEEE Transaction on Geoscience and Remote Sensing* **46**, 2016–2027.

Khlopenkov, K. V., A. P. Trishchenko, and Y. Luo (2009). Image matching technique for sub-pixel georeferencing accuracy in Canadian AVHRR Processing System (CAPS). *submitted to IEEE Transaction on Geoscience and Remote Sensing*.

Kidwell, K. (1998). NOAA polar orbiter data user's guide (TIROS-N, NOAA-6, -7, -8, -9,-10, -11, -12, -13 and -14). Technical report, NOAA/National Environmental Satellite, Data, and Information Service (NESDIS).

Koslowsky, D. (2003). The MEDOKADS data set as a substantial part of a remote sensing data network for a Mediterranean research and application network. In H.-J. Bolle (ed.), *Mediterranean Climate*, pp. 165–177. Berlin: Springer Verlag.

Latifovic, R., A. Trishchenko, J. Chen, W. Park, K. Khlopenkov, R. Fernandes, D. Pouliot, C. Ungureanu, Y. Luo, S. Wang, A. Davidson, and J. Cihlar (2005). Generating Historical AVHRR 1 km Baseline Satellite Data Records Over Canada Suitab,e for Climate Change Studies. *Canadian Journal of Remote Sensing* **31** (5), 324–346.

Lee, T. Y. and Y. J. Kaufman (1986). Non-Lambertian effects on remote sensing of surface reflectance and vegetation index. *IEEE Transactions on Geoscience and Remote Sensing* **24**, 699–708.

Li, Z., J. Cihlar, X. Zheng, L. Moreau, and L. Hung (1996). The bidirectional effects of AVHRR measurements over boreal regions. *IEEE Transactions on Geoscience and Remote Sensing* **34**, 1308–1322.

Lillesand, T., R. Kiefer, and J. Chipman (2004). *Remote Sensing and Image Interpretation* (fifth Ed.). New York: John Wiley & Sons.

Loeb, N. G. (1997). In-flight calibration of NOAA AVHRR visible and near-IR bands over Greenland and Antarctica. *International Journal of Remote Sensing* **18** (3), 477–490.

Logan, T. L. (1999). EOS/AM-1 Digital Elevation Model (DEM) Data Sets: DEM and DEM Auxiliary Datasets in Support of the EOS/Terra Platform. JPL D-013508. Jet Propulsion Laboratory, California Institute of Technology.

Luo, Y., A. P. Trishchenko, and K. V. Khlopenkov (2008). Developing clear-sky, cloud and cloud shadow mask for producing clear-sky composites at 250-meter spatial resolution for the seven MODIS land bands over Canada and North America. *Remote Sensing of Environment* **112** (12), 4167–4185.

Moreno, J. F. and J. Melia (1993). A method for accurate geometric correction of NOAA AVHRR HRPT data. *IEEE Transactions on Geoscience and Remote Sensing* **31** (1), 204–226.

Oesch, D. C., J. M. Jaquet, A. Hauser, and S. Wunderle (2005). Lake surface water temperature retrieval using Advanced Very High Resolution Radiometer and Moderate Resolution Imaging Spectroradiometer data: Validation and feasibility study. *Journal of Geophysical Research* **110**, C12014.

Rao, C. R. N. and J. Chen (1996). Post-launch calibration of the visible and near-infrared channels of the Advanced Very High Resolution Radiometer on the NOAA-14 spacecraft. *International Journal of Remote Sensing* **17** (14), 2743–2747.

Rao, C. R. N., J. Chen, N. Zhang, J. T. Sullivan, C. C. Walton, and M. P. Weinreb (1996). Calibration of meteorological satellite sensors. *Advances in Space Research* **17** (1), 11–20.

Richter, R. (1998). Correction of satellite imagery over mountainous terrain. *Applied Optics* **37**, 4004–4015.

Robel, J. (2009). NOAA KLM user's guide with NOAA-N,-P supplement. Technical report, NOAA/National Environmental Satellite, Data, and Information Services (NESDIS).

Romanov, P., G. Gutman, and I. Csiszar (2000). Automated Monitoring of Snow Cover over North America with Multispectral Satellite Data. *Journal of Applied Meteorology* **39** (11), 1866–1880.

Rosborough, G. W., D. G. Baldwin, and W. J. Emery (1994). Precise AVHRR image navigation. *IEEE Transactions on Geoscience and Remote Sensing* **32** (3), 644–657.

Rosenthal, W. and J. Dozier (1996). Automated mapping of montane snow cover at subpixel resolution from the Landsat Thematic Mapper. *Water Resources Research* **32** (1), 115–130.

Running, S. W., C. O. Justice, V. Salomonson, D. Hall, J. Barker, Y. J. Kaufmann, A. Strahler, A. R. Huete, J.-P. Muller, V. Vanderbilt, Z. M. Wan, P. Teillet, and D. Carneggie (1994). Terrestrial remote sensing science and algorithms planned for EOS/MODIS. *International Journal of Remote Sensing* **15** (17), 3587–3620.

Salomonson, V., W. Barnes, P. Maymon, H. Montgomery, and H. Ostrow (1989). MODIS: Advanced facility instrument for studies of the Earth as a system. *IEEE Transactions on Geoscience and Remote Sensing* **27** (2), 145–153.

Salomonson, V. V. and I. Appel (2004). Estimating fractional snow cover from MODIS using the normalized difference snow index. *Remote Sensing of Environment* **89** (3), 351–360.

Saunders, R. W. and K. T. Kriebel (1988). An improved method for detecting clear sky and cloudy radiances from AVHRR data. *International Journal of Remote Sensing* **9** (1), 123–150.

Simpson, J. J. and J. R. Stitt (1998). A procedure for the detection and removal of cloud shadow from AVHRR data over land. *IEEE Transactions on Geoscience and Remote Sensing* **36** (3), 880–897.

Sirguey, P., R. Mathieu, and Y. Arnaud (2009). Subpixel monitoring of the seasonal snow cover with MODIS at 250m spatial resolution in the Southern Alps of New Zealand: Methodology and accuracy assessment. *Remote Sensing of Environment* **113** (1), 160–181.

Stöckli, R. and P. L. Vidale (2004). European plant phenology and climate as seen in a 20 year AVHRR land-surface parameter dataset. *International Journal of Remote Sensing* **25**, 3303–3330.

Swinnen, E. and F. Veroustraete (2008). Extending the SPOT-VEGETATION NDVI Time Series (1998-2006) Back in Time With NOAA-AVHRR Data (1985-1998) for South Africa. *IEEE Transaction on Geoscience and Remote Sensing* **46**, 558–572.

Trishchenko, A., G. Fedosejevs, Z. Li, and J. Cihlar (2002a). Trends and uncertainties in thermal calibration of the AVHRR radiometers onboard NOAA-9 to -16. *Journal of Geophysical Research* **107**.

Trishchenko, A. P. (2002). Removing unwanted fluctuations in the AVHRR thermal calibration data using robust techniques. *Journal of Atmospheric and Oceanic Technology* **19**, 1939–1954.

Trishchenko, A. P. (2006). Solar Irradiance and Effective Brightness Temperature for SWIR Channels of AVHRR/NOAA and GOES Imagers. *Journal of Atmospheric and Oceanic Technology* **23** (2), 198–210.

Trishchenko, A. P. (2009). Effects of spectral response function on surface reflectance and NDVI measured with moderate resolution satellite sensors: Extension to AVHRR NOAA-17, 18 and METOP-A. *Remote Sensing of Environment* **113** (2), 335–341.

Trishchenko, A. P., J. Cihlar, and Z. Li (2002b). Effects of spectral response function on surface reflectance and NDVI measured with moderate resolution satellite sensors. *Remote Sensing of Environment* **81** (1), 1–18.

Trishchenko, A. P., Y. Luo, and K. V. Khlopenkov (2006). A method for downscaling MODIS land channels to 250 m spatial resolution using adaptive regression and normalization. In *Proceedings of SPIE - The International Society for Optical Engineering*, Volume v.6366, pp. 8.

Trishchenko, A. P., Y. Luo, K. V. Khlopenkov, W. M. Park, and S. Wang (2009). Arctic circumpolar mosaic at 250 m spatial resolution for IPY by fusion of MODIS/TERRA land bands B1-B7. *International Journal of Remote Sensing* **30** (6), 1635–1641.

Tucker, C. J. (1979). Red and Photographic Infrared Linear Combinations for Monitoring Vegetation. *Remote Sensing of Environment* **8**, 127–150.

Tucker, C. J., J. E. Pinzon, M. E. Brown, D. A. Slayback, E. W. Pak, R. Mahoney, E. F. Vermote, and N. E. Saleous (2005). An extended AVHRR 8-km NDVI dataset compatible with MODIS and SPOT vegetation NDVI data. *International Journal of Remote Sensing* **26** (20), 4485–4498.

Vermote, E. (1995). Absolute calibration of AVHRR visible and near-infared channels using ocean and cloud views. *International Journal of Remote Sensing* **16**, 2317–2340.

Vermote, E. and N. Saleous (2006). Calibration of NOAA16 AVHRR over a desert site using MODIS data. *Remote Sensing of Environment* **105** (3), 214–220.

Voigt, S. (2000). *Advanced methods for operational mapping of Alpine snow cover using medium resolution optical satellite data*. Inauguraldissertation, Universität Bern.

Walton, C. C., J. T. Sullivan, C. R. N. Rao, and M. P. Weinreb (1998). Corrections for detector nonlinearities and calibration inconsistencies of the infrared channels of the Advanced Very High Resolution Radiometer. *Journal of Geophysical Research* **103** (C2), 3323–3337.

Weiss, D. J. and S. J. Walsh (2009). Remote Sensing of Mountain Environments. *Geography Compass* **3** (1), 1–21.

Wildeisen, A. (2008). Cloud Masking over Central Europe using NOAA AVHRR Data. A Comparison of the Performance of the Cloud Mask Schemes CASPR and SAFNWC/PPS. Master's thesis, University of Bern, Switzerland.

Wolfe, R., J. Storey, E. Masuoka, and A. Fleig (1995). MODIS Level 1A Earth Location Algorithm Theoretical Basis Document. Available online at: http://modis.gsfc.nasa.gov/.

Wolfe, R. E., M. Nishihama, A. J. Fleig, J. A. Kuyper, D. P. Roy, J. C. Storey, and F. S. Patt (2002). Achieving sub-pixel geolocation accuracy in support of MODIS land science. *Remote Sensing of Environment* **83** (1-2), 31–49.

Xiong, J., G. Toller, V. Chiang, J. Sun, J. Esposito, and W. Barnes (2005). MODIS level 1B algorithm theoretical basis document. Available online at: http://modis.gsfc.nasa.gov/.

Xiong, X., K. Chiang, B. Guenther, and W. L. Barnes (2003a). MODIS thermal emissive bands calibration algorithm and on-orbit performance. In H. Huang, D. Lu, and Y. Sasano (eds.), *Optical Remote Sensing of the Atmosphere and Clouds III*, Volume 4891 of *Proceedings of the SPIE*, pp. 392–401.

Xiong, X., J. Sun, J. A. Esposito, B. Guenther, and W. L. Barnes (2003b). MODIS reflective solar bands calibration algorithm and on-orbit performance. In H. Huang, D. Lu, and Y. Sasano (eds.), *Optical Remote Sensing of the Atmosphere and Clouds III*, Volume 4891 of *Proceedings of the SPIE*, pp. 95–104.

Chapter 3

Impact of orthorectification and spatial sampling on maximum NDVI composite data in mountain regions

Fabio M. A. **Fontana**[1], Alexander P. **Trishchenko**[2], Konstantin V. **Khlopenkov**[2,3], Yi **Luo**[2,4], Stefan **Wunderle**[1]

[1] *Institute of Geography and Oeschger Centre for Climate Change Research, University of Bern, Switzerland*

[2] *Canada Centre for Remote Sensing, Ottawa, Canada*

[3] *Science Systems and Applications, Inc., Hampton, VA, United States*

[4] *Canadian Ice Service, Ottawa, Canada*

Abstract

Topography and accuracy of image geometric registration significantly affect the quality of satellite data, since pixels are displaced depending on surface elevation and viewing geometry. This effect should be corrected for through the process of accurate image navigation and orthorectification in order to meet the geolocation accuracy for systematic observations specified by the Global Climate Observing System (GCOS)

requirements for satellite climate data records. We investigated the impact of orthorectification on the accuracy of maximum Normalized Difference Vegetation Index (NDVI) composite data for a mountain region in north-western Canada at various spatial resolutions (1 km, 4 km, 5 km, and 8 km). Data from AVHRR on board NOAA-11 (1989 and 1990) and NOAA-16 (2001, 2002, and 2003) processed using a system called CAPS (Canadian AVHRR Processing System) for the month of August were considered. Results demonstrate the significant impact of orthorectification on the quality of composite NDVI data in mountainous terrain. Differences between orthorectified and non-orthorectified NDVI composites (ΔNDVI) adopted both large positive and negative values, with the 1% and 99% percentiles of ΔNDVI at 1 km resolution spanning values between $-0.16<\Delta$NDVI<0.09. Differences were generally reduced to smaller numbers for coarser resolution data, but systematic positive biases for non-orthorectified composites were obtained at all spatial resolutions, ranging from 0.02 (1 km) to 0.004 (8 km). Analyzing the power spectra of maximum NDVI composites at 1 km resolution, large differences between orthorectified and non-orthorectified AVHRR data were identified at spatial scales between 4 km and 10 km. Validation of NOAA-16 AVHRR NDVI with MODIS NDVI composites revealed higher correlation coefficients (by up to 0.1) for orthorectified composites relative to the non-orthorectified case. Uncertainties due to the AVHRR Global Area Coverage (GAC) sampling scheme introduce an average positive bias of 0.02 ± 0.03 at maximum NDVI composite level that translates into an average relative bias of $10.6\%\pm19.1$ for sparsely vegetated mountain regions. This can at least partially explain the systematic average positive biases we observed relative to our results in AVHRR GAC-based composites from the Global Inventory Modeling and Mapping Studies (GIMMS) and Polar Pathfinder (PPF) datasets (0.19 and 0.05, respectively). With regard to the generation of AVHRR long-term climate data records, results suggest that orthorectification should be an integral part of AVHRR pre-processing, since neglecting the terrain displacement effect may lead to important biases and additional noise in time series at various spatial scales.

3.1 Introduction

3.1.1 Overview

Mountain regions cover approximately one fourth of the Earth's surface (Kapos et al., 2000) and are known to be particularly sensitive to climate change (Beniston, 2003). Due to the strong altitudinal gradients many mountain regions provide unique opportunities to detect and analyze global change processes and phenomena on small horizontal scales. In this regard, remote sensing data represent a valuable source of in-
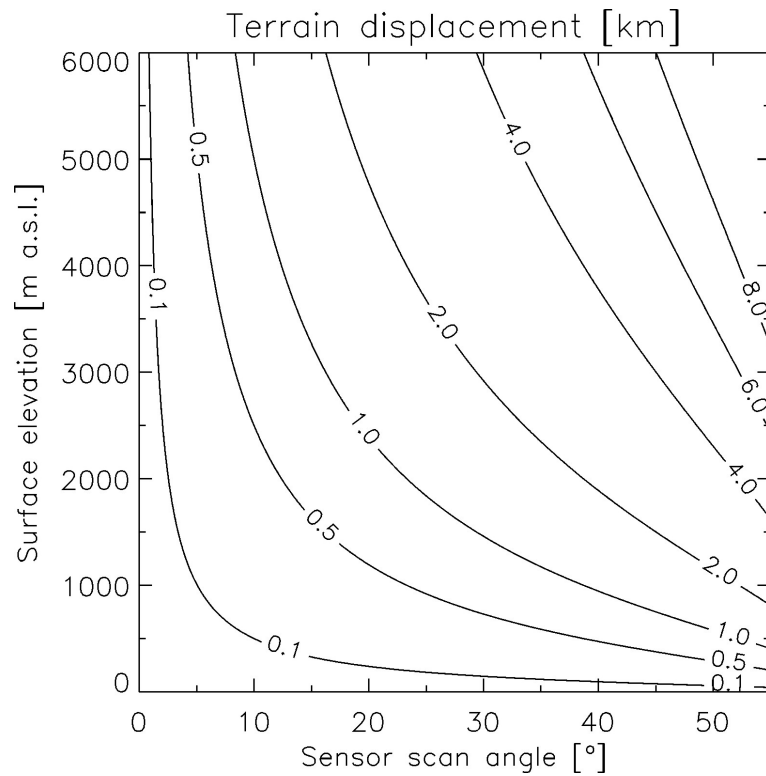
Figure 3.1: *Terrain displacement [km] depending on the observation geometry and the elevation of the observed target. Analysis is constrained to the approximate elevation range found in North America and considers the range of possible sensor scan angles of AVHRR (0°-55°; adopted and modified from Voigt, 2000).*

formation, most importantly for investigations at broad spatial scales (Bugmann et al., 2007). For long-term analyses of various biophysical surface parameters the global archive of the National Oceanic and Atmospheric Administration (NOAA) Advanced Very High Resolution Radiometer (AVHRR) data is of particular interest. However, the topography is recognized as a substantial source of uncertainty in AVHRR data (and satellite data in general). Not only does topography influence the radiometric characteristics of a surface observed from AVHRR, but also has a distinct effect on image geometric accuracy (Running et al., 1994; Wolfe et al., 2002). Geometric image distortions due to the relief of the Earth's surface occur along the AVHRR scan line, resulting from the intertwined effects of observation geometry and terrain elevation. The impact of topography on image geometric accuracy for a standard AVHRR viewing geometry is outlined in Figure 3.1. The terrain displacement, or orthoshift, may amount up to several kilometers for elevated targets depending on the sensor scan angle (Voigt, 2000; Eidenshink and Faundeen, 1994), where the displacement (Δx)

for a certain surface elevation (h) is defined as

$$\Delta x = \frac{h}{\tan \beta} \qquad (3.1)$$

with β=satellite elevation angle, which in turn is defined as

$$\beta = 90 - \alpha - \gamma \qquad (3.2)$$

with α=sensor scan angle and γ=geocentric angle between satellite and pixel location (Voigt, 2000). At terrain elevations of 2000 m a.s.l., for example, sensor scan angles of 30° result in an orthoshift of more than 1 km across track (Figure 3.1). However, the Global Climate Observing System (GCOS) report on systematic observation requirements for satellite-based products for climate (GCOS, 2006) requests that geolocation accuracy of remote sensing products should be better than 1/3 of the sensor instantaneous field of view (IFOV). Given the nominal spatial resolution of the AVHRR sensor at nadir (1.1 km), the requested geometric accuracy is not achieved. The orthoshift as outlined above can be corrected through the process of orthorectification, yet only very few of the known AVHRR processing systems account for surface elevation through the orthorectification procedure. The terrain displacement as illustrated in 3.1 is likely to have an impact on the accuracy of multi-date composite data. Along with other potential sources of error in composite data (described in Section 3.1.2), this image distortion potentially leads to a misinterpretation of satellite data records, since any surface pattern under investigation may become unidentifiable due to the image-to-image shift of elevated pixels. However, the impact of pronounced topography on the geometric accuracy of AVHRR derived long-term climate data records has not yet been adequately addressed and hence, this effect should be analyzed particularly with regard to future remote sensing studies dealing with broad scale phenomena in mountainous terrain. A common application of long-term AVHRR data is the analysis of vegetation activity using maximum Normalized Difference Vegetation Index (NDVI) composite data (described in detail in Section 3.1.2). The NDVI is calculated from the reflectance in the visible and near infrared bands (AVHRR bands 1 and 2) of the electromagnetic spectrum and is a measure of the photosynthetic activity within the area covered by a pixel (Tucker and Sellers, 1986). Due to the regionally and temporally limited data availability, only relatively few studies have analyzed long-term NDVI time series at the full spatial resolution of AVHRR (e.g. Udelhoven and Stellmes, 2007; Pouliot et al., 2009). The majority of the long-term studies on vegetation dynamics at global (Moulin et al., 1997), hemispherical (Myneni et al., 1997), continental (Delbart et al., 2006), and regional scales including mountain ranges such as the European Alps (Stöckli and Vidale, 2004) make use of reduced spatial resolution Global Area Coverage (GAC) AVHRR NDVI datasets from the Global Inventory Modeling and

Mapping Studies (GIMMS; Tucker et al., 2005) or from the Pathfinder AVHRR Land (PAL) project (James and Kalluri, 1994). GAC data are sampled on board the satellite in real-time to produce reduced resolution data. This is achieved by computing an average value from four out of five pixel samples along a scan line and by eliminating two out of three scan lines (Kidwell, 1998). The resulting product has a spatial resolution of 1.1 km 4 km at the sub-satellite point with a 3 km distance between pixels across the scan line. Hence, GAC values are representative of a 3 km×5 km area, even though GAC-based products are generally resampled to a 4 km, 5 km, or 8 km grid. In spatially heterogeneous areas such as many mountain regions of the world, the spatial sampling scheme inherent in the GAC data was found to result in a limited representation in comparison to other sampling schemes (Justice et al., 1989). Hence, with regard to the future use of GAC based NDVI data for studies of spatially heterogeneous mountain regions, potential errors due to the GAC sampling scheme should be analyzed. The paper is organized as follows: In the following section we expand on a number of issues relevant for the generation and analysis of maximum NDVI composite datasets. In Section 5.2 we give an overview of the data and the applied processing steps as well as of the geographical area under investigation. The influence of orthorectification on AVHRR maximum NDVI composite data at 1 km, 4 km, 5 km, and 8 km spatial resolution is analyzed in Section 3.3.1. Section 3.3.2 presents results of a validation with precisely georeferenced MODIS maximum NDVI composite data. Finally, with regard to the common use of GAC-based NDVI datasets in long-term vegetation studies, results are related to the 5 km Polar Pathfinder AVHRR dataset (hereafter referred to as PPF AVHRR) as well as the 8 km GIMMS NDVI dataset in Section 3.3.3, and the uncertainty in maximum NDVI composite data due to the GAC sampling scheme is analyzed. Section 6 summarizes the research.

3.1.2   Generation of composite datasets

Selecting the pixels with the highest quality from multiple scenes within a predefined time interval and merging them into a composite image is a commonly used technique. The goal of this compositing process is to create clear-sky composites with reduced contamination due to clouds and atmospheric constituents. Among other compositing procedures such as the minimum near infrared band value compositing (Fraser and Li, 2002) or the maximum surface temperature compositing method (Cihlar et al., 1994), the maximum NDVI technique (Holben, 1986) is the most widely used compositing technique for studies on the terrestrial vegetation although it may still lead to some biases (Luo et al., 2008). The maximum NDVI is selected within a predefined time interval based on the assumption that NDVI values are reduced by the

presence of clouds or by the influence of atmospheric constituents such as water vapor and aerosols on the measured reflectance in AVHRR bands 1 and 2 (Holben, 1986). Compositing interval lengths for AVHRR data typically vary between 5 to 7 days and up to 30 days depending on the application; however, a minimum interval length of 10 days is usually selected in order to increase the chance of a geographic location being observed under clear-sky conditions. Still, cloud contamination may be present in maximum NDVI data in areas of persistent cloud cover. Reflectances in AVHRR bands 1 and 2 are not only influenced by the composition of the atmosphere, but also by the surface angular anisotropy described by the bidirectional reflectance distribution function (BRDF) of the Earth's surface (Cihlar et al., 2004). These effects can be minimized by constraining the range of relative azimuth angles considered during a compositing interval (Luo et al., 2008) or by normalizing the measured reflectances to standard viewing conditions using BRDF models (Bacour et al., 2006). Although it was demonstrated that BRDF effects are reduced through the calculation of vegetation indices such as the NDVI (Lee and Kaufman, 1986), maximum NDVI composites may still contain spatial noise due to the variable observation geometry, cloud shadow contamination and other effects (Luo et al., 2008). Another issue relevant for the analysis of NDVI composite data is the accuracy of image geolocation. Instead of comparing the NDVI of a given location at two different points in time, diverse locations are compared at a certain image coordinate, if consecutive images within a compositing interval are not accurately co-registered (Townshend et al., 1992). High image geolocation accuracy is usually achieved by a combination of two different steps: pixel location prediction using a satellite orbital model and a chip matching procedure using ground control points (GCPs; Cracknell, 1997. Geolocation schemes for NOAA AVHRR solely based on information from satellite orbital models will result in an accuracy of 1-4 km at the sub-satellite point (Rosborough et al., 1994), which is insufficient for the creation of high-quality NDVI composites and does not meet the GCOS requirements for satellite climate data records. With regard to the generation of AVHRR-based long-term climate data records, above mentioned sources of uncertainty in composite data have repeatedly been analyzed. However, the eventual quality gain due to the implementation of orthorectification has not yet been quantified and we, therefore, make an attempt to assess the impact of orthorectification on maximum NDVI composites at various spatial scales. This could finally lead to a better applicability of long-term AVHRR data time series for climate change studies in mountainous regions. To achieve this goal, we make use of the newly developed AVHRR processing software at the Canada Centre for Remote Sensing (CCRS), the Canadian AVHRR Processing System (CAPS; Khlopenkov et al., 2009), which can optionally disable orthorectification and thereby allows us to quantify the terrain displacement effects in composite data.

3.2   Data and methods

3.2.1   AVHRR data

To assess the impact of accurate geolocation and orthorectification on the quality of maximum NDVI composite data, we use the 1 km AVHRR dataset hosted at the CCRS, which covers the entire area of Canada and parts of the Unites States since 1981 (Latifovic et al., 2005). In addition, this local coverage dataset is compared to two freely available GAC based datasets: the PPF AVHRR dataset (5 km; circumpolar coverage), and the GIMMS NDVI dataset (8 km; global coverage). A short overview of all three AVHRR datasets is given in the following sections.

CCRS AVHRR product

AVHRR data from two different satellites were chosen: historical data from the AVHRR/2 sensor aboard NOAA-11 in August 1989 and 1990 as well as more recent data from the AVHRR/3 sensor aboard NOAA-16 in August 2001, 2002, and 2003. These periods were selected to avoid the possible impact of aerosol contamination due to the Pinatubo eruption in 1991 and to be able to compare the AVHRR data in 2001 to 2003 against MODIS observations. In addition, the month of August provides a good opportunity for clear-sky observations and represents close to minimum snow and ice coverage conditions in the mountains. Pre-processing was performed using the CAPS software (Khlopenkov et al., 2009). CAPS performs geolocation based on a GCP refining procedure in native swath projection, and determining the satellite state vector and sensor attitude angles to achieve the best fits. Geolocation accuracy is generally better than 1/3 of the pixel size, with seasonally varying MODIS composite imagery being used as reference maps for image chip matching. The procedure as proposed in Khlopenkov and Trishchenko (2008) was used to remap the AVHRR data to the Lambert Conformal Conic (LCC) projection, which is the standard projection used at the CCRS for national scale coverage (Latifovic et al., 2005). In addition, CAPS includes orthorectification in image swath projection based on a 250 m digital elevation model (DEM) in order to account for the influence of surface elevation. Details on the orthorectification procedure can be found in Khlopenkov et al. (2009). Orthorectification can optionally be turned off in the CAPS software, which enables us to isolate the effect of orthorectification on the data. Hence, all AVHRR data were processed twice, once including orthorectification, and once not taking into account terrain displacement. In the following, NDVI data that originate from CAPS, where orthorectification was included, are named $NDVI_O$, in contrast to data that do not include orthorecti-

fication (NDVI$_{NO}$). In order to account for differences in the spectral response function (SRF) between the two considered AVHRR sensors, data from NOAA-16 AVHRR/3 were normalized to NOAA-9 AVHRR/2 using the correction functions as proposed by Trishchenko et al. (2002). These correction functions have previously been shown to significantly improve the consistency between the NDVI from various AVHRR sensors as well as in comparison with Système Pour l'Observation de la Terre (SPOT) VEGETATION NDVI data (Swinnen and Veroustraete, 2008). NOAA-11 AVHRR/2 data were not normalized to NOAA-9 AVHRR/2 since the differences in SRF between both are minor, and hence, the correction is optional (Trishchenko et al., 2002). Bimonthly maximum NDVI composites were computed from the 1 km spatial resolution input data, which results in a 15-day (day 1-15) and a 16-day composite (day 16 to the end of the month). All observations with view zenith angles (VZA) of VZA>55° were excluded. Additionally, data that were obtained at sun zenith angles (SZA) of SZA>80° were not considered to avoid artifacts introduced by the proximity to the terminator line. In order to identify the impact of orthorectification on coarse resolution data, maximum NDVI composites were also computed for three coarse resolution AVHRR datasets (4 km, 5 km, and 8 km) that were generated based on the 1 km dataset by averaging the adequate number of pixels. Cloud contamination information was obtained from the Separation of Pixels Using Aggregated Rating over Canada (SPARC) algorithm (Khlopenkov and Trishchenko, 2007). The SPARC algorithm combines several tests and outputs a cloudiness index (CI), which can be regarded as a measure of cloud contamination probability for each pixel. A cloudiness index threshold of CI=128 was chosen to separate cloudy from clear conditions.

PPF AVHRR data

The AVHRR Polar Pathfinder (PPF) dataset (Fowler et al., 2007) is available from the National Snow and Ice Data Centre as top of atmosphere (TOA) reflectance values (reflective channels) and brightness temperature (thermal channels). Navigation is based on an orbital ephemeris model with orbit corrections (Rosborough et al., 1994). Data are finally available in a 5 km spatial resolution Equal Area Scalable Earth (EASE) grid for the northern hemisphere, and geolocation accuracy is expected to be approximately 2 km on average. The northern hemisphere dataset was downloaded for the same time periods as described above (Section 3.2.1). Like the AVHRR data from the CCRS archive (Section 3.2.1), the PPF data for August 1989 and 1990 originate from the NOAA-11 AVHRR/2 sensor, data for 2001 to 2003 originate from NOAA-16 AVHRR/3. An SRF correction was applied as described above. Bimonthly maximum NDVI composites were calculated in original EASE grid format, using the same view and solar

zenith angle thresholds as proposed in Section 3.2.1 along with the processing of the CCRS data. Composites were reprojected to the LCC projection before the data for the regions of interest (Section 3.2.3) were extracted. Two different resampling methods, nearest neighbor (NN) and bilinear interpolation (BI), were used for reprojection to create two different datasets in order to account for uncertainties introduced by the resampling process. Cloud information was obtained using two threshold tests: a brightness temperature (T) test in channel 5 (T<0°) and a reflectance (R) test in channel 1 (R>35%). The supplied CASPR cloud product was not used since the output was found to be unreliable for August 1989 and 1990. NDVI data from the PPF dataset will hereafter be referred to as $NDVI_{PPF}$.

GIMMS AVHRR data

The global GIMMS NDVI dataset (Tucker et al., 2005; Pinzon et al., 2005) is available at the University of Maryland Global Land Cover Facility and is one of the most commonly used global datasets to study patterns of vegetation activity on various spatial scales. It has a spatial resolution of 8×8 km^2 and consists of bimonthly maximum NDVI composites. Cloud screening is provided by a band 5 thermal mask of 0°C, and observations at scan angles >40° are excluded. Post-processing of the GIMMS NDVI dataset includes corrections for changes in observation geometry due to satellite orbit drift and other effects not related to changes in vegetation conditions, e.g. distortions caused by persistent cloud cover or sensor intercalibration differences. Geolocation accuracy is assumed to be <1 pixel. The continental dataset for North America was downloaded for August 1989 and 1990, as well as for 2001 to 2003. GIMMS NDVI data for the selected periods originate from the same NOAA satellites as the CCRS AVHRR data. An SRF correction was applied to the NOAA-16 data as described above (Section 3.2.1). Data quality flags are embedded in the NDVI files. Only data were used where the quality flag=0 (good value) and flag=1 (good value, possibly snow). The GIMMS continental datasets are originally provided in Albers Equal Area Conic Projection. Hence, the continental dataset was reprojected to the LCC projection using NN and BI resampling schemes before extracting the geographic regions of interest (Section 3.2.3). NDVI data from the GIMMS dataset will hereafter be referred to as $NDVI_{GIMMS}$.

3.2.2   MODIS processing

Terra MODIS level 1b data for August in 2001, 2002, and 2003 were processed as described in detail in Luo et al. (2008). MODIS pre-processing at the CCRS includes

downscaling of bands B3 to B7 from 500 m to 250 m spatial resolution using adaptive regression and normalization scheme for compatibility with the 250 m bands B1 and B2 (Trishchenko et al., 2006), remapping of the images from swath projection into LCC projection according to Khlopenkov and Trishchenko (2008), and cloud and cloud shadow identification at 250 m spatial resolution based on bands B1, B2, B3, and B6. The NDVI was calculated from bands B1 and B2. In contrast to the clear-sky compositing scheme as proposed in Luo et al. (2008), the maximum NDVI criterion was chosen to create bimonthly composites in order to ensure consistency with the processing of CCRS AVHRR as well as GAC-based NDVI composite data as described above. The 250 m data were aggregated to 1 km, 4 km, 5 km, and 8 km spatial resolution by averaging the appropriate number of pixels. The cloud identification flag for the coarse resolution data was set to "cloudy", if more than half of the contributing 250 m pixels were marked as "cloudy" in the input dataset. In order to account for differences in the SRF, MODIS NDVI composites were normalized to NOAA-9 AVHRR/2 as proposed by Trishchenko et al. (2002). Maximum NDVI composites from MODIS will hereafter be referred to as $NDVI_{MODIS}$.

3.2.3 Geographical regions of interest

Investigations were limited to two regions of interest (ROI) west of Great Bear Lake in the North West Territories, Canada (denoted as black squares in Figure 3.2, top). The ROIs were defined to cover an area of 6400 km^2 (80 pixels×80 pixels) each, which enables us to characterize the orthorectification effect at regional (80 km) as well as at single pixel scale (1, 4, 5, and 8 km). Differences in the geomorphology between both ROIs are clearly apparent in the MODIS clear-sky composite image as displayed in Figure 3.2 (top; Trishchenko, 2009): Sparsely vegetated and spatially heterogeneous ROI/1 within the Mackenzie Mountain Range is characterized by strong altitudinal gradients on small horizontal scales (maximum elevation difference: 1604 m). We, therefore, believe that ROI/1 serves as a good example for a typical mountain region on Earth. ROI/2, on the other hand, mainly covers areas without significant topography west of Great Bear Lake (maximum elevation difference: 534 m) and represents more homogeneous land cover. ROI/2 is chosen as a control in order to demonstrate that the impact of orthorectification on maximum NDVI composites is reduced in topographically more homogeneous and lower laying areas compared to the mountain range (ROI/1). The DEM for both ROIs at 1000 m spatial resolution is displayed in Figure 3.2 (bottom). The DEM was created by combining data from the Canadian Centre for Topographic Information (CTI) and GTOPO30 if CTI data were not available. A summary of the geographic characteristics of both ROIs is provided in Table 5.1.
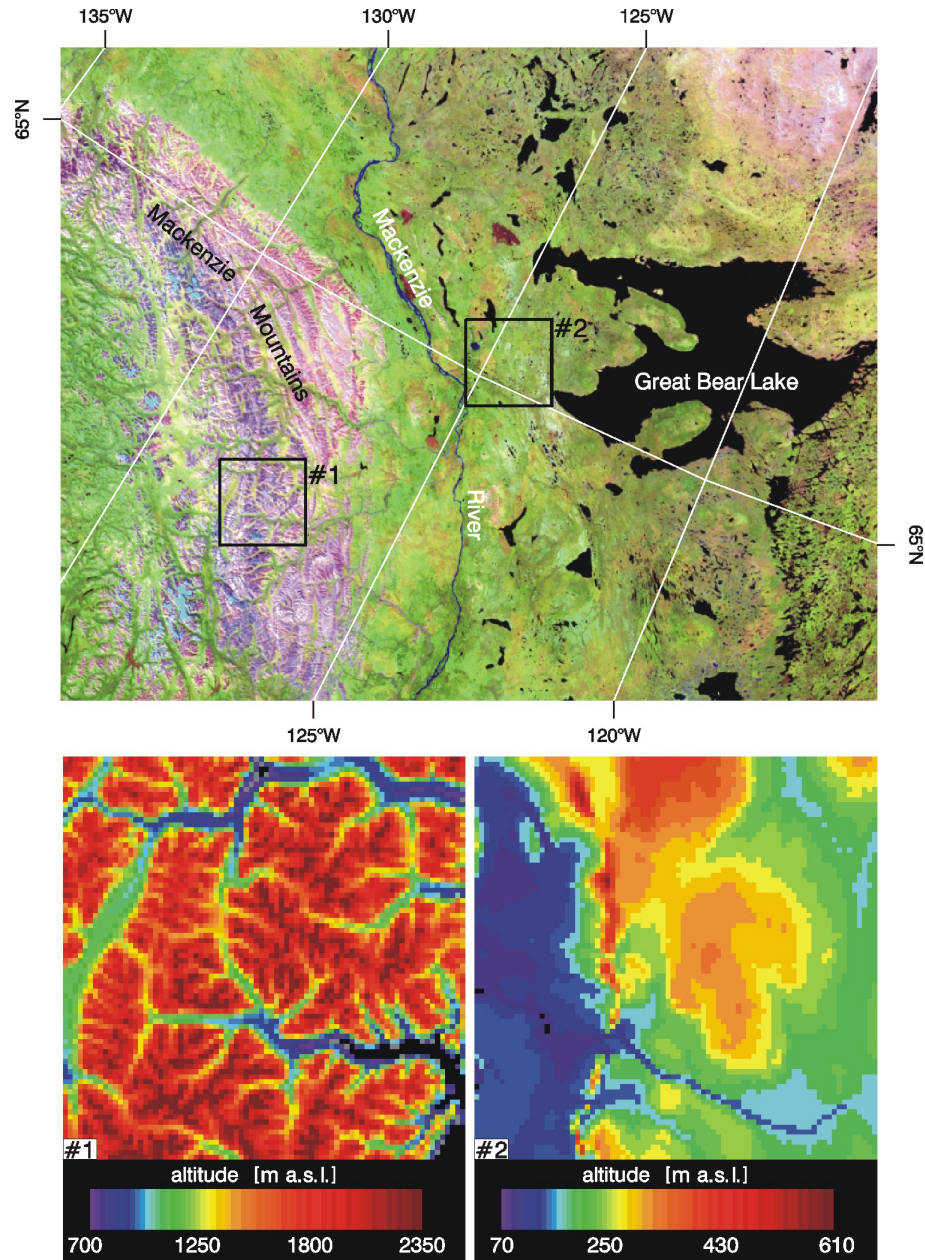
Figure 3.2: *The regions of interest (ROI) selected for the analysis of the maximum NDVI composite data, denoted as black squares in a MODIS clear-sky composite image (top), and as seen in a 1000 m digital elevation model (DEM; bottom). Each ROI covers an area of 6400 km² (80 pixels×80 pixels). RGB color scheme of MODIS composite image: Red - band 6 (1628-1652 nm); Green - band 2 (841-876 nm); Blue - band 1 (620-670 nm).*

3.3 Results and discussion

3.3.1 Comparison of NDVI$_O$ and NDVI$_{NO}$

A difference image of two maximum NDVI composites is displayed in Figure 3.3 for both ROIs, together with the corresponding frequency distribution of the differences.

Table 3.1: *Geographical characteristics of the regions of interest (ROI). Both ROIs have a spatial extent of 6400 km^2 (80×80 1-km pixels). A denotes altitude in meters above sea level.*

	ROI/1	ROI/2
Upper left corner lat/long [°]	63.3 N / 128.7 W	65.4 N / 125.8 W
Lower right corner lat/long [°]	63.0 N / 126.5 W	65.1 N / 123.4 W
A_{min} / A_{max} [m]	704 / 2308	73 / 607
A_{mean} (1 stdev) [m]	1601 (314)	219 (76)

The differences (NDVI$_O$−NDVI$_{NO}$; hereafter referred to as ΔNDVI) are shown for a 1 km spatial resolution composite in August 1990 (day 16 to end of month). Water surfaces as well as missing values due to persistent cloud cover in either of the datasets (NDVI$_O$ or NDVI$_{NO}$) are marked as black areas and are excluded from the analysis. The impact of orthorectification on the maximum NDVI composite image is clearly apparent in ROI/1 (Figure 3.3, top). For the composite shown, NDVI spans values between −0.21< ΔNDVI<0.16, with negative differences dominating (ΔNDVI$_{median}$=−0.016). The underlying topography (cf. DEM in Figure 3.2) is recognizable in the pattern of ΔNDVI, with values around ΔNDVI≈0 in the low-lying valleys and higher absolute values in elevated areas. Similar to the low-lying areas in ROI/1, the range of ΔNDVI is lower in ROI/2 (Figure 3.3, bottom). In contrast to the topographically heterogeneous ROI/1, the histogram of ΔNDVI is symmetrical relative to zero (ΔNDVI$_{median}$=0.0) for ROI/2. The asymmetry towards negative values of ΔNDVI in ROI/1 (where NDVI$_O$ adopts lower values than NDVI$_{NO}$) results from the repeated displacement of elevated pixels into opposite directions during the course of a compositing interval. Due to the nature of the maximum NDVI compositing scheme, higher NDVI values will thereby erroneously be assigned to the geographic location of targets with low NDVI if terrain displacement is not properly accounted for. High NDVI values of certain (elevated) geographical locations are thus duplicated, whereas the extent of areas with low NDVI decreases. If this process is repeated for a number of times, it will finally lead to an increase in the number of pixels, where NDVI$_{NO}$ adopts higher values compared to NDVI$_O$. This is supported by the fact that for ROI/1 the satellite zenith angles considered in the compositing were, on average, significantly larger for non-orthorectified input data (with p<0.01; not shown). This is not the case for ROI/2, where no significant difference between orthorectified and non-orthorectified composites was found in terms of average satellite zenith angles considered. Depending on how often a certain area is observed within a compositing interval, the displacement of low-NDVI areas may also lead to large positive values of NDVI (see Figure 3.3). In ROI/2, non-
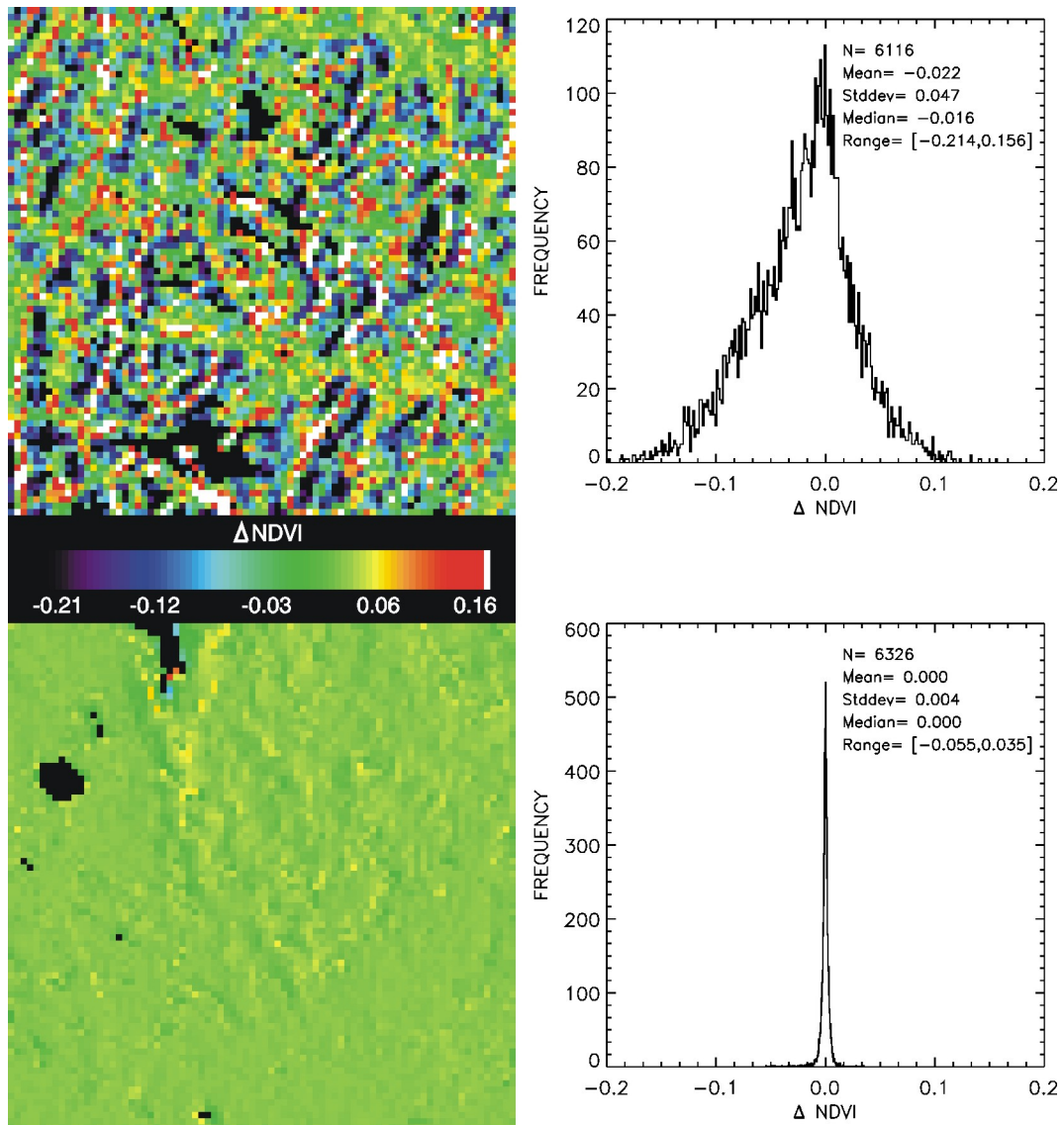
Figure 3.3: *NDVI difference image for the ROIs under investigation (left) and corresponding histograms (right). The differences (NDVI$_O$−NDVI$_{NO}$) are shown for a 1 km spatial resolution maximum NDVI composite in August 1990 (day 16 to end of month). Water surfaces as well as missing values due to cloud cover in either of the datasets (NDVI$_O$ or NDVI$_{NO}$) are marked as black areas and are excluded from the analysis.*

zero differences are observed due to the influence of small scale topography on the geolocation, as seen for the most elevated areas in the centre/north of ROI/2 (see DEM in Figure 3.2). Furthermore, minor pixel shifts in low elevation areas result from the orthorectification process, if the scene to be corrected covers both high and low elevation areas. To analyze the impact of spatial resolution (1 km, 4 km, 5 km, and 8 km) on the distribution of ΔNDVI, the histograms of ΔNDVI for all composites and years are
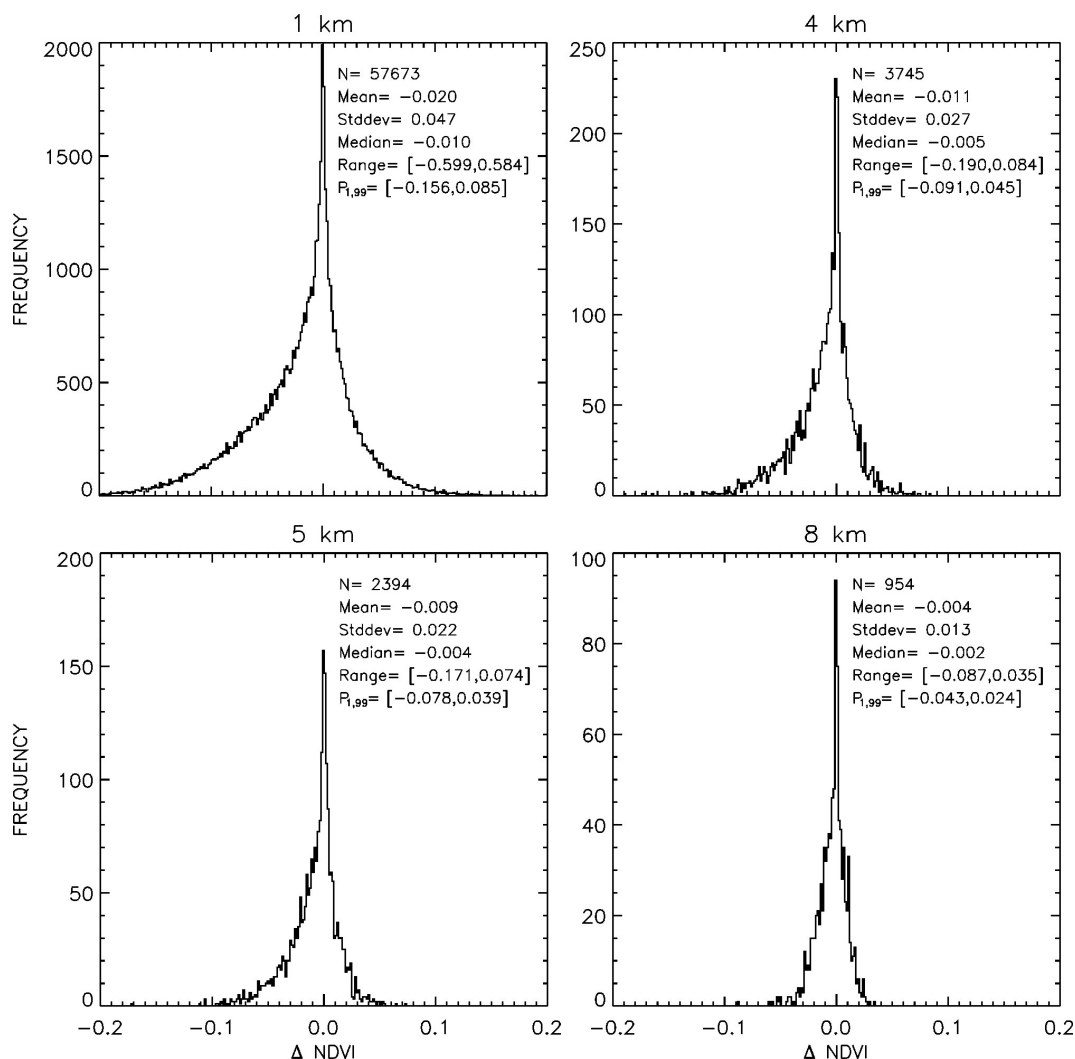
Figure 3.4: *ROI/1 histograms of the differences (ΔNDVI) between orthorectified and non-orthorectified composites for all spatial resolutions. Top: 1 km (left) and 4 km (right). Bottom: 5 km (left), and 8 km (right). Each histogram represents a total of 10 composites. $P_{1,99}$ denotes the 1% and 99% percentiles, respectively. For clarity, the scale of the x-axis is kept constant for all spatial resolutions.*

displayed in Figure 3.4 (10 composites per spatial resolution). Given the good agreement between orthorectified and non-orthorectified composites in ROI/2, results are only shown for ROI/1. Similar to Figure 3.3 (top), histograms for all spatial resolutions are not symmetrical relative to zero. In addition, distributions of ΔNDVI are characterized by large positive and negative values, even though the range of ΔNDVI is clearly reduced if the data are aggregated to coarser resolutions. At 1 km resolution the 1% and 99% percentiles ($P_{1,99}$) correspond to ΔNDVI values of $P_{1,99;1km}=[-0.16, 0.09]$ in contrast to reduced numbers at 8 km resolution ($P_{1,99;8km}=[-0.04, 0.02]$). Aggregation

to larger regions apparently reduces the range of NDVI because pixel values of both $NDVI_O$ and $NDVI_{NO}$ converge as they more closely correspond to the same region, i.e. full-resolution pixels may still remain within the same (coarse resolution) pixel after the orthorectification process. In addition, the range of $\Delta NDVI$ is reduced since the process of aggregation reduces the frequency of occurrence of both high and low NDVI values. The distinct effect of terrain displacement as demonstrated at single pixel scale is of particular relevance for comparative studies of satellite and ground based phenology in complex terrain (Fontana et al., 2008). It likely influences observations of the temporal progression of vegetation development at a certain location as represented by time series of maximum NDVI composites and could thereby lead to biases in the retrieval of phenological parameters, such as the start of season. However, the analysis of the temporal uncertainty introduced to NDVI composite data by the terrain displacement is beyond the scope of the study. Apart from the single pixel scale effects the regional (i.e. ROI) scale effect is also of interest. In view of the asymmetry of the distribution of $\Delta NDVI$, it is, particularly with regard to the regional scale analysis of vegetation activity in mountainous regions, important to determine whether mean NDVI as well as the spatial variability (σ_{NDVI}) differ significantly between orthorectified and non-orthorectified composites. As a result of the overrepresentation of areas with high NDVI as explained above, we would expect mean NDVI to be systematically higher in non-orthorectified imagery. Hence, we compared mean NDVI between orthorectified and non-orthorectified imagery using one-tailed t-statistics for all composites and spatial resolutions, testing the Null-hypotheses H_0: mean $NDVI_{NO} \leq$ mean $NDVI_O$ against the alternative hypotheses H_A: mean $NDVI_{NO} >$ mean $NDVI_O$. In addition, differences in σ_{NDVI} were analyzed using F-test. Results are summarized in Figure 3.5. Statistically significant results (with p<0.01) are indicated with filled symbols in contrast to insignificant results (open symbols). In ROI/1, mean NDVI appeared to be significantly higher in non-orthorectified composites at all spatial resolutions except in one case at 5 km and three cases at 8 km resolution (Figure 3.5; top, left), despite the fact that the effect of terrain displacement diminishes during aggregation to coarser resolutions. By contrast, significantly higher mean NDVI in ROI/2 was only obtained at the 1 km level in six out of ten composites (Figure 3.5; top, right). As discussed above, minor pixel shifts due to orthorectification in nearby mountains as well as small scale topography may lead to the observed differences at the 1 km level in ROI/2. Spatial variability appeared to be less affected by the terrain displacement effect (Figure 3.5, bottom). Significant differences between orthorectified and non-orthorectified imagery were only obtained at the 1 km level in ROI/1. In contrast to the single pixel scale effect characterized by large positive and negative values of $\Delta NDVI$, the regional scale effect of terrain displacement is characterized by a systematic overestimation
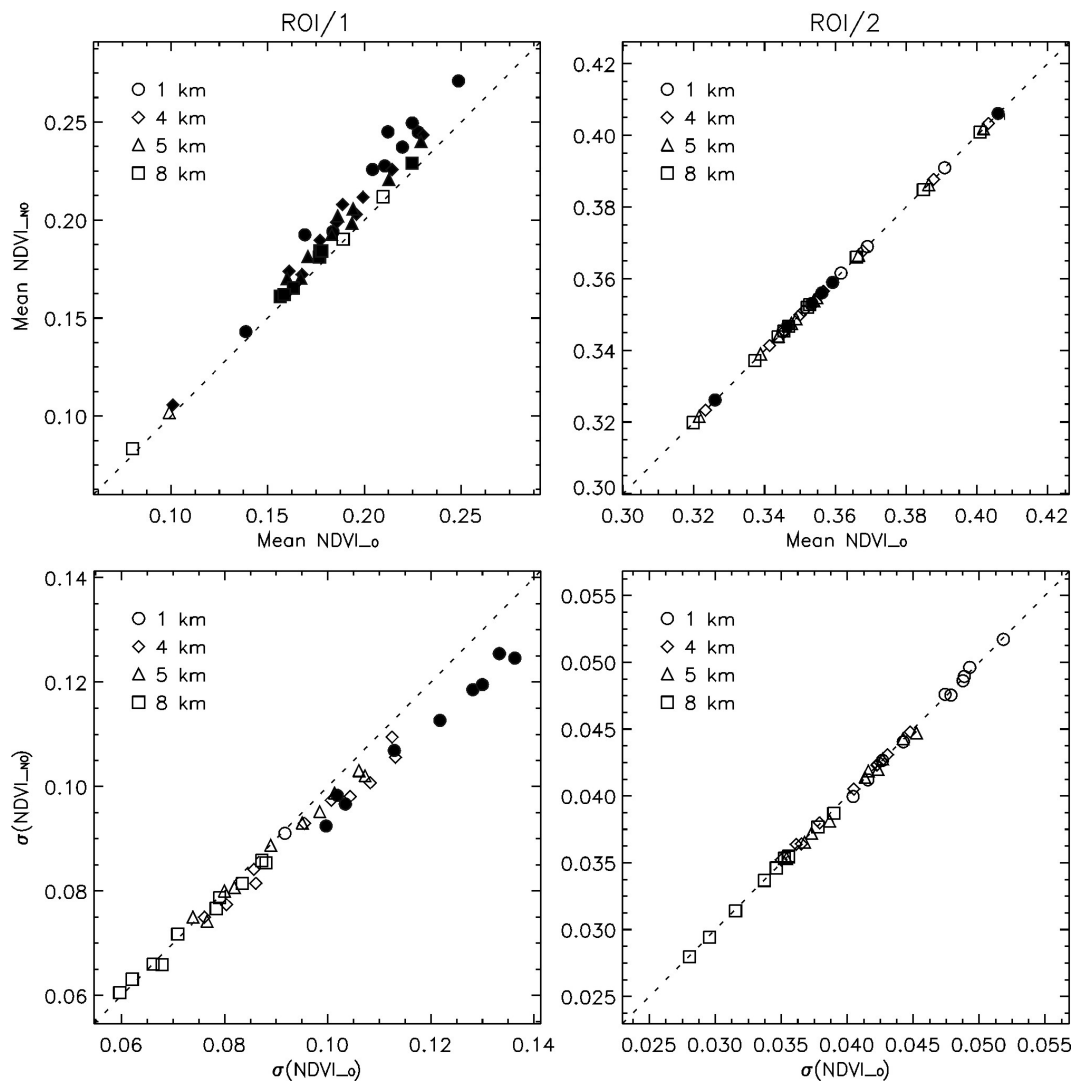
Figure 3.5: *Comparison of mean (top) and standard deviation (σ_{NDVI}; bottom) between NDVI_O and NDVI_NO for ROI/1 (left) and ROI/2 (right). Symbols are filled, where the statistics were found to be significant (p<0.01).*

of mean greenness and associated vegetation photosynthetic activity, represented by significantly higher values of mean NDVI in non-orthorectified composites. This effect could be of interest for studies dealing with the contribution of vegetation to biochemical processes. NDVI datasets have repeatedly served as a basis for the generation of fields of biophysical parameters, such as leaf area index (LAI) or fraction of absorbed photosynthetically active radiation (FPAR; Sellers et al., 1996), which in turn are used to model various soil-vegetation-atmosphere interactions. Hence, inaccurate representation of mean vegetation activity by non-orthorectified composites may lead to a misrepresentation of vegetation in biochemical models in mountainous areas. Results demonstrate that the correction of the pixel displacement in topographically

heterogeneous areas has a significant effect on the maximum NDVI composites both at single pixel and regional scales. The effect is mainly, but not exclusively, observed in areas with significant topography, depending on the spatial resolution of the composite. The next step is thus to validate these findings with precisely georeferenced maximum NDVI composites from the MODIS sensor. These results will be discussed in the following section.

3.3.2 Validation with MODIS maximum NDVI composites

Validation of NOAA-16 AVHRR/3 NDVI data using precisely georeferenced MODIS composites was performed for the month of August in 2001, 2002, and 2003. Linear correlation coefficients (r) were computed between $NDVI_{MODIS}$ on the one hand and $NDVI_{-O}$ and $NDVI_{-NO}$, respectively, on the other hand to get a measure of the spatial coherence of the datasets. In order to account for differences in the performance of the cloud masking schemes between AVHRR and MODIS, pixels were only considered for the comparison if they were flagged as cloud-free in both datasets. Figure 3.6 illustrates the results, showing r for both ROIs including all four spatial resolutions. The size of the '+'-symbols varies according to the percentage of valid values in each ROI and compositing period, resulting from the number of pixels affected by persistent cloud cover. Correlation coefficients for ROI/2 closely follow the 1:1 line (Figure 3.6, right), supporting above findings that in areas without pronounced topography (ROI/2) the implementation of orthorectification only has a marginal influence on the composite data. For a topographically heterogeneous area such as ROI/1 (Figure 3.6, left) correlation coefficients, however, adopt higher values for $NDVI_{-O}$, with $0.00 < \Delta r < 0.11$ ($\Delta r = r_O - r_{NO}$). Correlation coefficients span values between $0.56 < r < 0.99$ for $NDVI_{-O}$, which reflects a generally high level of spatial coherence between MODIS reference imagery and orthorectified output of the CAPS software. In ROI/1, linear correlation coefficients for $NDVI_{-O}$ lower than $r < 0.8$ were solely obtained in one August composite in 2002 (day 16 to end of month), when persistent cloud cover extensively degraded the quality of the maximum NDVI composite and resulted in a low percentage of valid values. In order to visualize the differences between the three NDVI datasets, a MODIS reference composite for ROI/1 is displayed along with orthorectified and non-orthorectified AVHRR NDVI composites at 1 km spatial resolution (days 1-15 in August, 2003) in Figure 3.7. Low-NDVI areas (dark surfaces in Figure 3.7) are diminished and high-NDVI areas are expanded in non-orthorectified composites (middle) compared to both, orthorectified AVHRR (left) and MODIS composites (right). This is again in good agreement with findings in Section 3.3.1, where higher mean NDVI values were obtained for non-orthorectified composites. Visually, local scale
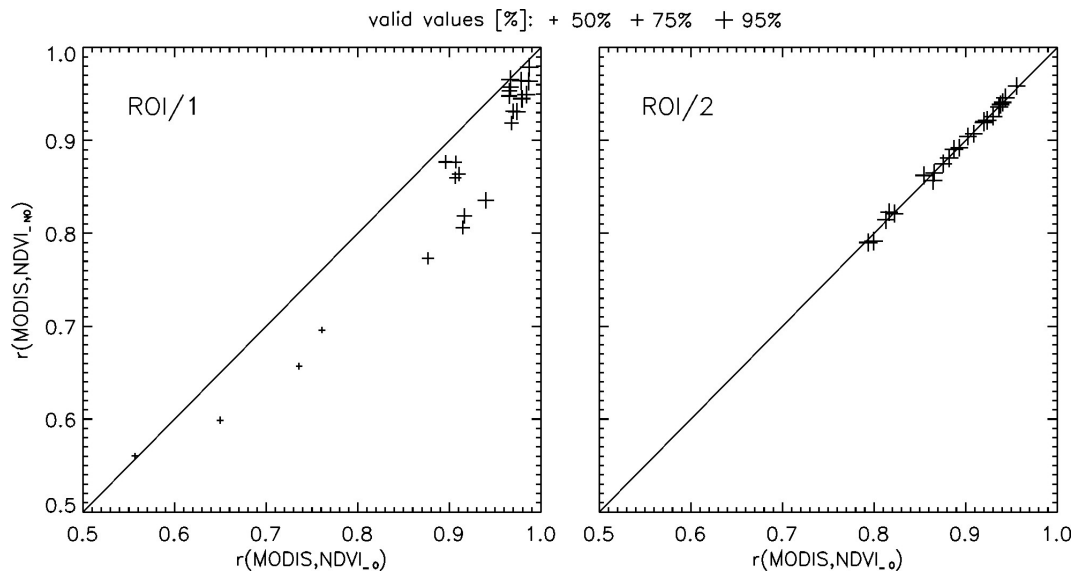
valid values [%]: + 50% + 75%   + 95%

Figure 3.6: *Linear correlation coefficients (r) for ROI/1 (left) and ROI/2 (right) and all spatial resolutions in August 2001, 2002, and 2003. X-axis: Coefficients between NDVI$_{MODIS}$ and NDVI$_{O}$. Y-axis: Coefficients between NDVI$_{MODIS}$ and NDVI$_{NO}$. The size of the '+'-symbols varies according to the percentage of valid values in each ROI and compositing period. Three percent levels (50%, 75%, and 95%) are provided as a reference.*
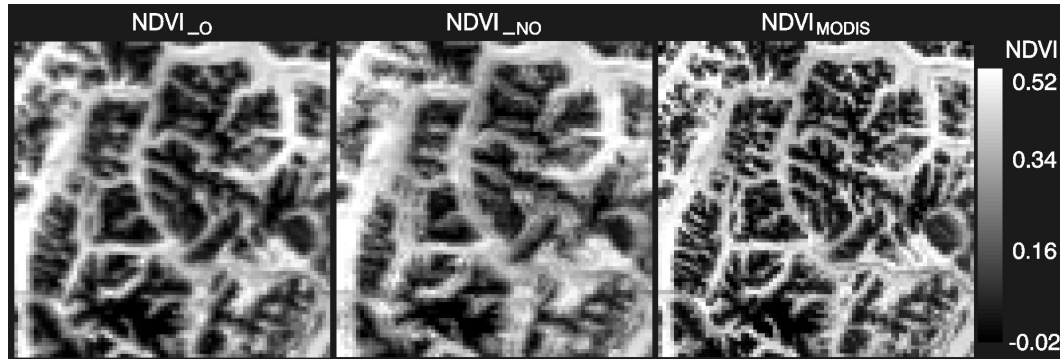

Figure 3.7: *ROI/1 as seen in a 1 km maximum NDVI composite in August 2003 (days 1-15), including orthorectification (NDVI$_{O}$; left), without (NDVI$_{NO}$; middle), and as seen in a MODIS 1 km composite for the same period (NDVI$_{MODIS}$; right). Dark surfaces, indicating low NDVI values, are clearly diminished in the subset that does not include orthorectification (middle).*

topographical features such as valleys and ridges with a horizontal extent of a few kilometers are more clearly represented in orthorectified composites compared to the non-orthorectified case. To quantify this effect, we performed a Fourier transform of all three displayed maximum NDVI composites in Figure 3.7 and analyzed the integral of the power spectra of each composite after applying a series of circular cut high pass
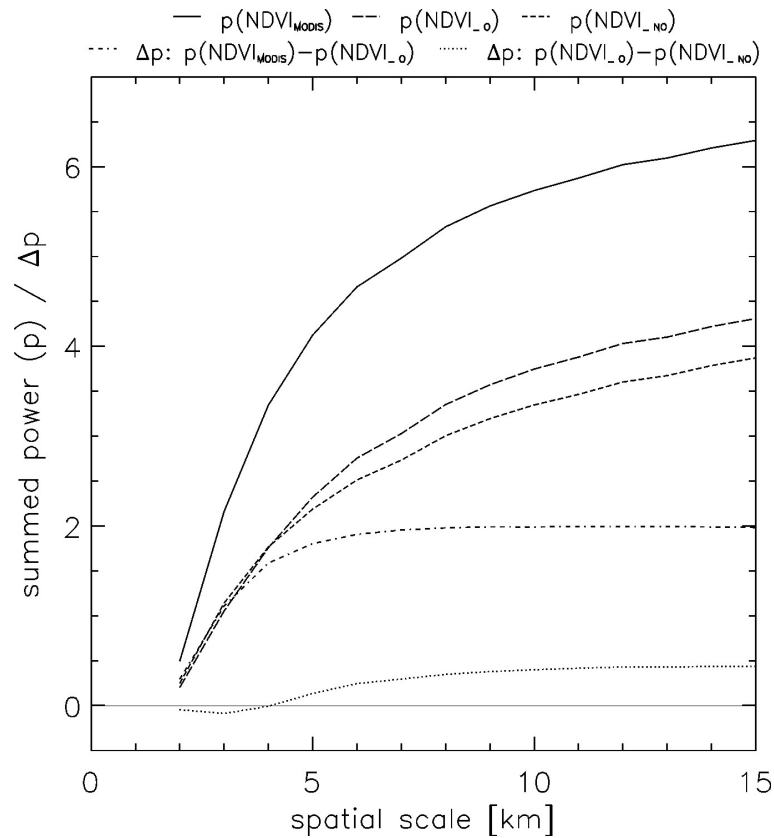
Figure 3.8: *Summed power (p) of three maximum NDVI composites (NDVI_O, NDVI_NO, and NDVI_MODIS; Figure 3.7) after the application of high pass filters with cut-off values correspond-ing to various spatial scales. For clarity, differences in summed power (Δp) between NDVI_MODIS and NDVI_O and between NDVI_O and NDVI_NO are also provided.*

filters. For the high pass filters, we chose cut-off values corresponding to spatial scales from 2 km to 15 km. The results are presented in Figure 3.8. In terms of summed power after filtering NDVI$_{MODIS}$ clearly exceeds both AVHRR composite images. Major differences arising for spatial scales smaller than ca. 5 km indicate a high level of small scale spatial information contained in MODIS composite imagery relative to AVHRR composites. Differences in summed power were, however, also obtained between NDVI$_O$ and NDVI$_{NO}$: while the differences were found to be minor for small spatial scales (<4 km), they distinctly increase for spatial scales between 4 km and 10 km with the summed power of filtered NDVI$_O$ being larger compared to that of filtered NDVI$_{NO}$; at spatial scales larger than 10 km differences remain constant, meaning that the summed power for these spatial scales is identical in both images. These results based on a single composite again confirm that local scale topographical features at spatial scales between 4 km and 10 km are more clearly represented in orthorecti-fied composites and point at the necessity of orthorectification being an integral part

of data pre-processing in studies concerning topographically heterogeneous areas. In rugged terrain, spatial NDVI patterns can only be preserved from scene level up to composite level if terrain displacement is accounted for. Given the good agreement with MODIS reference composites and the improved representation of local scale land surface features by NDVI$_{O}$, we believe that the results provided here represent an important step towards the generation of high quality satellite climate data records for mountain regions on the North American land mass. Beyond that, the newly developed CAPS algorithm (Khlopenkov et al., 2009) could basically be applied to any geographical area on Earth to pre-process long term AVHRR data records, given that an archive of full spatial resolution AVHRR data is available. So far, only results based on 1 km AVHRR data and coarse resolution data created through aggregation of the 1 km data have been presented. However, most of the studies dealing with the analysis of vegetation activity on large spatial scales make use of GAC-based data, since they uniquely provide long-term coverage at global scale. We, therefore, relate above findings to GAC data from both PPF and GIMMS archives in the following section and address the GAC sampling scheme and its influence on NDVI data in more detail.

3.3.3 Comparison with GAC-based datasets

For the comparison with GAC-based datasets we chose aggregated orthorectified imagery from the CCRS archive (NDVI$_{O}$) and confined the analyses to ROI/1. Results are displayed in Figure 3.9 for the 5 km spatial resolution PPF data (left) and 8 km GIMMS data (right). Pixels were only considered for the comparison if they were flagged as cloud-free in both datasets. Histograms of the difference images (ΔNDVI=NDVI$_{O}$−NDVI$_{PPF/GIMMS}$) are displayed for data that were reprojected using NN (solid line) and BI algorithm (dotted line). Similar to the pattern obtained for the comparison of NDVI$_{O}$ and NDVI$_{NO}$ (Section 3.3.1), the majority of the ΔNDVI values were negative (ΔNDVI$_{median}$<0) for both PPF and GIMMS datasets, but the standard deviation of ΔNDVI was higher. In contrast to the distribution of ΔNDVI$_{PPF}$, which adopted both large positive and negative values with a systematic average positive bias for NDVI$_{PPF}$ of 0.05 for both datasets (NN and BL resampling scheme), ΔNDVI$_{GIMMS}$ values were almost exclusively negative, representing significant differences in the magnitudes of NDVI$_{O}$ and NDVI$_{GIMMS}$ (systematic average positive bias for NDVI$_{GIMMS}$ of 0.19). Since both NDVI$_{PPF}$ as well as NDVI$_{GIMMS}$ originate from GAC data, the difference in the magnitude of the systematic bias is assumed to be due to the post-processing as outlined in Section 3.2.1, which is included in the GIMMS data in order to correct the NDVI for effects not related to changes in vegetation. Users of GIMMS data are asked to use the data with caution (Global Inventory Modeling and
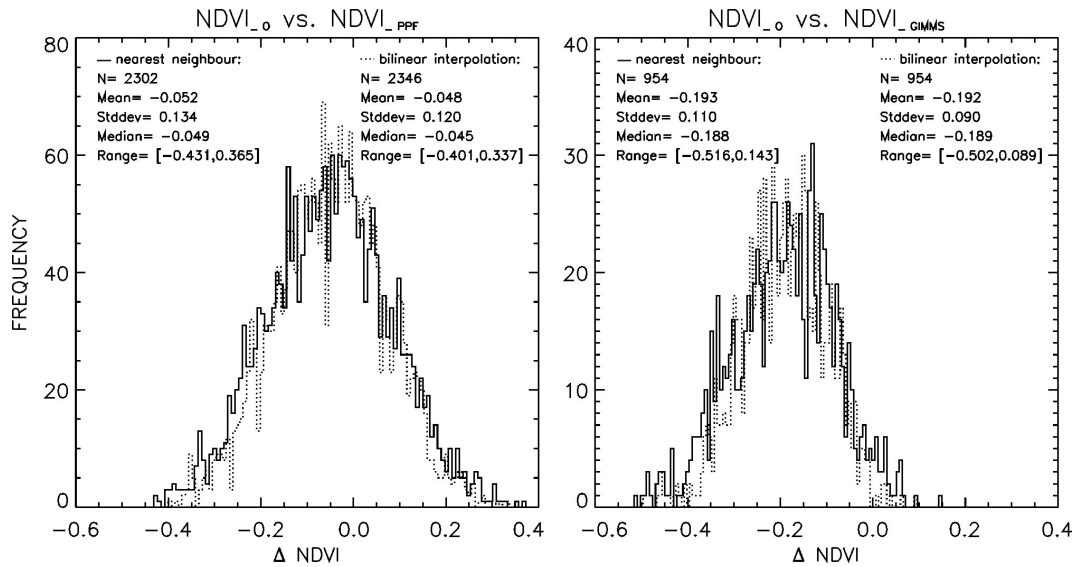
Figure 3.9: *Histograms of the differences (ΔNDVI) between orthorectified AVHRR data (NDVI_O) and Global Area Coverage (GAC) data from PPF (NDVI_PPF; left) and GIMMS (NDVI_GIMMS; right), with ΔNDVI=NDVI_O−NDVI_PPF/GIMMS. Histograms are shown for ROI/1 NDVI data that were reprojected using nearest neighbor (solid line) and bilinear interpolation algorithm (dotted line). Each histogram represents a total of 10 composites.*

Mapping Studies (GIMMS), 2007), since they present generalized vegetation patterns and may therefore be of limited value for studies at local scales. Nevertheless, the strong systematic positive bias of NDVI_GIMMS was somewhat surprising. In general, three factors contribute to the observed differences between NDVI_O and GAC-based datasets. First, uncertainties in the accuracy of geolocation in the GAC datasets should be considered. As a consequence of the spatial degradation of GAC data due to the onboard sampling scheme (Section 3.1.1), geolocation schemes for GAC data do not include chip matching and are primarily based on orbital models. Even though Fowler et al. (2007) expect sub-pixel accuracy in the geolocation of the PPF data, in certain cases we observed image-to-image offsets of up to 2 pixels (i.e. in the range of 10 km; not shown). No obvious shifts were found for the GIMMS data, however, geolocation accuracy of 1 pixel at 8 km level (Tucker et al., 2005) likely adds to the discrepancies in a spatially heterogeneous area such as ROI/1. Second, as a result of these geolocation uncertainties GAC data do not include orthorectification. This again leads to the effects in maximum NDVI composite data as outlined in the previous sections. Third, the GAC sampling scheme itself as outlined in Section 3.1.1 is a potential source of systematic biases in NDVI composite data and will be addressed in more detail below. To quantify the impact of the GAC sampling scheme on the NDVI in ROI/1 both at single scene as well as at multi-date (i.e. composite) level, we conducted a separate

analysis. For the analysis at scene level, we chose a NOAA-16 AVHRR clear-sky scene on August 29, 2003, whereas composite level analysis was performed for the 16-day period from August 16 to the end of the month in August 2003. In order to isolate the GAC sampling effect from the terrain displacement effect, we selected orthorectified imagery for the analysis. Within the 80×80 km^2 ROI/1, 20 locations were randomly chosen as a starting point for the analysis. At scene level, a "true" mean NDVI was calculated at each of these locations based on aggregated 4×4 km2 AVHRR band 1 and band 2 input data (i.e. including all 1 km pixels in the calculation of the coarse resolution NDVI). Even though a single GAC sample represents an area of 5×3km^2, GAC data resolution is often assumed to be 4 km, and we, therefore, chose to perform the analysis at 4 km level. GAC AVHRR band 1 and 2 data were subsequently calculated by simulating an AVHRR scan line within the 4×4 km^2 area, i.e. by averaging four neighboring 1 km pixels at a time. By doing this (4 rows, 4 columns, and 2 diagonals), a total number of 10 simulated GAC NDVI values was calculated per 4×4 km^2 area. For the multi-date analysis, we identified the maximum NDVI for the same locations during the compositing interval. Here again, "true" maximum NDVI values (based on aggregated data) were compared to 10 simulated GAC maximum NDVI values. For the determination of the maximum GAC NDVI during a compositing interval, we created 10 different 16-day NDVI time series at each location by averaging the neighboring pixels in a randomly chosen AVHRR scan line (as described above) for each satellite overpass (10 iterations). Results are displayed in Figure 3.10 for scene (left) as well as composite level (right). NDVI values based on aggregated data (NDVI$_{agg}$) are opposed to the 10 simulated GAC means (NDVI$_{sim}$) of the same 4×4 km^2 area ('+'), standard deviations within the 10 GAC values are also provided ('♦'). For the limited number of locations we selected, following differences between aggregated and simulated NDVI values were obtained at scene and composite level: mean deviations of NDVI$_{sim}$ from the "true" NDVI (NDVI$_{agg}$) amounted ΔNDVI$_{mean}$=0.001$\pm$0.04 at scene level and ΔNDVI$_{mean}$=$-$0.02$\pm$0.03 at composite level, where NDVI=NDVI$_{agg}$-NDVI$_{sim}$. At composite level, this translates into an average positive relative bias for NDVI$_{sim}$ of 10.6%$\pm$19.1 for the selected locations (not shown). In addition, the uncertainty introduced by the GAC sampling scheme appeared to be somewhat reduced at the multi-date level, given the difference in the mean of the standard deviations at scene (mean σ_{scene}=0.04) and composite level (mean $\sigma_{composite}$=0.02). The GAC sampling scheme has repeatedly been identified in literature as a source of error in AVHRR NDVI data. In general, discrepancies between GAC and aggregated datasets arise from the fact that in GAC sampling, data values unrepresentative of those occurring in the original data are included in the averaging process (Justice et al., 1989). Using simulated AVHRR imagery based on Landsat Multispectral Scanner (MSS) data for various ter-
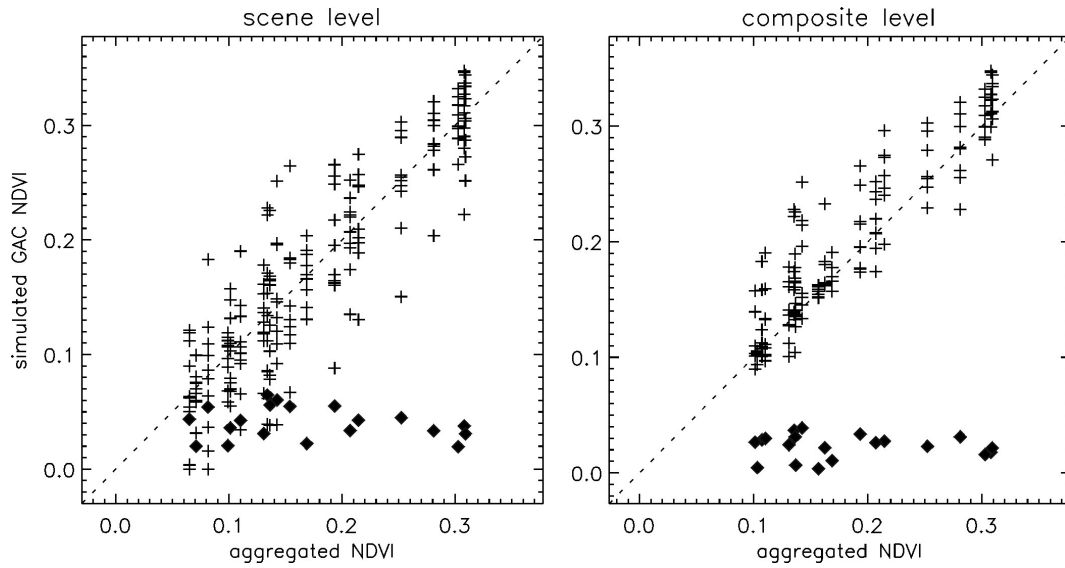
Figure 3.10: *Uncertainty of AVHRR Global Area Coverage (GAC) sampling scheme at scene (left) and composite level (right) for 20 randomly chosen locations within ROI/1. For each aggregated 4 km NDVI, 10 simulated GAC means within the same 4×4 pixel area are plotted ('+'), together with the standard deviation ('♦') within these 10 mean NDVI values.*

rain types Justice et al. (1989) found that for spatially heterogeneous areas, the GAC sampling scheme was less accurate in comparison with other sampling procedures. Belward (1992) demonstrated that undersampling in the GAC data generation leads to increased values of mean local variance in GAC data compared to aggregated data. Our findings for randomly chosen locations in a spatially heterogeneous area (ROI/1) confirm that the GAC sampling scheme potentially leads to biases and additional noise in the data both at scene and composite level, even though we found the uncertainty introduced by the GAC sampling to be reduced through the selection of the maximum NDVI during a compositing interval.

3.4   Concluding remarks

Pixel positions in satellite imagery are affected by the surface topography, however, this effect was so far ignored by most AVHRR processing systems. Given the large area of the Earth's surface covered by elevated topography, this represents a significant drawback for the use of AVHRR data in climate studies over mountainous regions, particularly with regard to the GCOS systematic observation requirements for satellite products (GCOS, 2006). In this study, we have shown that the implementation of orthorectification, i.e. the correction of the terrain displacement in satellite imagery,

has a significant effect on the quality of AVHRR maximum NDVI composites, which are commonly used to analyze vegetation activity at various spatial scales. The analyses were performed for an area in north-western Canada. Differences between orthorectified and non-orthorectified maximum NDVI composites at various spatial resolutions (1 km, 4 km, 5 km, and 8 km) were analyzed for the month of August in 1989, 1990, and 2001 to 2003. Validation was performed using accurately georeferenced MODIS maximum NDVI composites. Large positive and negative differences between orthorectified and non-orthorectified maximum NDVI composites were obtained at single pixel scale in topographically heterogeneous areas, although they were reduced to smaller numbers for coarse resolution data aggregated based on 1 km data. Absolute differences for a topographically more homogeneous and lower laying area were significantly smaller, however, an influence of small scale topography could still be detected. Effects of orthorectification identified at single pixel scale are assumed to be of particular interest for studies dealing with the retrieval of phenological and biophysical information from NDVI time series. However, the temporal uncertainty introduced to NDVI composite by the terrain displacement remains to be addressed in future studies. At regional scale, non-orthorectified composites were found to overestimate mean NDVI at all spatial resolutions. Spatial variability was only significantly affected at 1 km spatial resolution. Regional scale effects are therefore of importance for studies dealing with the contribution of vegetation to biochemical processes when the NDVI is used as input for the generation of fields of biophysical surface parameters such as the LAI. The good geometric accuracy of orthorectified AVHRR composites generated by CCRS CAPS was reflected in high linear correlation coefficients with MODIS reference composites. Local scale topographic features, which are apparent in MODIS composites, were more clearly recognizable in orthorectified AVHRR composites compared to the non-orthorectified data. Analyzing the power spectra of maximum NDVI composites, large differences between orthorectified and non-orthorectified AVHRR data were identified at local scales between 4 km and 10 km. We are, therefore, convinced that orthorectification should be an integral part of AVHRR pre-processing and that orthorectified CAPS output represents an important step towards the generation of high quality satellite climate data records for the Canadian landmass. Finally, differences between $NDVI_O$ and GAC-based datasets from PPF and GIMMS were analyzed for mountainous ROI/1. Positive systematic biases relative to $NDVI_O$ were identified for both GAC-based datasets. The GAC sampling scheme as a source of error in NDVI data in a spatially heterogeneous area such as ROI/1 was discussed both at scene and composite levels. Even though the uncertainty introduced by the GAC sampling scheme was somewhat reduced through the selection of the maximum NDVI during a compositing interval, simulated GAC NDVI data were systematically positively biased at

composite level. Results suggest that AVHRR GAC-based datasets produced with the maximum NDVI composite scheme contain inherent positive NDVI biases and therefore should be used with caution in future vegetation studies in mountain regions. This bias is a consequence of the GAC sampling scheme. It is defined by the degree of local NDVI spatial heterogeneity regardless of surface topography. The correction of this effect using solely GAC data is not possible because continuous imagery is required at higher spatial resolution to obtain unbiased NDVI composites. This conclusion emphasizes the importance of the task on reprocessing of AVHRR 1-km imagery for climate studies as identified by the Committee on Earth Observation Satellites (CEOS) in its response to the GCOS Implementation Plan (CEOS, 2006).

Acknowledgements

References

Bacour, C., F.-M. Breon, and F. Maignan (2006). Normalization of the directional effects in NOAA-AVHRR reflectance measurements for an improved monitoring of vegetation cycles. *Remote Sensing of Environment* **102** (3-4), 402–413.

Belward, A. S. (1992). Spatial attributes of AVHRR imagery for environmental monitoring. *International Journal of Remote Sensing* **13** (2), 193–208.

Beniston, M. (2003). Climatic Change in Mountain Regions: A Review of Possible Impacts. *Climatic Change* **59** (1), 5–31.

Bugmann, H., A. Bjornsen Gurung, F. Ewert, W. Haeberli, A. Guisan, D. Fagre, A. Kääb, and GLOCHAMORE participants (2007). Modeling the Biophysical Impacts of global Change in Mountain Biosphere Reserves. *Mountain Research and Development* **27** (1), 66–77.

CEOS (2006). Satellite observation of the climate system: The Committee on Earth Observation Satellites (CEOS) response to the implementation plan for the Global Observing System for Climate in support of the UNFCCC. Available online at: http://www.ceos.org/images/PDFs/CEOSResponse_1010A.pdf.

Cihlar, J., R. Latifovic, J. Chena, A. Trishchenko, Y. Duc, G. Fedosejev, and B. Guindona (2004). Systematic corrections of AVHRR image composites for temporal studies. *Remote Sensing of Environment* **89** (2), 217–233.

Cihlar, J., D. Manak, and M. D'Iorio (1994). Evaluation of Compositing Algorithms for AVHRR Data Over Land. *IEEE Transactions on Geoscience and Remote Sensing* **32** (2), 427–437.

Cracknell, A. (1997). *The Advanced Very High Resolution Radiometer*. London: Taylor & Francis Ltd.

Delbart, N., T. Le Toan, L. Kergoat, and V. Fedotova (2006). Remote sensing of spring phenology in boreal regions: A free of snow-effect method using NOAA-AVHRR and SPOT-VGT data (1982-2004). *Remote Sensing of Environment* **101** (1), 52–62.

Eidenshink, J. C. and J. L. Faundeen (1994). The 1 km AVHRR global land data set: first stages in implementation. *International Journal of Remote Sensing* **15** (17), 3443–3462.

Fontana, F., C. Rixen, T. Jonas, G. Aberegg, and S. Wunderle (2008). Alpine Grassland Phenology as Seen in AVHRR, VEGETATION, and MODIS NDVI Time Series - a Comparison with In Situ Measurements. *Sensors* **8**, 2833–2853.

Fowler, C., J. Maslanik, T. Haran, T. Scambos, J. Key, and W. Emery (2000, updated 2007). AVHRR Polar Pathfinder Twice-daily 5 km EASE-Grid composites V001/003, August 1989, 1990, 2001, 2002, and 2003. Technical report, Boulder, Colorado USA: National Snow and Ice Data Centre. Digital media.

Fraser, R. H. and Z. Li (2002). Estimating fire-related parameters in boreal forest using SPOT VEGETATION. *Remote Sensing of Environment* **82** (1), 95–110.

GCOS (2006). Systematic Observation Requirements for Satellite-based Products for Climate: Supplemental details to the satellite-based component of the Implementation plan for the Global Observing System for Climate in support of the UNFCC. GCOS-107, WMO/TD-1338.

Global Inventory Modeling and Mapping Studies (GIMMS) (2007). AVHRR 8km Normalized Difference Vegetation Index (NDVI), Bimonthly 1981-2006. Product guide. Available at http://glcf.umiacs.umd.edu/data/gimms/.

Holben, B. N. (1986). Characteristics of maximum-value composite images from temporal AVHRR data. *International Journal of Remote Sensing* **7** (11), 1417–1434.

James, M. and S. Kalluri (1994). The Pathfinder AVHRR land data set: An improved coarse resolution data set for terrestrial monitoring. *International Journal of Remote Sensing* **15**, 3347–3363.

Justice, C. O., B. L. Markham, J. R. G. Townshed, and R. L. Kennard (1989). Spatial degradation of satellite data. *International Journal of Remote Sensing* **10** (9), 1539–1561.

Kapos, V., J. Rhind, M. Edwards, C. Ravilious, and M. F. Price (2000). Developing a Map of the Worlds Mountain Forests. In M. F. Price and N. Butt (eds.), *Forests in a Sustainable Mountain Environment: A state of knowledge report for 2000*, pp. 4–9. CAB International, Wallingford.

Khlopenkov, K. V. and A. P. Trishchenko (2007). SPARC: New cloud, snow, and cloud shadow detection scheme for historical 1-km AVHRR data over Canada. *Journal Of Atmospheric And Oceanic Technology* **24** (3), 322–343.

Khlopenkov, K. V. and A. P. Trishchenko (2008). Implementation and evaluation of concurrent gradient search method for reprojection of MODIS level 1B imagery. *IEEE Transaction on Geoscience and Remote Sensing* **46**, 2016–2027.

Khlopenkov, K. V., A. P. Trishchenko, and Y. Luo (2009). Image matching technique for sub-pixel georeferencing accuracy in Canadian AVHRR Processing System (CAPS). *submitted to IEEE Transaction on Geoscience and Remote Sensing*.

Kidwell, K. (1998). NOAA polar orbiter data user's guide (TIROS-N, NOAA-6, -7, -8, -9,-10, -11, -12, -13 and -14). Technical report, NOAA/National Environmental Satellite, Data, and Information Service (NESDIS).

Latifovic, R., A. Trishchenko, J. Chen, W. Park, K. Khlopenkov, R. Fernandes, D. Pouliot, C. Ungureanu, Y. Luo, S. Wang, A. Davidson, and J. Cihlar (2005). Generating Historical AVHRR 1 km Baseline Satellite Data Records Over Canada Suitab,e for Climate Change Studies. *Canadian Journal of Remote Sensing* **31** (5), 324–346.

Lee, T. Y. and Y. J. Kaufman (1986). Non-Lambertian effects on remote sensing of surface reflectance and vegetation index. *IEEE Transactions on Geoscience and Remote Sensing* **24**, 699–708.

Luo, Y., A. P. Trishchenko, and K. V. Khlopenkov (2008). Developing clear-sky, cloud and cloud shadow mask for producing clear-sky composites at 250-meter spatial

resolution for the seven MODIS land bands over Canada and North America. *Remote Sensing of Environment* **112** (12), 4167–4185.

Moulin, S., L. Kergoat, N. Viovy, and G. Dedieu (1997). Global-Scale Assessment of Vegetation Phenology Using NOAA/AVHRR Satellite Measurements. *Journal of Climate* **10** (6), 1154–1170.

Myneni, R. B., C. D. Keeling, G. Tucker, C. J. Asrar, and R. R. Nemani (1997). Increased plant growth in the northern high latitudes from 1981 to 1991. *Nature* **386**, 698–702.

Pinzon, J., M. E. Brown, and C. J. Tucker (2005). Satellite time series correction of orbital drift artifacts using empirical mode decomposition. In N. Huang (ed.), *Hilbert-Huang Transform: Introduction and Applications*, pp. 167–186.

Pouliot, D., R. Latifovic, and I. Olthof (2009). Trends in vegetation NDVI from 1-km AVHRR data over Canada for the period 1985–2006. *International Journal of Remote Sensing* **30** (1), 149–168.

Rosborough, G. W., D. G. Baldwin, and W. J. Emery (1994). Precise AVHRR image navigation. *IEEE Transactions on Geoscience and Remote Sensing* **32** (3), 644–657.

Running, S. W., C. O. Justice, V. Salomonson, D. Hall, J. Barker, Y. J. Kaufmann, A. Strahler, A. R. Huete, J.-P. Muller, V. Vanderbilt, Z. M. Wan, P. Teillet, and D. Carneggie (1994). Terrestrial remote sensing science and algorithms planned for EOS/MODIS. *International Journal of Remote Sensing* **15** (17), 3587–3620.

Sellers, P. J., S. O. Los, C. J. Tucker, C. O. Justice, D. A. Dazlich, G. J. Collatz, and D. A. Randall (1996). A Revised Land Surface Parametrization (SiB2) for Atmospheric GCMs. Part II. The Generation of Global Fields of Terrestrial Biophysical Parameters from Satellite Data. *Journal of Climate* **9**, 706–737.

Stöckli, R. and P. L. Vidale (2004). European plant phenology and climate as seen in a 20 year AVHRR land-surface parameter dataset. *International Journal of Remote Sensing* **25**, 3303–3330.

Swinnen, E. and F. Veroustraete (2008). Extending the SPOT-VEGETATION NDVI Time Series (1998-2006) Back in Time With NOAA-AVHRR Data (1985-1998) for South Africa. *IEEE Transaction on Geoscience and Remote Sensing* **46**, 558–572.

Townshend, J. R. G., C. Justice, C. Gurney, and J. McManus (1992). The impact of misregistration on change detection. *IEEE Transactions on Geoscience and Remote Sensing* **30** (5), 1054–1060.

Trishchenko, A. P. (2009). Effects of spectral response function on surface reflectance and NDVI measured with moderate resolution satellite sensors: Extension to AVHRR NOAA-17, 18 and METOP-A. *Remote Sensing of Environment* **113** (2), 335–341.

Trishchenko, A. P., J. Cihlar, and Z. Li (2002). Effects of spectral response function on surface reflectance and NDVI measured with moderate resolution satellite sensors. *Remote Sensing of Environment* **81** (1), 1–18.

Trishchenko, A. P., Y. Luo, and K. V. Khlopenkov (2006). A method for downscaling MODIS land channels to 250 m spatial resolution using adaptive regression and normalization. In *Proceedings of SPIE - The International Society for Optical Engineering*, Volume v.6366, pp. 8.

Tucker, C. J., J. E. Pinzon, M. E. Brown, D. A. Slayback, E. W. Pak, R. Mahoney, E. F. Vermote, and N. E. Saleous (2005). An extended AVHRR 8-km NDVI dataset compatible with MODIS and SPOT vegetation NDVI data. *International Journal of Remote Sensing* **26** (20), 4485–4498.

Tucker, C. J. and P. J. Sellers (1986). Satellite remote sensing of primary production. *International Journal of Remote Sensing* **7** (11), 1395–1416.

Udelhoven, T. and M. Stellmes (2007). Changes in land surface conditions on the Iberian Peninsula (1989 to 2004) detected by means of time series analysis from hypertemporal remote sensing data. International Workshop in the Analysis of Multi-temporal Remote Sensing Images, MultiTemp 2007, Leuven.

Voigt, S. (2000). *Advanced methods for operational mapping of Alpine snow cover using medium resolution optical satellite data*. Inauguraldissertation, Universität Bern.

Wolfe, R. E., M. Nishihama, A. J. Fleig, J. A. Kuyper, D. P. Roy, J. C. Storey, and F. S. Patt (2002). Achieving sub-pixel geolocation accuracy in support of MODIS land science. *Remote Sensing of Environment* **83** (1-2), 31–49.

Chapter 4

Alpine grassland phenology as seen in AVHRR, VEGETATION, and MODIS NDVI time series - a comparison with in situ measurements

Fabio M. A. **Fontana**[1,2], Christian **Rixen**[3], Tobias **Jonas**[3], Gabriel **Aberegg**[1], Stefan **Wunderle**[1,2]

[1] *Institute of Geography, University of Bern, Switzerland*

[2] *Oeschger Centre for Climate Change Research, University of Bern, Switzerland*

[3] *WSL, Swiss Federal Institute for Snow and Avalanche Research, Davos Dorf, Switzerland*

Abstract

This study evaluates the ability to track grassland growth phenology in the Swiss Alps with NOAA-16 Advanced Very High Resolution Radiometer (AVHRR) Normalized Difference Vegetation Index (NDVI) time series. Three growth parameters from 15 alpine and subalpine grassland sites were investigated between 2001 and 2005: Melt-Out

(MO), Start Of Growth (SOG), and End Of Growth (EOG). We tried to estimate these phenological dates from yearly NDVI time series by identifying dates, where certain fractions (thresholds) of the maximum annual NDVI amplitude were crossed for the first time. For this purpose, the NDVI time series were smoothed using two commonly used approaches (Fourier adjustment or alternatively Savitzky-Golay filtering). Moreover, AVHRR NDVI time series were compared against data from the newer generation sensors SPOT VEGETATION and TERRA MODIS. All remote sensing NDVI time series were highly correlated with single point ground measurements and therefore accurately represented growth dynamics of alpine grassland. The newer generation sensors VGT and MODIS performed better than AVHRR, however, differences were minor. Thresholds for the determination of MO, SOG, and EOG were similar across sensors and smoothing methods, which demonstrated the robustness of the results. For our purpose, the Fourier adjustment algorithm created better NDVI time series than the Savitzky-Golay filter, since latter appeared to be more sensitive to noisy NDVI time series. Findings show that the application of various thresholds to NDVI time series allows the observation of the temporal progression of vegetation growth at the selected sites with high consistency. Hence, we believe that our study helps to better understand large-scale vegetation growth dynamics above the tree line in the European Alps.

4.1 Introduction

4.1.1 Scientific context

The effects of climate variability on ecosystems have in recent decades become increasingly important within the global climate change discussion (Studer et al., 2007): earlier start of spring and extended autumn conditions are reflected in phenological time series and result in prolonged growing seasons. This has already been demonstrated in phenological ground observations (Menzel, 2000; Roetzer et al., 2000; Defila and Clot, 2001) as well as in remote sensing vegetation index time series (Myneni et al., 1997; Zhou et al., 2001). Ground observations in combination with remote sensing approaches can make important contributions to future climate-phenology studies (Studer et al., 2007). However, ground validation of remote sensing measurements with coarse resolution implies considerable difficulties. Fisher and Mustard (2007) state that the poor relationship between ground- and satellite phenology due to data scale issues is a drawback of satellite phenology, because the chance of a single point ground observation being representative of an entire area at remote sensing scale (typically $\geq$ 1 km in remote sensing phenology studies; White et al., 1997;

Reed et al., 1994) is small. Comparative studies of satellite and ground based phenology were performed in order to assess the interrelationship of both approaches (Chen et al., 2001; Braun and Hense, 2004; Fisher et al., 2006; Fensholt et al., 2006; Fisher and Mustard, 2007). In order to assure the comparability of remote sensing and ground phenological datasets, Fisher and Mustard (2007) suggest that the phenological metric to be investigated should ideally be identifiable from ground and space and it should represent the same phenological event from both perspectives. Additionally, the same authors stress the importance of topography in comparative studies such that small-scale phenological heterogeneity due to highly variable topography may lead to discrepancies between remote sensing and ground observations.

The Normalized Difference Vegetation Index (NDVI) is a commonly used remote sensing vegetation index in climate-phenology studies (Myneni et al., 1997; Zhou et al., 2001; White et al., 1997; Reed et al., 1994; Stöckli and Vidale, 2004). The NDVI is calculated from the reflectances in the red and near infrared (NIR) bands of the electromagnetic spectrum and is a measure of the photosynthetic activity within the area covered by a pixel (Justice et al., 1985; Tucker and Sellers, 1986). NDVI time series, however, suffer from numerous limitations: the calculated NDVI is not only a function of vegetation density and type, but it is also influenced by the atmosphere and illumination as well as observation geometry, which results in noisy NDVI time series (Holben, 1986; Gutman, 1991). In order to extract meaningful information on vegetation dynamics regardless of these distortions, various methods for the elimination of spurious data were developed, such as the Maximum Value Composite (MVC; Holben, 1986), Best Index Slope Extraction (BISE; Viovy et al., 1992), Fourier adjustment (Sellers et al., 1996), Savitzky-Golay filter (Chen et al., 2004), asymmetric Gaussian model functions (Jönsson and Eklundh, 2002), and many more. All methods aim at approaching an upper NDVI envelope, based on the assumption that NDVI values are depressed by any of the above-mentioned effects (Holben, 1986). Smoothing algorithms yet hold the danger of introducing artifacts and suppressing natural variations in the NDVI time series (Fisher and Mustard, 2007).

4.1.2 Study overview

The European Alps are assumed to be particularly sensitive to changes in the climate system (Beniston et al., 1997; Wanner et al., 2000, 1997). Plant species have already been observed to migrate to higher elevations as a consequence of climate change (Grabherr et al., 1994; Walther et al., 2005). Stöckli and Vidale (2004) found a trend towards longer growing season lengths in the European Alps based on the 20-year Pathfinder NDVI dataset (James and Kalluri, 1994). Observed changes in growing

season length are likely to have considerable implications for ecosystem services, agriculture and nature conservation. It is therefore particularly pressing to understand and quantify past and future changes in season length in mountain ranges on large spatial scales, e.g. with remote sensing approaches. Phenological networks in Switzerland (Studer et al., 2005; Defila and Clot, 2001) that could serve as ground validation for remote sensing NDVI time series reach up to 1800 m above sea level. However, for higher elevations the Swiss snow-measuring network IMIS ("Interkantonales Mess- und Informationssystem") can provide data on vegetation growth (Rhyner et al., 2002; Jonas et al., 2008).

The study presented here focuses on the growth phenology of alpine grassland at 15 IMIS sites between 2001 and 2005 from both satellite and ground perspectives. The IMIS network provides an excellent opportunity to link remote sensing and ground phenological measurements in a highly complex environment such as the Swiss Alps, even though frequent cloud cover as well as pronounced topography make the task difficult. Particularly, we investigated the ability of remote sensing NDVI time series to track three IMIS vegetation parameters with special consideration of the 20-year National Oceanic and Atmospheric Administration (NOAA) Advanced Very High Resolution Radiometer (AVHRR) archive of the Remote Sensing Research Group (RSGB), University of Bern. A cross-comparison was subsequently performed with NDVI time series from two newer generation sensors: Système Pour l'Observation de la Terre (SPOT) VEGETATION (VGT; 1 km spatial resolution) and TERRA Moderate Resolution Imaging Spectroradiometer (MODIS; 500 m and 1 km). NDVI time series from all three sensors were smoothed following two different approaches: a Fourier adjustment algorithm modified from Stöckli and Vidale (2004) and the Savitzky-Golay method introduced by Chen et al. (2004). The ability of both algorithms to minimize undesirable noise in the NDVI time series was revised for our purposes.

4.2 Data and methods

4.2.1 Ground dataset

Only a brief overview of the ground dataset is provided here. For detailed information we refer to Jonas et al. (2008). The IMIS network is a meteorological network that has been run by the Swiss Federal Institute for Snow and Avalanche Research (SLF) since 1996 (Rhyner et al., 2002) and that has since then recorded snow and climate variables such as snow depth, air temperature, wind speed, and soil temperature in 30-minute intervals. More than 100 stations were installed throughout the Swiss Alps. Snow
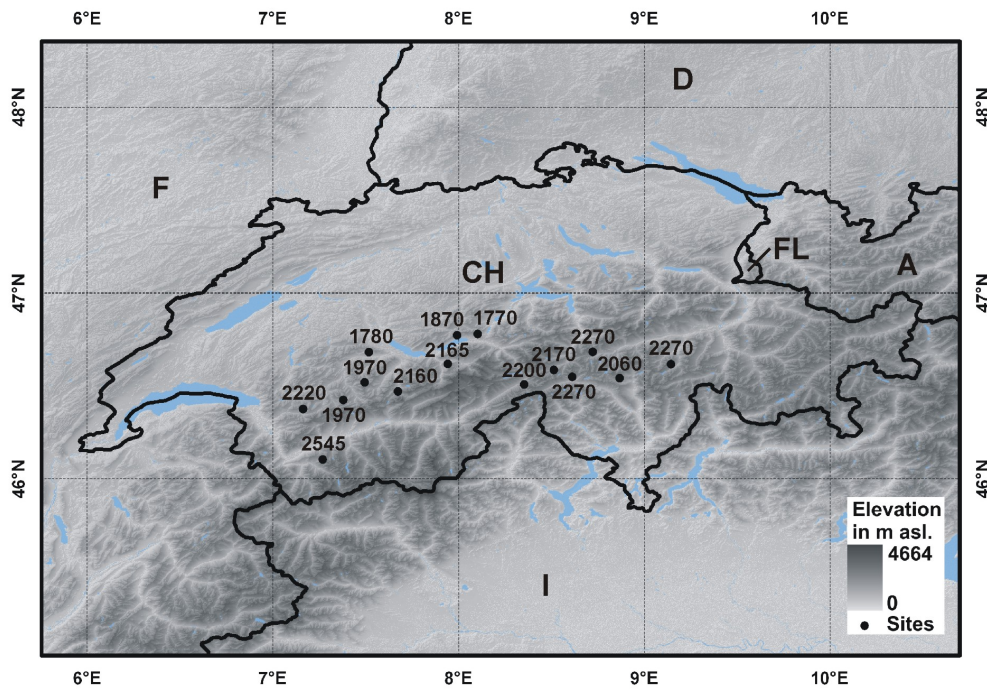
Figure 4.1: *Spatial distribution of the sites (black dots) in Switzerland. All sites represent subalpine and alpine grassland (modified from Jonas et al., 2008). The numbers associated with the black dots indicate site elevations above sea level [m].*

depth is measured from above with an ultrasonic snow depth sensor (mounted on a mast 6 m above ground), which can also track vegetation height during summer. 15 out of 105 stations were identified to best feature undisturbed subalpine and alpine grasslands with a homogeneous vegetation of at least 10 cm height at full growth. The sites are distributed throughout the Swiss Alps and range from 1770 to 2545 m a.s.l. (Figure 4.1). The combination of meteorological and phenological information at the IMIS sites provides an excellent opportunity to study alpine grassland phenology. IMIS dates or indices were computed by fitting the growth signal with a 3-leg linear fit (bold line, Figure 4.2): melt-out date (IMIS$_{MO}$), which can be regarded as the start of season, start of height growth (IMIS$_{SOG}$), and end of growth (IMIS$_{EOG}$), which corresponds to the date where maximum plant height is reached. Leaf unfolding after melt-out did typically not result in any detectable height growth until two to three weeks after melt-out, when the onset of vegetation height growth (IMIS$_{SOG}$) was observed. IMIS$_{SOG}$ was followed by a nearly linear growth until maximum vegetation height was reached (IMIS$_{EOG}$) in early summer (Figure 4.2).

A minimum duration of snow cover at the investigated grassland sites spanning from 1 December to 30 April was identified (Jonas et al., 2008). For the subsequent use
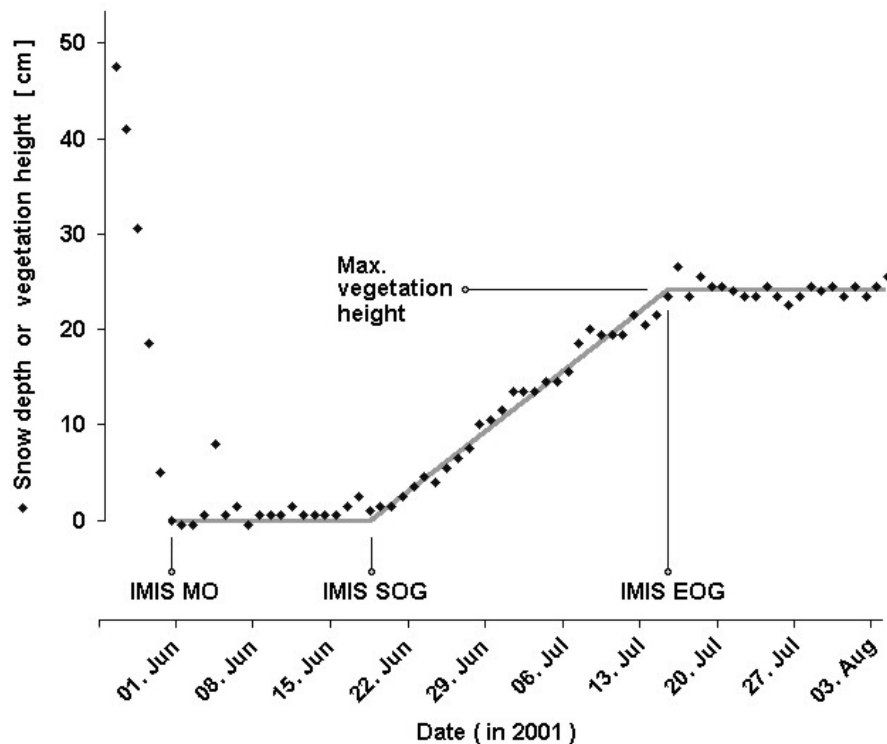
Figure 4.2: *Sample data (black dots) from the ultrasonic sensor at the Tujetsch site (2270 m a.s.l.) in 2001. Melt-out (IMIS$_{MO}$), start of growth (IMIS$_{SOG}$), and end of growth (IMIS$_{EOG}$) are determined from a 3-leg linear fit of the growth signal (adapted and modified from Jonas et al., 2008).*

within the processing of the remote sensing data, we shortened this snow-covered period by 15 days on either side to define a maximum growing season length at the investigated sites.

4.2.2   Remote sensing datasets

NOAA AVHRR

The AVHRR data utilized in this study consist of afternoon passes (Equator Crossing Time $\approx$ 1.30 pm) from the six channel AVHRR/3 instrument on board the polar orbiting NOAA-16 satellite between the 27 February 2001 and 3 October 2005. The nominal instrument spatial resolution at nadir is 1.1 km. Sensor data were calibrated according to the KLM user's guide (Goodrum et al., 2000), using the monthly updated coefficients for channels 1 and 2 from the NOAA National Environmental Satellite Data and Information Service (NESDIS). Prelaunch coefficients for channel 1 and 2 calibration were used before these updates started in 2003. A feature matching algorithm

Table 4.1: *Spectral characteristics [nm] of the red and NIR bands of all involved sensors: AVHRR/3 (Goodrum et al., 2000), VEGETATION (VEGETATION Programme, 1998), and MODIS (Barnes et al., 1998); where red=red part of the electromagnetic spectrum and NIR=near infrared part of the spectrum. Red and NIR bands are involved in the calculation of the NDVI.*

	AVHRR/3	VGT	MODIS
red [nm]	580-680	610-680	620-670
NIR [nm]	725-1000	780-890	841-876

was used to achieve sub-pixel accuracy of the geolocation. Orthorectification, which is important to reduce geometric distortions introduced by the complex alpine relief and the scan geometry, was performed using the GTOPO30 digital terrain model. Cloud detection was done using the Cloud and Surface Parameter Retrieval (CASPR) software by Key (2002). The overall quality of the CASPR algorithm was proved by Di Vittorio and Emery (2002), however, Hauser et al. (2005) who also applied CASPR to NOAA-16 data for a region covering Switzerland observed difficulties arising from sub-pixel clouds. An atmospheric correction in the involved AVHRR channels was not performed. The data were not corrected for NOAA-16 orbital drift, since the effect of solar zenith angle on NDVI is partly compensated for vegetated surfaces (Stöckli and Vidale, 2004) and is assumed to be weak, especially in seasonal and inter-annual terms (Zhou et al., 2001).

NDVI time series were subsequently calculated from AVHRR bands 1 and 2 (Table 4.1). Observations with satellite zenith angles greater than 45° were excluded from further processing in order to avoid large variations in the data due to viewing geometry. Data gaps in early 2001 and late 2005 as pointed out above were dealt with as follows: missing data outside the growing season as outlined in Section 4.2.1 were set to a value of NDVI=-0.05, since the pixel was assumed to be snow covered at that time of the year. Missing data during the snow free period were set to NDVI=0.0. A Maximum Value Composite (AVHRR$_{MVC}$) was subsequently created from the cloud screened daily NDVI data. The MVC technique (Holben, 1986) selects the highest NDVI value within a predefined time interval (i) and is a widely accepted method for the removal of undesirable noise from daily NDVI time series. A value of i=10 days was chosen for the daily AVHRR product.

The drawback of the compositing methodology is the loss of critical temporal information required to accurately track phenological processes. In order to counter this

loss, precise acquisition dates for all selected NDVI values were retained instead of assigning constant time steps (i) to the composite NDVI time series.

SPOT VEGETATION

The freely available SPOT VGT-S RADIOMETRY product for Europe (25°N-75°N, −11°E-62°E) was downloaded from the VGT distribution site (http://free.vgt.vito.be/) for the investigated period (180 scenes totally). The S-10 product represents 10-day composites in 1 km spatial resolution, selecting the pixel with the highest Top of Atmosphere NDVI (VEGETATION Programme, 1998). NDVI time series at the selected alpine grassland sites were extracted from the NDV band. The precise date of acquisition for each pixel was derived from the time grid (TG) band. Cloud as well as quality flags were extracted from the status map (SM). For more detailed information about the VGT-S10 product we refer to the VEGETATION Programme (VEGETATION Programme, 1998).

All cloudy NDVI values that occurred during the snow covered period were set to a value of −0.05. Values from cloudy days during the growing season were linearly interpolated between the previous and subsequent NDVI value. The same procedure was applied to all points where the quality flag in either the red or the near infrared band (Table 4.1) revealed less than ideal quality.

TERRA MODIS

The MODIS tile number h18/v4 (40°N-50°N, 0°E-15.6°E) of the MOD09A1 surface reflectance product with a spatial resolution of 500 m was downloaded from the Land Processes Distributed Active Archive Center (LP DAAC) for the investigated period (225 scenes in total). The MOD09A1 product represents 8-day composites, selecting observations with minimal cloud cover and favorable observation geometry (low solar and satellite zenith angles). MODIS scenes were resampled to UTM 32N (WGS84) prior to further processing.

NDVI time series were calculated from the surface reflectance in MODIS bands 1 and 2 (Table 4.1). The precise acquisition date for each pixel is provided along with the MOD09A1 product in an auxiliary dataset. Cloud state as well as quality flags were extracted from the surface reflectance state flags. The same interpolation procedure for cloudy and not ideal quality NDVI values was performed as described in Section 4.2.2 along with the preprocessing of the VGT-S data.

In order to assess the impact of spatial NDVI product resolution on the comparison with IMIS ground data, a surface reflectance product with 1 km spatial resolution was

generated based on the original 500 m MOD09A1 product using bilinear resampling. Further processing of the 1 km product was performed according to the procedure as described above for the 500 m product. The 1 km NDVI product was finally calculated from the 1 km surface reflectance product, and cloudy as well as not-ideal quality NDVI values were interpolated using the same procedure as for the VGT-S data.

4.2.3   Application of smoothing algorithms

The process of compositing is not sufficient to eliminate all unrealistic variability from NDVI time series (Jönsson and Eklundh, 2002). Two widely used smoothing approaches were therefore modified (below described in detail) and applied to the composite NDVI time series ($NDVI_{comp}$) in order to test for their capability to minimize undesirable noise in the composite NDVI time series at the selected 15 alpine grassland sites: a Fourier adjustment algorithm modified from Stöckli and Vidale (2004) based on Sellers et al. (1996), and an adaptive Savitzky-Golay filter as it was introduced by Chen et al. (2004). Smoothing algorithms were applied to isolated single year time series (i.e. from January to December). Only modifications to the above-mentioned algorithms are dealt with in the following sections.

Fourier Adjustment

Unevenly spaced composite NDVI time series (i.e. precise acquisition dates for all NDVI values) as described here for all three sensors do not meet the requirements of the above mentioned Fourier adjustment algorithm, which assumes constant intervals in time. The algorithm was therefore applied to time series with daily, and hence constant, time steps ($NDVI_{365}$). For that purpose composite NDVI time series were complemented with auxiliary NDVI values ($NDVI_{aux}=-1$) in between the valid points that had been pre-selected within compositing. In order to get a rough approximation of seasonality in the NDVI time series, a second order Fourier series (f) was fitted to $NDVI_{365}$ using non-linear least squares, assigning weights of $W_{valid}=1$ to all valid and $W_{aux}=0$ to all auxiliary points. Data were flagged as anomalous if they were outside the boundary $(f_{comp}-2\sigma) < NDVI_{comp} < (f_{comp}+2\sigma)$, where f_{comp} represents the values of f at the corresponding dates of $NDVI_{comp}$, and σ is the standard deviation of $(f_{comp}-NDVI_{comp})$. Anomalous $NDVI_{comp}$ values were subsequently linearly interpolated between the previous and following valid point. Screened $NDVI_{comp}$ were again transformed into a time series with daily time steps for further processing, assigning $NDVI_{aux}$ to the missing dates.
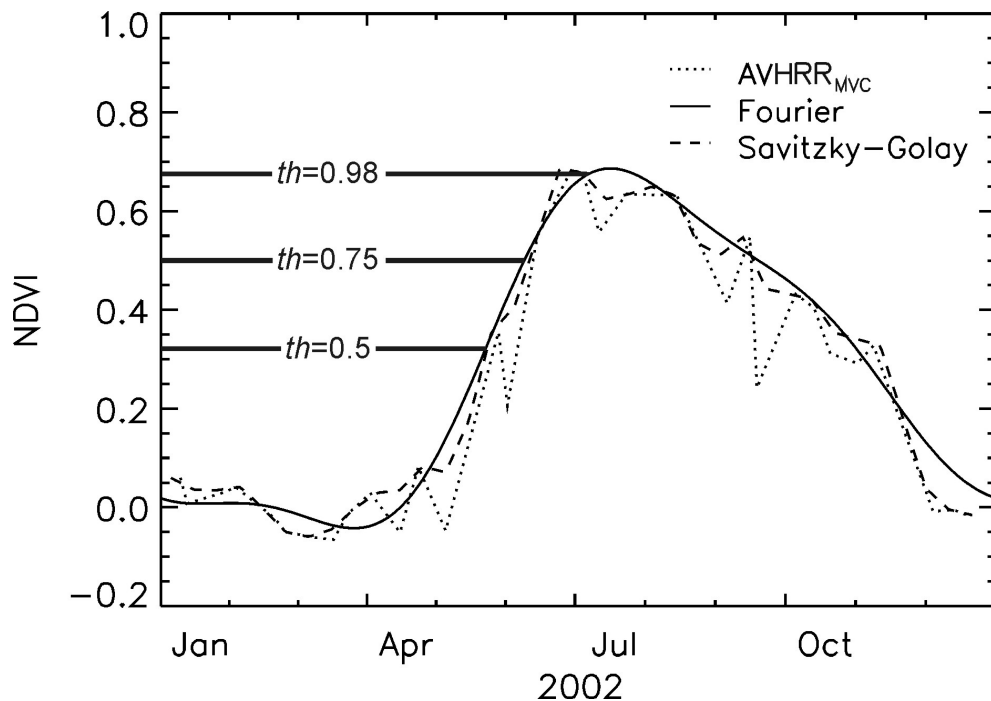
Figure 4.3: *Composite NDVI time series (AVHRR$_{MVC}$; dotted) at the Dötra site in southern Switzerland (2060 m a.s.l) in 2002 and the corresponding Fourier adjusted (thin solid) as well as Savitzky-Golay filtered NDVI products (dashed). NDVI increase in spring is very pronounced after snow melt. The Savitzky-Golay product follows AVHRR$_{MVC}$ more closely compared to the Fourier product. Note the temporal offset between AVHRR$_{MVC}$ (based on precise acquisition dates) and the Savitzky-Golay NDVI product (fix time steps of i=10 days assumed). Thick solid lines mark the thresholds (th) where 50% (th=0.5), 75% (th=0.75), and 98% (th=0.98), respectively, of total annual NDVI amplitude are crossed for the first time.*

In the following we fitted third order Fourier series, since it turned out that the very pronounced NDVI increase in spring and decrease in late fall at the selected sites could not be represented in second order series (not shown). The weighting scheme (Stöckli and Vidale, 2004), which assigns higher weights to uncontaminated measurements than to negative outliers, was only applied during the growing season. Here again, $W_{aux}=0$ were assigned to all NDVI$_{aux}$ of the daily resolution time series. The high temporal resolution (1 day) of the resulting Fourier adjusted NDVI time series can be advantageous when comparing satellite and ground based phenological events. An example of a Fourier adjusted NDVI time series is displayed in Figure 4.3 for the Dötra site, 2060 m a.s.l.

Savitzky-Golay Filter

The Savitzky-Golay filter (Savitzky and Golay, 1964) performs a local polynomial least squares fit within a moving window to assign a smoothed value to each underlying data point. In contrast to simple moving average filters, this filter preserves area, mean position, width, and height of seasonal peaks in NDVI time series (Jönsson and Eklundh, 2004). Like the Fourier adjustment algorithm, the Savitzky-Golay filter requires NDVI data with uniform temporal intervals, however, the use of NDVI time series with daily resolution (taking into account precise acquisition dates as demonstrated for the Fourier algorithm) did not reveal satisfactory results (not shown). Hence, dates corresponding to the MVC time interval center (i/2) were assigned to each NDVI value in order to create an evenly spaced composite NDVI time series (NDVI$_{\mathrm{even}}$) with a temporal resolution of i=10 days. All values outside the boundary $(f-2\sigma) < \mathrm{NDVI}_{\mathrm{even}} < (f+2\sigma)$ were flagged as anomalous, where f is a second order Fourier series that was fitted to NDVI$_{\mathrm{even}}$ and σ the standard deviation of $(f-\mathrm{NDVI}_{\mathrm{even}})$. Anomalous NDVI$_{even}$ values were subsequently linearly interpolated between the previous and following valid point and steps 2 to 7 of the suggested procedure in Chen et al. (2004) were applied to screened NDVI$_{\mathrm{even}}$. Once the NDVI time series was filtered, a curve was fitted to the data points using linear interpolation to obtain daily resolution. An example of a Savitzky-Golay adapted NDVI time series is displayed in Figure 4.3.

4.2.4   Comparison of remote sensing and ground data

The ability of remote sensing NDVI time series to track the IMIS vegetation growth dates IMIS$_{\mathrm{MO}}$, IMIS$_{\mathrm{SOG}}$, and IMIS$_{\mathrm{EOG}}$ was tested using the threshold method. A threshold (*th*) represents a certain fraction of the maximum annual NDVI range (NDVI$_{\mathrm{MAX}}$ − NDVI$_{\mathrm{MIN}}$; Figure 4.3). The date where the threshold is crossed for the first time designates the vegetation growth parameter in the NDVI time series (analogous to IMIS dates: NDVI$_{\mathrm{MO}}$, NDVI$_{\mathrm{SOG}}$, and NDVI$_{\mathrm{EOG}}$). Keeping in mind that the NDVI is a measure of photosynthetic activity and therefore can be related to aboveground biomass (Tucker et al., 1985), we expect leaf unfolding after melt-out as well as grassland height growth to be represented in the NDVI time series as various NDVI levels, i.e. at a certain percentage of the maximum annual greenness of each pixel. The threshold method, however, strongly depends on single data points (NDVI$_{\mathrm{MAX}}$ and NDVI$_{\mathrm{MIN}}$) and is hence sensitive to errors in the timing and magnitude of both NDVI bounding values (Fisher et al., 2006).

The relationship between remote sensing and ground datasets was on the one hand quantified by calculating the linear correlation coefficient (r) of remote sensing and

ground growth phenological dates, and on the other hand by the determination of the mean temporal offset in days ($\overline{OD}$) between the two datasets, with OD representing the temporal offsets in days between remote sensing and ground datasets for each phenological date, site and year. Several thresholds were tested for each pixel and phenological date in order to identify which thresholds yielded lowest $\overline{OD}$. The mean offset in days $\overline{OD}$ adopted negative values where the growth parameter was estimated too early in the year by the remote sensing NDVI dataset, i.e. where *th* was chosen too low. Analogously, $\overline{OD}$ adopted positive values where *th* was chosen too high. Figure 4.4 addresses this issue, showing an example of a relationship between satellite and ground data where *th* was chosen too low (left), nearly optimal (middle) and too high (right). In the first case the majority of the points are below the 1:1 line, gradually shifting upwards with increasing thresholds (middle and right). OD for each point is given by its vertical distance from the 1:1 line. The scatter as seen in the subplots of Figure 4.4 was therefore described as the OD standard deviation (σ in Figure 4.4 and Table 4.2) in addition to the linear correlation coefficient r. These analyses were carried out for eight NDVI datasets from all 4 products (AVHRR, VGT, MODIS 500 m, and MODIS 1 km), each smoothed with both filter methods (i.e. Fourier adjustment and Savitzky-Golay filter; Table 4.2). Differences in correlation coefficients were tested performing the Fisher r-to-z transformation, standard deviations of the offset in days by means of the F-test. In the following, p-values of $p < 0.01$ were termed as highly statistically significant and $p < 0.05$ as statistically significant.
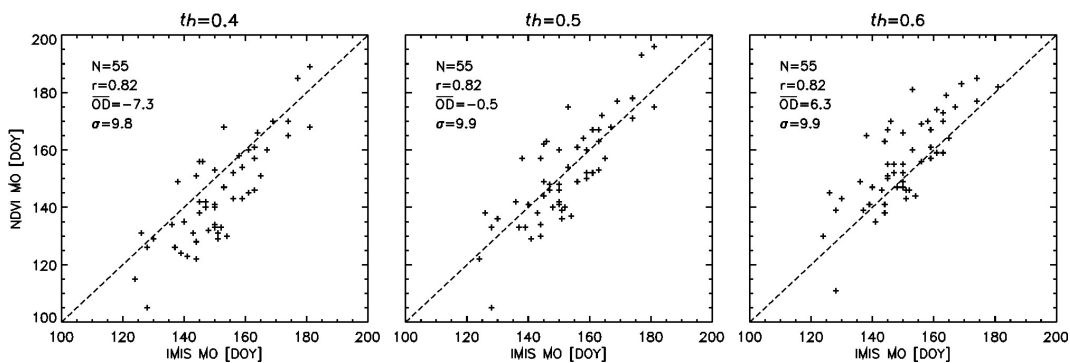

Figure 4.4: *Relationship of remote sensing NDVI time series and IMIS ground data depending on the chosen threshold (*th*), exemplary shown for the detection of melt-out (MO) by means of the Fourier adjusted MODIS (500 m) NDVI dataset. Where *th* is chosen too low (*th=0.4; left) the majority of the points lies below the 1:1 line (mean offset of days ($\overline{OD}$) negative). OD for each point is given by the vertical distance between each point and the 1:1 line. With *th=0.5 (middle) points closely follow the 1:1 line ($\overline{OD} \approx 0$), whereas the point cloud shifts over the 1:1 line ($\overline{OD}$ positive) with increasing thresholds (*th=0.6; right). r=linear correlation coefficient of satellite and ground dataset, σ=standard deviation of OD.*

4.3 Results

Out of the three thresholds that were tested for each phenological event, smoothing algorithm, and sensor, shaded thresholds in Table 4.2 generally represent the lowest mean offset in days ($\overline{OD}$). For the same phenological date, the best thresholds (i.e. yielding min. $\overline{OD}$) were very similar across all sensors and smoothing methods. On the other hand, the optimum thresholds for different phenological dates showed clear differences. All best (shaded) threshold values ranged between 0.5 and 0.6 for MO, between 0.7 and 0.75 for SOG and between 0.95 and 0.98 for EOG. Hence, an effect of spatial NDVI product resolution on the determination of the thresholds was not found for the MODIS 500 m and 1 km products, i.e. best thresholds (Table 4.2 [d]) remained unchanged with reduced spatial resolution.

Correlations were highly significant across all datasets and smoothing algorithms, with linear correlation coefficients adopting values between r=0.51 and r=0.82 (Table 4.2). Overall best correlations were obtained by the Fourier adjusted MODIS 500 m NDVI dataset. Overall lowest correlations were obtained for EOG extraction by means of the Savitzky-Golay filtered NDVI time series. In general, large standard deviations of OD were observed (cp. Table 4.2), with highest standard deviations obtained for the AVHRR product and lowest standard deviations obtained for the MODIS 500 m product (Figure 4.4).

4.3.1 Comparison of AVHRR NDVI time series and IMIS phenological dates

Differences in smoothing algorithm performance were apparent (significance levels indicated in Table 4.2): the Fourier adjusted NDVI data exhibited overall higher correlations with the IMIS phenological dates than the Savitzky-Golay filtered data, however, this difference was not statistically significant. Additionally, OD standard deviation was generally found to be higher for the Savitzky-Golay filtered dataset compared to the Fourier adjusted data, with the difference in OD standard deviation for the detection of EOG being highly significant. No obvious pattern was found in terms of which phenological event showed highest correlations within one respective dataset: within the Fourier adjusted AVHRR NDVI time series, EOG displayed highest correlations (MO lowest), whereas within the Savitzky-Golay filtered data, SOG exhibited highest correlations (EOG lowest).

4.3.2 Comparison to VGT and MODIS products

Differences in smoothing algorithm performance were not as pronounced for the investigated newer generation sensors compared to AVHRR, even though Fourier adjusted NDVI time series generally exhibited slightly higher correlations compared to the Savitzky-Golay filtered time series. OD standard deviations were highly significantly different for EOG detection using the MODIS 500 m product (significance levels indicated in Table 4.2).

All VGT as well as MODIS NDVI products exhibited higher correlations compared to AVHRR, but the difference was not statistically significant in all investigated cases (Table 4.2 [b-d]): Differences within the Fourier adjusted datasets were e.g. significant for the detection of MO, but not significant for EOG detection. Correlations of IMIS phenological dates and 1 km MODIS NDVI time series were not significantly lower compared to the MODIS 500 m product and were comparable to the correlations as obtained for the VGT NDVI product (also 1 km).

OD standard deviations of all newer generation products were lower compared to AVHRR. Differences in OD standard deviations were e.g. statistically significant for EOG detection by means of the VGT and MODIS 1 km Savitzky-Golay filtered datasets compared to AVHRR. An minor effect of spatial resolution was detected in terms of OD standard deviation, which was found to increase with lowered spatial resolution. This effect was more pronounced for the Fourier adjusted NDVI data compared to the Savitzky-Golay filtered data. OD standard deviations of the Fourier adjusted 1 km MODIS product appeared to be of the same order of magnitude as the standard deviations obtained with the 1 km VGT datasets, but lower compared to the AVHRR NDVI data.

Table 4.2 *(facing page)*: *Relationship between phenological growth dates of alpine grassland from four remote sensing NDVI time series ([a-d]; each smoothed with two smoothing algorithms) and IMIS sensor ground data, where MO=melt-out, SOG=start of growth, EOG=end of growth,* th=*applied threshold, r=linear correlation coefficient of satellite and ground dataset, and $\overline{OD}$=mean temporal offset in days between satellite and ground dataset $\pm$ one standard deviation (σ). Several thresholds were tested for each parameter, NDVI product, and sensor. Shaded thresholds indicate lowest $\overline{OD}$ with regard to the other thresholds. All correlations were significant with p < 0.001 (two-tailed). Significant differences between equivalent values of r and σ, respectively, (for shaded thresholds only) are indicated for i) the comparison of AVHRR with the newer generation sensors (horizontal, **:1%-level, *:5%-level, one-tailed) and ii) the comparison between smoothing algorithms (vertical, $^{\bullet\bullet}$:1%-level, two-tailed). Comparisons within the MODIS products (500 m and 1 km) did not reveal significant differences.*

Fourier

N=55

[a] AVHRR (1 km)

	th	r	$\overline{OD}$
MO	0.5	0.61	−7.1±13.3
	0.6	0.61	0.3±13.4
	0.7	0.60	7.9±13.4
SOG	0.7	0.63	−6.2±13.4
	0.75	0.64	−2.2±13.3
	0.8	0.64	2.2±13.2
EOG	0.95	0.67	−6.4±12.8
	0.98	0.68	0.7±12.4 ••
	1.0	0.66	12.7±12.6

[b] VEGETATION (1 km)

	th	r	$\overline{OD}$
MO	0.5	0.78	−3.6±11.0
	0.6	0.78 *	3.5±10.9
	0.7	0.79	10.7±10.8
SOG	0.7	0.77	−3.4±11.4
	0.75	0.77	0.5±11.3
	0.8	0.77	4.7±11.3
EOG	0.95	0.72	−3.4±12.9
	0.98	0.69	3.2±13.2
	1.0	0.67	14.4±13.5

[c] MODIS (500 m)

	th	r	$\overline{OD}$
MO	0.4	0.82	−7.3±9.8
	0.5	0.82 *	−0.5±9.9 *
	0.6	0.82	6.3±9.9
SOG	0.6	0.79	−7.8±10.8
	0.7	0.79	−0.6±10.7
	0.75	0.79	3.3±10.8
EOG	0.9	0.77	−8.7±11.7
	0.95	0.76	−1.5±12.4 ••
	0.98	0.74	4.7±12.9

[d] MODIS (1 km)

	th	r	$\overline{OD}$
MO	0.4	0.8	−6.8±11.4
	0.5	0.8 *	0.2±11.7
	0.6	0.81	7.1±11.3
SOG	0.6	0.75	−7.0±12.6
	0.7	0.75	0.4±12.4
	0.75	0.75	4.3±12.3
EOG	0.9	0.75	−8.0±12.4
	0.95	0.74	−1.0±12.4
	0.98	0.74	5.4±12.4

Savitzky-Golay

N=55

[a] AVHRR (1 km)

	th	r	$\overline{OD}$
MO	0.5	0.55	−5.3±14.4
	0.6	0.53	1.5±15.0
	0.7	0.52	7.8±15.5
SOG	0.7	0.59	−6.4±14.7
	0.75	0.57	−1.6±14.7
	0.8	0.47	3.0±17.3
EOG	0.9	0.50	−13.0±18.5
	0.95	0.51	−3.7±20.1
	0.98	0.60	5.2±18.2

[b] VEGETATION (1 km)

	th	r	$\overline{OD}$
MO	0.5	0.76	−7.9±11.2
	0.6	0.76 *	−2.4±11.2 *
	0.7	0.76	3.6±11.3
SOG	0.75	0.76	−7.1±11.4
	0.8	0.76 *	−3.5±11.5
	0.9	0.72	6.9±12.4
EOG	0.95	0.71	−11.4±13.1
	0.98	0.64	−2.5±15.2 *
	1.0	0.49	8.5±19.5

[c] MODIS (500 m)

	th	r	$\overline{OD}$
MO	0.4	0.79	−4.8±11.9
	0.5	0.81 **	0.3±11.3 *
	0.6	0.80	4.6±11.5
SOG	0.7	0.79	−3.8±11.4
	0.75	0.79 *	−0.5±12.4
	0.8	0.78	3.4±13.2
EOG	0.95	0.63	−4.8±17.4
	0.98	0.63	0.7±17.7
	1.0	0.57	11.8±19.8

[d] MODIS (1 km)

	th	r	$\overline{OD}$
MO	0.4	0.81	−4.7±11.6
	0.5	0.81 **	0.6±11.4
	0.6	0.8	5.6±11.8
SOG	0.7	0.75	−3.4±13.0
	0.75	0.73	−0.1±13.6
	0.8	0.74	3.1±13.8
EOG	0.95	0.74	−9.1±13.6
	0.98	0.72 *	−1.7±14.5 *
	1.0	0.63	8.9±18.0

4.4 Discussion

The good agreement between the spectral remote sensing measurements and the single point vegetation height measurements in highly complex terrain was remarkable, especially in consideration of the large differences in measurement scales. Robustness of the results was reflected in consistent thresholds among all NDVI products and phenological events and is encouraging with regard to further phenological studies within complex alpine environments.

Numerous previous studies have investigated the relationship between remote sensing and ground measured vegetation indices as well as biophysical parameters in a wide range of grassland ecosystems (Fensholt et al., 2006; Tucker et al., 1985; Kennedy, 1989; Kawamura et al., 2003; Wilson and Meyers, 2007), including such in the European Alps (Vescovo and Gianelle, 2006, 2007). By contrast to these studies, our study focused on the resolution of annual growth dynamics of alpine grassland. We believe that relating threshold derived phenological dates from remote sensing NDVI time series to ground phenological data from the IMIS network was an important step towards a better understanding of broad scale vegetation growth dynamics above the tree line in the European Alps.

4.4.1 Determination of thresholds

Optimal thresholds were only investigated with a precision of 0.1 (MO), 0.05 (SOG), and 0.02/0.03 (EOG). A larger dataset would be needed in order to determine precise thresholds for each NDVI dataset and parameter. However, the good agreement between both satellite and ground datasets still enables us to identify following approximate thresholds to be suitable to determine grassland growth phenology with NDVI time series at the selected 15 IMIS sites:

- Melt-out: $th{\approx}0.6$

- Start of growth: $th{\approx}0.75$

- End of growth: $th{\approx}0.98$

Even though year-to-year melt-out variability at the selected sites is very high (below described in detail), melt-out dates from ground and remote sensing datasets showed a good agreement. Independent of sensor and smoothing algorithm, thresholds of approx. $th{=}0.6$ seemed to be appropriate to track MO, which can be regarded as the start of season. This threshold for the determination of the start of season is slightly

higher compared to the threshold as it was applied e.g. in Stöckli and Vidale (2004) to a NDVI dataset with 0.1° spatial resolution. Stöckli and Vidale (2004) applied a threshold of *th*=0.4 to the entire Alps subdomain in order to derive start of season dates for a period of 20 years. However, lower spatial resolution of the latter NDVI product renders a comparison of both thresholds difficult, since first of all, the variability of the occurrence of phenological events within a pixel will increase with lower spatial resolution, and second, an area of 0.1°×0.1° within the European Alps will most likely include land cover classes other than grassland. It will therefore exhibit different annual NDVI dynamics compared to the higher resolution NDVI datasets as used in this study. This issue emphasizes the necessity of adapting thresholds to specific land cover classes. Based on these considerations, we suggest that whether or not the presented thresholds are applicable to coarser resolution NDVI products critically depends on the homogeneity of land cover and terrain within the investigated area.

SOG dates, which at the ground usually were observed two to three weeks after MO, coincided with the date where approximately 75% of the total annual NDVI amplitude were crossed, corresponding to *th*=0.75. The differences in the threshold magnitude between MO and SOG reflect the increased pixel integrated greenness due to leaf unfolding and build up of leaf biomass after snow melt. Then again, EOG dates were generally identified in remote sensing data shortly before NDVI time series reached saturation ($NDVI_{MAX}$). The fact that $IMIS_{EOG}$ nearly coincided with $NDVI_{MAX}$ is a highly interesting finding, suggesting that maximum photosynthetic activity of alpine grassland is achieved at the end of height growth, i.e. when vegetation has reached its maximum height.

Since the decrease of spatial resolution from 500 m to 1 km did not have an effect on the determination of the thresholds, we suggest that thresholds for alpine grassland to a major extent depend on the spectral characteristics of the sensor: according to Table 4.1 red bands of the considered sensors all encompass different parts of the spectrum in the red domain, hence being variably sensitive to changes in chlorophyll concentration within the grassland pixel (Gitelson and Kaufman, 1998). Positions of the channels in the visible domain of the electromagnetic spectrum can thereby influence the magnitude of the NDVI (Teillet et al., 1997) and the shape of the NDVI curve. Thus, differences in spectral band widths and locations (Table 4.1) lead to variable NDVI dynamic ranges ($NDVI_{MAX}-NDVI_{MIN}$) among the sensors (Fensholt et al., 2006) as well as to different timings of $NDVI_{MAX}$, i.e. NDVI saturation. The determination of the thresholds is thereby influenced. The time of occurrence of $NDVI_{MAX}$ is particularly important for the extraction of EOG from remote sensing NDVI time series, since the thresholds were found to be close to *th*=1.0, i.e. close to $NDVI_{MAX}$ itself. The magnitude of the NDVI as well as the shape of the NDVI curve also depend on the reduction

of the atmospheric influence in both channels, since NDVI values are depressed by atmospheric influence (Gutman, 1991). This issue is discussed in more detail below.

The shape of the NDVI curve is to a certain extent also influenced by the nonuniform distribution of bidirectional reflectance (BRD), which results in surface reflectance – and hence NDVI – variations depending on the observation geometry (relative positions sun–target–sensor; Cihlar et al., 1997; Los et al., 2005). However, it was also shown that BRD effects are significantly reduced through the calculation of vegetation indices such as the NDVI from single channel data (Holben, 1986; Lee and Kaufman, 1986) and minimized through the process of compositing (Holben, 1986).

4.4.2 Smoothing algorithm performance

Even though the differences in r and σ between the two smoothing approaches were mostly statistically insignificant, results as summarized in Table 4.2 suggest that for our purposes the Fourier algorithm was more efficient in eliminating undesirable noise from the NDVI time series. Since Savitzky-Golay NDVI products closely follow the composite NDVI times series (Figure 4.3), they are more sensitive to short term NDVI variations and therefore more susceptible to noisy data. This is most clearly reflected in EOG detection by means of the Savitzky-Golay filtered NDVI time series, where linear correlation coefficients were lowest and OD standard deviation values highest among all investigated cases: noisy time series during the growing season led to multiple local NDVI maxima. Since thresholds for the determination of EOG were found to be close to th=1.0 (i.e. $NDVI_{MAX}$), the chance that EOG was attributed to the wrong NDVI peak was high. This issue underlines a drawback of the threshold methodology (Section 4.2.4), i.e. that the determination of phenological dates from NDVI time series using a fraction of the maximum annual NDVI amplitude may be influenced by errors in the magnitude and timing of both bounding values. Third order Fourier series on the other hand can only track changes in vegetation with a periodicity of 4 months and are therefore less susceptible to noisy composite time series. Residual noise in the Fourier adjusted NDVI time series could be avoided by choosing lower order Fourier series, however, we argue that third order Fourier series represent a good trade-off between noise removal on the one hand and representation of natural NDVI short term variations on the other hand.

As mentioned in Section 4.2.2 the process of compositing comes along with a loss of temporal information. The application of the Fourier algorithm to NDVI time series with daily time steps (considering precise acquisition dates) certainly helped to over-come this issue to a certain extent. By contrast, the temporal uncertainty introduced to the Savitzky-Golay filtered datasets by assigning fixed time intervals of i=10 (Fig-

ure 4.3) likely added to the lower performance of the Savitzky-Golay filtered NDVI datasets.

4.4.3 AVHRR vs. newer generation sensors

The fact that all three sensors turned out to be capable of tracking alpine grassland dynamics at the selected sites is encouraging with regard to the analysis of the 20-year AVHRR archive. However, results as summarized in Table 4.2 revealed drawbacks of AVHRR compared to the newer generation sensors (though not statistically significant in all cases). Differences in spectral sensor characteristics likely added to this effect (Table 4.1). This is particulary important regarding the NIR band, where clear differences between AVHRR and the newer generation sensors are apparent. The AVHRR NIR band is superimposed on strong water vapor absorption bands between 900-980 nm, whereas VGT and MODIS NIR bands do not cover these absorption bands and are hence less affected by variations in atmospheric water vapor content (Kawamura et al., 2005; Justice et al., 1991). This effect is enhanced by the fact that both VGT and MODIS data include atmospheric correction, whereas AVHRR data were not corrected for these effects. Even though VGT and MODIS data both include atmospheric correction, Fensholt et al. (2006) found discrepancies between VGT and MODIS in the reflectance values of the NIR bands due to differences in atmospheric correction schemes.

Noisy composite NDVI time series were in some cases still observed for all three sensors even after quality and cloud screening, even though unrealistic NDVI values ideally are discarded through the process of compositing. In general, remaining noise in the NDVI time series could be attributed to – for remote sensing applications – hindering weather conditions in terms of extended cloudy periods during the growing season. While in the Alps less cloud cover is observed in winter (December through February) compared to the foreland, the opposite applies to the summer months (June through August), when frequent cloud cover is observed due to orographically induced convection (Kästner and Kriebel, 2001; Winkler et al., 2006). In the case of AVHRR, insufficient cloud masking by the CASPR algorithm as outlined above likely added to the observed noise in the time series and thereby contributed to the lower performance of AVHRR.

4.4.4 Explanation of OD standard deviation

Complex alpine and subalpine topography leads to high snow cover variability in space and time due to terrain effects on various climatic variables such as wind, precipitation,

and snow fall (Liston and Sturm, 1998; Keller et al., 2005). The resulting "patchy mosaic" (Liston, 1999) of vegetation and snow cover during the period of snow melt results in high year to year NDVI variability within the area around each IMIS site, regardless of the snow and vegetation conditions at the site itself. This random effect adds to the between-year variability of observed phenological dates such that a pixel in one year may exhibit a vegetation signal before, and in another year after it is observed at the IMIS site. Land cover is another crucial factor, which has to be taken into account in this respect due to the limited spatial extent of the investigated grassland areas of sometimes only a few square kilometers: depending on varying pixel size due to observation geometry contaminating land cover classes other than grassland might have influenced the shape of the annual NDVI curve and hence the extraction of phenological dates in some cases.

Even though the locations of the IMIS sites were chosen to be representative of the direct site environment (Rhyner et al., 2002), systematic offsets between remote sensing and ground data may be expected according to the location of the IMIS site within its surrounding topography: phenological dates from elevated sites (IMIS site above median elevation of pixel) will presumably be estimated too early by the NDVI, since the phenology at such IMIS sites lags behind the average phenology of the (lower) surroundings. The opposite effect is expected for valley sites (IMIS site below median elevation of pixel). Similar small-scale effects of topography have already been stressed by Fisher et al. (2006). Given the limited number of 15 sites, here this issue cannot be addressed in more detail. However, another dataset consisting of five years of melt-out dates from another 69 sites throughout the Swiss Alps will be available for that purpose in the near future.

Interestingly, OD standard deviations of the 1 km MODIS Fourier and VGT datasets were of comparable magnitude, leading to the assumption that OD standard deviation also depends on spatial sensor resolution. That again is in good agreement with the above mentioned issue of small-scale vegetation and snow cover variability (Liston, 1999) as well as the influences of multiple land cover classes in the surroundings of the site: both effects obviously become less pronounced with enhanced spatial resolution.

4.5 Conclusion and outlook

The capability of NOAA AVHRR NDVI time series to track alpine grassland phenology was investigated with regard to the analysis of our 20 year AVHRR archive. Three grassland growth phenological dates (melt-out, start of growth, and end of growth) were extracted from NDVI time series and compared to equivalent measurements from

the IMIS network at 15 sites in the Swiss Alps. The same investigations were performed for three additional NDVI products from newer generation sensors VGT and MODIS.

The good agreement between single point vegetation height and coarse scale remote sensing measurements was remarkable. Even though correlations were lower for AVHRR compared to the newer generation sensors, results for AVHRR were encouraging with regard to long-term vegetation dynamics analysis in the Swiss Alps. The ability of the tested Fourier adjustment algorithm to minimize undesirable noise from the NDVI time series at the selected sites must be rated higher compared to the Savitzky-Golay product, since the Fourier product is less susceptible to noisy composite time series. Similar thresholds for the determination of grassland phenological dates across sensors and smoothed NDVI products demonstrated the high robustness of the results. Findings for all three sensors show that the application of various thresholds to NDVI time series allows the observation of the temporal progression of vegetation growth at the selected sites with high consistency. Minor threshold differences among the investigated NDVI products are assumed to result from variable spectral sensor characteristics in the red bands, which govern chlorophyll sensitivity, and thereby influence the annual NDVI range.

Discrepancies between remote sensing and ground datasets are assumed to result from small-scale phenological variability due to complex topography as well as from land cover classes other than grassland in the surroundings of the sites. These assumptions are supported by the fact that discrepancies are smaller for the 500 m spatial resolution MODIS product compared to the equivalent 1 km product. Overall, ground based data from the IMIS station network provided a valuable tool to better understand and interpret remote sensing NDVI data.

Investigations will be extended to a larger number of sites and years as soon as the particular data will be available. In order to assess the reasons for the discrepancies between remote sensing and ground data, the incorporation of topographic information in data analysis will be necessary. The inclusion of additional ground verification sites in combination with topographic information will significantly improve our understanding of the relationship between remote sensing and ground phenological measurements in a complex environment such as the Swiss Alps. Additionally, AVHRR data from other NOAA satellites will be included in order to assess the transferability of the results to other satellites of the NOAA series. This will finally enable us to investigate changes in alpine vegetation dynamics on a larger spatial scale for the past 20 years with high spatial and temporal resolution based on the RSGB AVHRR archive. Knowledge about these changes will significantly enhance our understanding of the potential future impact of climate warming on sensitive alpine ecosystems.

Acknowledgements

References

Barnes, W. L., T. S. Pagano, and V. V. Salomonson (1998). Prelaunch characteristics of the Moderate Resolution Imaging Spectroradiometer (MODIS) on EOS-AM1. *IEEE Transactions on Geoscience and Remote Sensing* **36**, 1088–1100.

Beniston, M., H. F. Diaz, and R. S. Bradley (1997). Climatic Change at High Elevation Sites: An Overview. *Climatic Change* **36**, 233–251.

Braun, P. and A. Hense (2004). Combining ground-based and satellite data for calibrating vegetation indices. In *Proceedings SPOT 4/5 Vegetation unser's Conference*, Antwerp, pp. 137–141.

Chen, J., P. Jönsson, M. Tamura, Z. Gu, B. Matsushita, and L. Eklundh (2004). A simple method for reconstructing a high-quality NDVI time-series data set based on the Savitzky-Golay filter. *Remote Sensing of Environment* **91**, 332–344.

Chen, X., C. Xu, and Z. Tan (2001). An analysis of relationships among plant community phenology and seasonal metrics of Normalized Difference Vegetation Index in the northern part of the monsoon region of China. *International Journal of Biometeorology* **45**, 170–177.

Cihlar, J., H. Ly, Z. Li, J. Chen, H. Pokrant, and F. Huang (1997). Multitemporal, multichannel AVHRR data sets for land biosphere studies - artifacts and corrections. *Remote Sensing of Environment* **60**, 35–57.

Defila, C. and B. Clot (2001). Phytophenological trends in Switzerland. *International Journal of Biometeorology* **45**, 203–207.

Di Vittorio, A. V. and W. J. Emery (2002). An automated, dynamic threshold cloud-masking algorithm for daytime AVHRR images over land. *IEEE Transactions on Geoscience and Remote Sensing* **40**, 1682–1694.

Fensholt, R., I. Sandholt, and S. Stisen (2006). Evaluating MODIS, MERIS, and VEGE-TATION Vegetation Indices Using In Situ Measurements in a Semiarid Environment. *IEEE Transactions on Geoscience and Remote Sensing* **44**, 1774–1786.

Fisher, J. I. and J. F. Mustard (2007). Cross-scalar satellite phenology from ground, Landsat, and MODIS data. *Remote Sensing of Environment* **109**, 261–273.

Fisher, J. I., J. F. Mustard, and M. A. Vadeboncoeur (2006). Green leaf phenology at Landsat resolution: Scaling from the field to the satellite. *Remote Sensing of Environment* **100**, 265–279.

Gitelson, A. A. and Y. J. Kaufman (1998). MODIS NDVI Optimization To Fit the AVHRR Data Series–Spectral Considerations. *Remote Sensing of Environment* **66**, 343–350.

Goodrum, G., K. B. Kidwell, and W. Winston (2000). NOAA KLM user's guide. Technical report, National Environmental Satellite, Data, and Information Services (NESDIS).

Grabherr, G., M. Gottfried, and H. Pauli (1994). Climate effects on mountain plants. *Nature* **369**, 448–448.

Gutman, G. G. (1991). Vegetation Indices from AVHRR: An Update and Future Prospects. *Remote Sensing of Environment* **35**, 121–136.

Hauser, A., D. Oesch, N. Foppa, and S. Wunderle (2005). NOAA AVHRR derived Aerosol Optical Depth over land. *Journal of Geophysical Research* **110**, 8204–+.

Holben, B. N. (1986). Characteristics of maximum-value composite images from temporal AVHRR data. *International Journal of Remote Sensing* **7**, 1417–1434.

James, M. and S. Kalluri (1994). The Pathfinder AVHRR land data set: An improved coarse resolution data set for terrestrial monitoring. *International Journal of Remote Sensing* **15**, 3347–3363.

Jonas, T., C. Rixen, M. Sturm, and V. Stöckli (2008). How alpine plant growth is linked to snow cover and climate variability. *Journal of Geophysical Research* **113** (G03013), doi:10.1029/2007JG000680.

Jönsson, P. and L. Eklundh (2002). Seasonality extraction by function fitting to time-series of satellite sensor data. *IEEE Transactions on Geoscience and Remote Sensing* **40**, 1824–1832.

Jönsson, P. and L. Eklundh (2004). TIMESAT–a program for analyzing time-series of satellite sensor data. *Computers and Geosciences* **30**, 833–845.

Justice, C., T. Eck, D. Tanré, and B. Holben (1991). The effect of water vapor on the normalized difference vegetation index derived for the Sahelian region from NOAA AVHRR data. *International Journal of Remote Sensing* **12**, 1165–1187.

Justice, C. O., J. R. G. Townshend, B. N. Holben, and C. J. Tucker (1985). Analysis of the phenology of global vegetation using meteorological satellite data. *International Journal of Remote Sensing* **6**, 1271–1318.

Kästner, M. and K. T. Kriebel (2001). Alpine cloud climatology using long-term NOAA AVHRR satellite data. *Theoretical and Applied Climatology* **68**, 175–195.

Kawamura, K., T. Akiyama, O. Watanabe, H. Hasegawa, F. Zhang, H. Yokota, and S. Wang (2003). Estimation of aboveground biomass in Xilingol Steppe, Inner Mongolia using NOAA/NDVI. *Grassland Science* **49**, 1–9.

Kawamura, K., T. Akiyama, H.-o. Yokota, M. Tsutsumi, T. Yasuda, O. Watanabe, and S. Wang (2005). Comparing MODIS vegetation indices with AVHRR NDVI for monitoring the forage quantity and quality in Inner Mongolia grassland, China. *Grassland Science* **51**, 33–40.

Keller, F., S. Goyette, and M. Beniston (2005). Sensitivity analysis of snow cover to climate change scenarios and their impact on plant habitats in alpine terrain. *Climatic Change* **72**, 299–319.

Kennedy, P. (1989). Monitoring the vegetation of Tunisian grazing lands using the normalized difference vegetation index. *Ambio* **18**, 119–123.

Key, J. (2002). The Cloud and Surface Parameter Retrieval (CASPR) System for Polar AVHRR - User's Guide. Technical report, Cooperative Institute for Meteorological Satellite Studies, University of Wisconsin, 1225 West Dayton St., Madison, WI 53562.

Lee, T. Y. and Y. J. Kaufman (1986). Non-Lambertian effects on remote sensing of surface reflectance and vegetation index. *IEEE Transactions on Geoscience and Remote Sensing* **24**, 699–708.

Liston, G. E. (1999). Interrelationships among Snow Distribution, Snowmelt, and Snow Cover Depletion: Implications for Atmospheric, Hydrologic, and Ecologic Modeling. *Journal of Applied Meteorology* **38**, 1474–1487.

Liston, G. E. and M. Sturm (1998). A snow-transport model for complex terrain. *Journal of Glaciology* **44**, 498–516.

Los, S., P. North, W. Grey, and M. Barnsley (2005). A method to convert AVHRR Normalized Difference Vegetation Index time series to a standard viewing and illumination geometry. *Remote Sensing of Environment* **99**, 400–411.

Menzel, A. (2000). Trends in phenological phases in Europe between 1951 and 1996. *International Journal of Biometeorology* **44**, 76–81.

Myneni, R. B., C. D. Keeling, G. Tucker, C. J. Asrar, and R. R. Nemani (1997). Increased plant growth in the northern high latitudes from 1981 to 1991. *Nature* **386**, 698–702.

Reed, B. C., J. F. Brown, D. VanderZee, T. R. Loveland, J. W. Merchant, and D. O. Ohlen (1994). Measuring phenological variability from satellite imagery. *Journal of Vegetation Science* **5**, 703–714.

Rhyner, J., M. Bründl, H. J. Etter, M. Steiniger, U. Stöckli, T. Stucki, M. Zimmerli, and W. Amman (2002). Avalanche warning Switzerland - consequences of the avalanche winter 1999. In *Proceedings of the 13th Int. Snow Science Workshop*, Penticton, B.C., Canada.

Roetzer, T., M. Wittenzeller, H. Haeckel, and J. Nekovar (2000). Phenology in central Europe - differences and trends of spring phenophases in urban and rural areas. *International Journal of Biometeorology* **44**, 60–66.

Savitzky, A. and M. J. E. Golay (1964). Smoothing and Differentiation of Data by Simplified Least Squares Procedures. *Analytical Chemistry* **36**, 1627–1639.

Sellers, P., S. O. Los, C. J. Tucker, C. O. Justice, D. A. Dazlich, G. J. Collatz, and D. A. Randall (1996). A Revised Land Surface Parametrization (SiB2) for Atmospheric GCMs. Part II. The Generation of Global Fields of Terrestrial Biophysical Parameters from Satellite Data. *Journal of Climate* **9**, 706–737.

Stöckli, R. and P. L. Vidale (2004). European plant phenology and climate as seen in a 20 year AVHRR land-surface parameter dataset. *International Journal of Remote Sensing* **25**, 3303–3330.

Studer, S., C. Appenzeller, and C. Defila (2005). Inter-Annual Variability and Decadal Trends in Alpine Spring Phenology: A Multivariate Analysis Approach. *Climatic Change* **73**, 395–414.

Studer, S., R. Stöckli, C. Appenzeller, and P. Vidale (2007). A comparative study of satellite and ground-based phenology. *International Journal of Biometeorology* **51**, 405–414.

Teillet, P. M., K. Staenz, and D. J. William (1997). Effects of spectral, spatial, and radiometric characteristics on remote sensing vegetation indices of forested regions. *Remote Sensing of Environment* **61**, 139–149.

Tucker, C. J. and P. J. Sellers (1986). Satellite remote sensing of primary production. *International Journal of Remote Sensing* **7**, 1395–1416.

Tucker, C. J., C. L. Vanpraet, M. J. Sharman, and G. Van Ittersum (1985). Satellite remote sensing of total herbaceous biomass production in the Senegalese Sahel: 1980-1984. *Remote Sensing of Environment* **17**, 233–249.

VEGETATION Programme (1998). SPOT Vegetation User Guide. http://www.spot-vegetation.com/.

Vescovo, L. and D. Gianelle (2006). Mapping the green herbage ratio of grasslands using both aerial and satellite-derived spectral reflectance. *Agriculture, Ecosystems & Environment* **115**, 141–149.

Vescovo, L. and D. Gianelle (2007). Using the MIR bands in vegetation indices for the estimation of grassland biophysical parameters from satellite remote sensing in the Alps region of Trentino (Italy). *Advances in Space Research* **in press**.

Viovy, N., O. Arino, and A. Belward (1992). The Best Index Slope Extraction (BISE): a method for reducing noise in NDVI time-series. *International Journal of Remote Sensing* **13**, 1585–1590.

Walther, G. R., S. Beissner, and H. Pauli (2005). Trends in the upward shift of alpine plants. *Journal of Vegetation Science* **16**, 541–548.

Wanner, H., H. Holzhauser, C. Pfister, and H. Zumbühl (2000). Interannual to century scale climate variability in the European Alps. *Erdkunde* **24**, 62–69.

Wanner, H., R. Rickli, E. Salvisberg, C. Schmutz, and M. Schuepp (1997). Global climate change and variability and its influence on Alpine climate - concepts and observations. *Theoretical and Applied Climatology* **58**, 221–243.

White, M. A., P. E. Thornton, and S. W. Running (1997). A continental phenology model for monitoring vegetation responses to interannual climatic variability. *Global Biogeochemical Cycles* **11**, 217–234.

Wilson, T. and T. Meyers (2007). Determining vegetation indices from solar and photosynthetically active radiation fluxes. *Agricultural and Forest Meteorology* **144**, 160–179.

Winkler, P., M. Lugauer, and O. Reitbuch (2006). Alpine pumping. *promet* **32**, 34–42.

Zhou, L., C. J. Tucker, R. K. Kaufmann, D. Slayback, N. V. Shabanov, and R. B. Myneni (2001). Variations in Northern Vegetation Activity Inferred from Satellite Data of Vegetation Index During 1981 to 1999. *Journal of Geophysical Research* **106**, 20069–20084.

Chapter 5

Perennial snow and ice extent variations in the Arctic circumpolar land area (2000-2008)

Fabio M. A. **Fontana**[1], Alexander P. **Trishchenko**[2], Konstantin V. **Khlopenkov**[2,3], Yi **Luo**[2,4], Samuel U. **Nussbaumer**[1], Stefan **Wunderle**[1]

[1] *Institute of Geography and Oeschger Centre for Climate Change Research, University of Bern, Remote Sensing Research Group, Bern, Switzerland*
[2] *Canada Centre for Remote Sensing, Ottawa, Canada*
[3] *Science Systems and Applications, Inc., Hampton, VA, United States*
[4] *Canadian Ice Service, Ottawa, Canada*

Abstract

Perennial snow and ice (PSI) extent reflects minimum snow and ice conditions at the end of the summer season and is an important parameter of mountain environments with regard to its involvement in the hydrological cycle and the surface energy budget. We investigated interannual variations of PSI in nine mountain regions of interest (ROI) between 2000 and 2008. For that purpose, a novel MODIS dataset processed at the Canada Centre of Remote sensing (CCRS) at 250 m spatial resolution in all seven land bands and covering the Arctic circumpolar area was utilized. The extent of PSI

was found to undergo significant interannual variations, with coefficients of variation (CV) ranging from 5% to 81% depending on the ROI. Variations could in part be explained by a strong and statistically significant negative relationship between PSI and positive degree-days (threshold 0°) during the summer months in some ROIs. Linear correlation coefficients (r) as low as r=−0.90 were obtained. In the European Alps and Scandinavia, PSI extent was significantly correlated with independently derived annual net glacier mass balances, with r=0.92 and r=0.85, respectively. This suggests that PSI extracted from MODIS imagery may be used as an indicator of net glacier mass balances in these areas. Validation of PSI extent in two land surface classifications in 2000 and 2005, GLC-2000 and Globcover, revealed clear misrepresentation of PSI extent by up to 129% in both classifications. With regard to the use of land surface classifications to set up boundary conditions for climate and land surface process models, this is a potential source of error to be investigated in future studies. The results presented here have provided interesting insight into variations of PSI in several ROIs and helped to increase our understanding of sensitive mountain regions in the context of the global climate change discussion.

5.1 Overview

Snow cover and glaciers are important components of the hydrological cycle in many mountain ecosystems (Beniston, 2003). As natural storages of frozen water, they are strongly involved in the modification of the timing and magnitude of water discharge from the mountain areas on various temporal scales (Viviroli et al., 2003). Mountain snow and ice are thereby important modulators of water availability both in mountain regions as well as in surrounding low-lands (Viviroli et al., 2007) and provide water supply for a significant part of the Earth's population (Barnett et al., 2005). Furthermore, hydro-electric power plants as sources of renewable energy heavily rely on water temporarily stored in these reservoirs (Hauenstein, 2005). Apart from issues directly related to water resources, snow and ice exert large influence on climate and the surface energy budget at regional scale (Dewey, 1977; Kotlarski, 2007), e.g. through their high reflectivity or the cooling of the atmosphere. As a result, they are critical parameters to be considered for the assessment of land surface-atmosphere interactions (Hock and Holmgren, 2005). On the other hand, both, snow cover and glaciers provide some of the clearest evidence of climate change, since they are often close to the melting point and, therefore, react sensitively to changes in temperature (UNEP, 2007). In view of the importance of snow cover and glaciers for mountain environments from a wide range of aspects, the study of past, present, and future snow cover and glacier
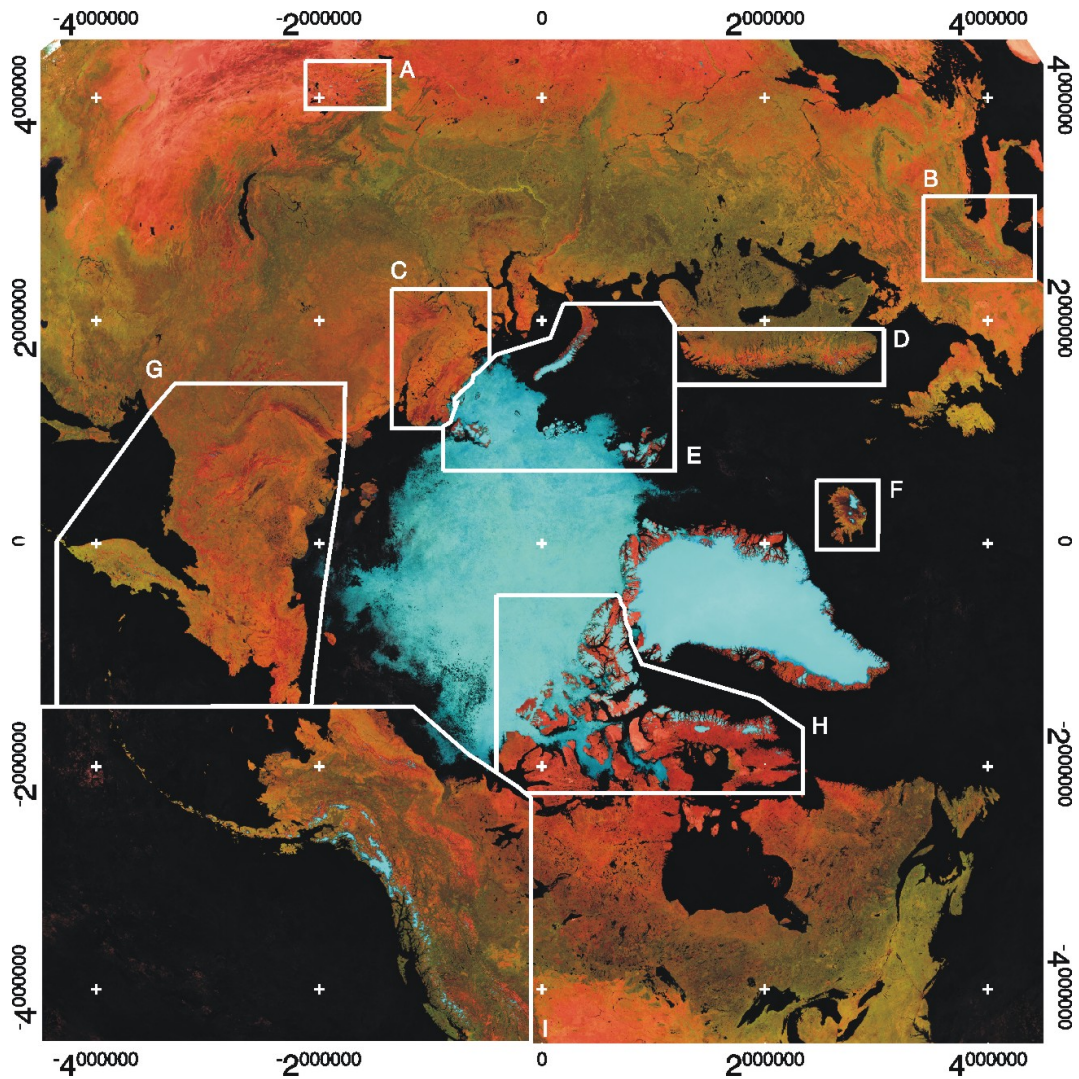
Figure 5.1: *Arctic circumpolar clear-sky mosaic for July to September, 2003, in Lambert Azimuthal Equal-Area (LAEA) projection. Selected regions of interest are delineated in white and labelled according to Table 5.1. Perennial land (and sea) ice extent appears in bluish colors. RGB color scheme: red, band B6 (1.628–1.652µm); green, band B2 (0.841–0.876µm); blue, band B1 (0.62–0.67µm).*

variations has become increasingly important within the global climate change discussion (Lemke et al., 2007). In this context, variations in the spatial extent of perennial snow and ice (PSI) are one important aspect. Perennial snow and ice extent represents minimum snow and ice conditions in mountain regions for a specific year, which are typically observed at the end of the summer season. While interannual changes in the spatial extent of perennial mountain ice, i.e. glaciers and ice caps, are generally small and lag behind climatic changes by at least a few years (Oerlemans, 2001, 148 pp.), larger year-to-year variability is expected for perennial snow cover due to the close

relationship of snow covered area (SCA) with meteorological conditions such as air temperature variations (Robinson and Dewey, 1990).

Satellite remote sensing provides the unique opportunity to study PSI at a wide range of spatial and temporal scales. For studies of perennial mountain ice data from high spatial resolution ($\leq$30 m) sensors are the premier source of information (Paul et al., 2007; Kargel et al., 2005), even though observation frequency of these sensor systems is limited as a consequence of the generally low ground repeat cycles combined with the influence of cloud cover. Studies on snow cover mainly utilized the weekly satellite maps of the northern hemisphere snow cover at a spatial resolution of several kilometers (Robinson et al., 1993; Ramsay, 1998), however, their use for studies of mountain regions is limited because of the coarse spatial resolution. Other snow cover products have become available with the advent of the Moderate Resolution Imaging Spectroradiometer (MODIS) onboard the Terra and Aqua satellites, which offers improved snow and ice detection capabilities due to finer spectral and spatial resolution (Justice et al., 1998). MODIS snow and ice products are available at a range of temporal (daily to monthly) and spatial resolutions (500 m to 0.05°; Hall et al., 2002). However, higher spatial resolution is desirable for studies in rugged terrain in order to capture the patchy mosaic of snow cover (Sirguey et al., 2009). In addition, the Global Climate Observing System (GCOS) has recommended a spatial resolution of 250 m for many Essential Climate Variables (ECVs) intended for terrestrial applications, such as snow cover and albedo (GCOS, 2006, Appendix 2). To meet these requirements and as a contribution to the Canadian component of the International Polar Year (IPY) Programme, a MODIS dataset at 250 m spatial resolution in all seven land bands (MODIS spectral bands B1-B7) and a temporal resolution of 10 days was recently published by the Canada Centre for Remote Sensing (CCRS; Trishchenko et al., 2009). The dataset covers the Arctic circumpolar area (ACA; 9000×9000 km^2) and is centered at the geographic North Pole. If MODIS continues to be operational until the end of 2009, a dataset covering one decade will be available for various applications, such as the analysis of trends in land surface parameters or the determination of land cover types within the ACA at a fine spatial resolution.

In this respect, this dataset may represent a valuable tool not only for the quantification of PSI extent variations, but also for the validation of land surface classifications (LSCs) in complex and spatially heterogeneous mountain regions. Latter application is of particular interest, since LSCs, which are often derived from remote sensing data, are commonly used to set up boundary conditions in climate and land surface process models (Hagemann, 2002). Given the importance of snow and ice for the surface energy budget, accurate delineation of permanently snow and ice covered surfaces in such classifications is a prerequisite. The problem with LSCs is, however, that they

differ with regard to the classification schemes employed, underlying remote sensing data, and the time period considered. As a result, classifications may differ considerably (Hansen and Reed, 2000; Giri et al., 2005), which emphasizes the motivation to validate PSI extent in LSCs using the newly available MODIS dataset as outlined above.

Embedded in this context, the paper is structured as follows: data and methods are introduced in Section 5.2. Interannual PSI variations in a number of mountain regions within the ACA are quantified and discussed in Section 5.3.1. Section 5.3.2 makes use of MODIS-retrieved PSI extent to validate the extent of surfaces classified as PSI in two freely available global LSCs, the Global Land Cover 2000 database (GLC-2000) and the Globcover land cover map in 2005. Research is finally summarized in Section 6.

5.2   Data and methods

5.2.1   MODIS data

The MODIS clear-sky composites for the ACA were generated as described in detail by Trishchenko et al. (2009). In summary, processing includes four major steps: since only bands B1 and B2 of the MODIS sensor are available at 250 m spatial resolution, bands B3 to B7 are downscaled from 500 m to 250 m spatial resolution using an adaptive regression and normalization scheme in a first step (Trishchenko et al., 2006). Second, bands B1 to B7 are reprojected from swath to Lambert Azimuthal Equal Area (LAEA) projection using a gradient search method (Khlopenkov and Trishchenko, 2008), which was shown to preserve the geolocation accuracy achieved by the MODIS science team (Wolfe et al., 2002). In a third step, scene identification at 250 m resolution is performed based on bands B1, B2, B3, and B6. Latter step outputs a mask delineating cloud cover, cloud shadows, and areas observed under clear-sky conditions including information on snow cover. This mask is used in step four together with a set of decision rules to create clear-sky composites for a predefined time interval (Luo et al., 2008). For our purposes, a single clear-sky composite was created per year by merging the highest quality pixels from multiple MODIS scenes during the period from July to September. This was done for the period from 2000 to 2008. The resulting composites represent minimum snow and ice (i.e. PSI) conditions for the ACA, exemplarily shown for the year 2003 in Figure 5.1. Nine regions of interest (ROI) were defined for the analysis of PSI (delineated in white in Figure 5.1), all of them featuring complex topography and areas permanently covered by snow and ice. Greenland as a large ice sheet was excluded from the analysis.

Characteristic spectral surface properties enable the discrimination of PSI from other land cover types (Dozier and Painter, 2004). Regarding the detection of snow and ice, the Normalized Difference Snow Index (NDSI) exploits the reflective properties of snow and ice covered surfaces. The NDSI is calculated by dividing the difference of reflectances observed in MODIS bands B4 and B6 by their sum and may be regarded as a measure of the abundance of snow and ice within the area covered by a pixel. Hence, we generated MODIS PSI maps (PSI$_{MODIS}$) for each ROI and year following Hall et al. (2002), using an NDSI threshold of NDSI$\geq$0.4 and excluding pixels if either the B2 or B4 reflectance was <10%. It is important to note that debris-covered glacier surfaces are not recognized by this approach and, hence, are excluded from analyses. In order to remove sea and lake ice prior to the analyses, a land/water mask was created based on the Global Self-consistent, Hierarchical, High-resolution Shoreline (GSHHS) database (Wessel and Smith, 1996).

5.2.2 Global land cover 2000 map

The Global Land Cover 2000 (GLC-2000) project was led by the Joint Research Institute (JRC) of the European Commission (EC) and included contributions from over 30 research groups around the world (GLC, 2003a). The main objective of the GLC-2000 project was to generate a global land cover database in support of international assessment programs such as the Millennium Ecosystems Assessment. The GLC-2000 land cover classification primarily made use of daily global mosaics of Système Pour l'Observation de la Terre (SPOT) VEGETATION 1 km satellite data acquired between November 1999 and December 2000 (Bartholomé and Belward, 2005). Other data sources were partially used, for example, to overcome limitations due to persistent cloud cover. The database encompasses regionally optimized land cover information as well as a thematically less detailed global legend that combines the regional classifications into a single harmonized global product (Bartholomé and Belward, 2005). The global land cover legend includes 22 classes, following the Land Cover Classification System (LCCS) of the Food and Agriculture Organisation (FAO; Di Gregorio and Jansen, 2000). Applied classification schemes varied depending on the geographic area and the partner institution responsible for a certain regional window (see Fritz et al., 2003 for details on the classification algorithms).

In order to enable the areal comparison of PSI extent between GLC-2000 and MODIS circumpolar imagery, global GLC-2000 data were reprojected from original geographic lat/long to the LAEA projection (1 km spatial resolution). Land cover class 21 ("Snow and ice") was extracted to create PSI maps from GLC-2000 (PSI$_{GLC}$). Given the time

period considered for the GLC-2000 classification scheme, PSI_{MODIS} was compared to PSI_{GLC} in 2000.

5.2.3   Globcover land cover map

The Globcover project was launched in 2004 by the European Space Agency (ESA) and run in collaboration with a number of international organization and scientific programs, such as the United Nations Environment Program (UNEP) and the International Geosphere-Biosphere Programme (IGBP). The aim of the project was to complement and update existing land cover classifications such as the GLC-2000 classification (Section 5.2.2) with a new global land cover map for the year 2005 (Globcover, 2008). The Globcover land cover map is based on 300 m spatial resolution data acquired between December 2004 and June 2006 by the Medium Resolution Imaging Spectrometer (MERIS) onboard Environmental Satellite (ENVISAT). The database includes a global product derived by an automatic and regionally-tuned classification, as well as eleven regional products derived by the same classification system (see Bicheron et al., 2008 for details on the classification steps). Data gaps were filled using a set of reference land cover datasets. The legend of the global product includes 22 classes and is compatible with the LCCS as mentioned in Section 5.2.2.

For consistency with the MODIS data, global Globcover data were reprojected from original geographic lat/long to the LAEA projection (300 m spatial resolution). PSI maps (PSI_{GC}) were obtained by extracting land cover class 220 ("Permanent snow and ice"). The decision on which year to select for the comparison of PSI_{MODIS} and PSI_{GC} is not straightforward, since the time period considered for the Globcover classification includes summer months both in 2005 (entire summer and fall) and 2006 (until June). We argue, however, that minimal snow and ice conditions are not achieved until June in most mountain regions and, therefore, compared PSI_{GC} to PSI_{MODIS} in 2005.

5.3   Results and Discussion

5.3.1   Interannual variations of perennial snow and ice extent

Results of the PSI_{MODIS} extent analysis for the period from 2000 to 2008 are summarized in Table 5.1. Overall, we found PSI extent to exhibit strong interannual variations depending on the ROI, with coefficients of variation (CV) ranging from 5% in the Russian Arctic and Svalbard to 81% in Northern Siberia. In general, observed interannual variability was particularly large in ROIs characterized by relatively small PSI extent (Table 5.1, A–D and G). Combined over all ROIs and years, the CV of PSI_{MODIS} amounted

to 22%. In order to illustrate interannual PSI$_{MODIS}$ variations in more detail, selected geographic subsets within the European Alps and Northern Siberia ROIs are displayed Figures 5.2 and 5.3, respectively. The PSI masks derived as described in Section 5.2.1 are also shown. The years were selected to represent small, about average, and extensive PSI extent conditions for the respective area (see the figure caption for more information). Both figures highlight the large interannual variability, which may be observed in certain ROIs, and demonstrate the high level of spatial detail provided by the circumpolar MODIS composites for the detection of PSI in mountain areas. Note the sea ice along the adjacent coast in Figure 5.3 (bottom), which comes along with extensive PSI extent in the displayed subset.

Given that the extent of perennial mountain ice generally only varies slowly in time (Oerlemans, 2001), its variability is not captured by MODIS imagery at 250 spatial resolution except in cases of pronounced year-to-year ice retreat or advance. Hence, the variations in PSI$_{MODIS}$ as outlined above can mainly be attributed to variations in perennial snow cover, and as such, represents the balance of snow accumulation and melting processes during the preceding seasons. Observed variability of PSI is in line with earlier studies that described interannual variations of PSI in mountain regions (Wang and Xie, 2009) or, on larger scales, of northern hemisphere SCA in summer (Robinson et al., 1993).

Table 5.1: *Results of the perennial snow and ice (PSI) extent analysis for all 9 regions of interest (ROIs) between 2000 and 2008. The ROIs are labelled according to Figure 5.2. CV=coefficient of variation, defined as the standard deviation divided by the mean×100*

	mean [km^2]	CV [%]	PSI$_{MIN}$/PSI$_{MAX}$ [km^2]
A. Altai	1.33×10^3	14	1.02×10^3/1.63×10^3
B. European Alps	2.60×10^3	25	1.93×10^3/4.17×10^3
C. Northern Siberia	1.30×10^3	81	4.96×10^2/3.72×10^3
D. Scandinavia	4.98×10^3	50	2.84×10^3/1.08×10^4
E. Russian Arctic & Svalbard	1.04×10^5	5	9.67×10^4/1.11×10^5
F. Iceland	1.10×10^4	7	1.05×10^4/1.30×10^4
G. Eastern Siberia	3.96×10^3	67	1.77×10^3/9.94×10^3
H. Canadian Arctic	2.01×10^5	10	1.71×10^5/2.36×10^5
I. Western North America	1.32×10^5	13	1.11×10^5/1.67×10^5
All ROIs	4.94×10^5	22	4.23×10^5/5.26×10^5

Table 5.2: *Linear correlation coefficients (r_{Tpos}) between standardized anomalies of PSI$_{MODIS}$ and positive degree-days (threshold 0°C) during selected summer months (2000–2008). Values of $r_{Tpos} < -0.66$ are statistically significant with $p < 0.05$. Results are provided for all nine ROIs according to Figure 5.2.*

	May	June	July	Aug	Sept	May–Sept	June–July	June–Aug	June–Sept	July–Sept
A. Altai	0.09	0.17	−0.72	−0.52	−0.56	−0.52	−0.62	−0.63	−0.72	−0.77
B. European Alps	0.17	−0.63	−0.33	0.16	−0.55	−0.42	−0.64	−0.35	−0.54	−0.38
C. Northern Siberia	−0.54	−0.22	−0.04	−0.79	0.12	−0.60	−0.19	−0.60	−0.59	−0.78
D. Scandinavia	−0.04	−0.56	−0.48	−0.51	−0.37	−0.61	−0.71	−0.68	−0.69	−0.62
E. Russian Archtic & Svalbard	−0.09	−0.57	−0.02	0.64	−0.26	−0.01	−0.37	0.13	−0.02	0.20
F. Iceland	0.19	−0.77	−0.60	−0.42	0.08	−0.37	−0.90	−0.75	−0.54	−0.36
G. Eastern Siberia	−0.25	−0.25	0.19	−0.78	−0.57	−0.75	−0.02	−0.58	−0.81	−0.78
H. Canadian Arctic	0.03	−0.39	−0.17	−0.81	0.27	−0.53	−0.25	−0.54	−0.52	−0.50
I. Western North America	−0.75	−0.60	−0.49	−0.75	−0.03	−0.90	−0.56	−0.70	−0.77	−0.73
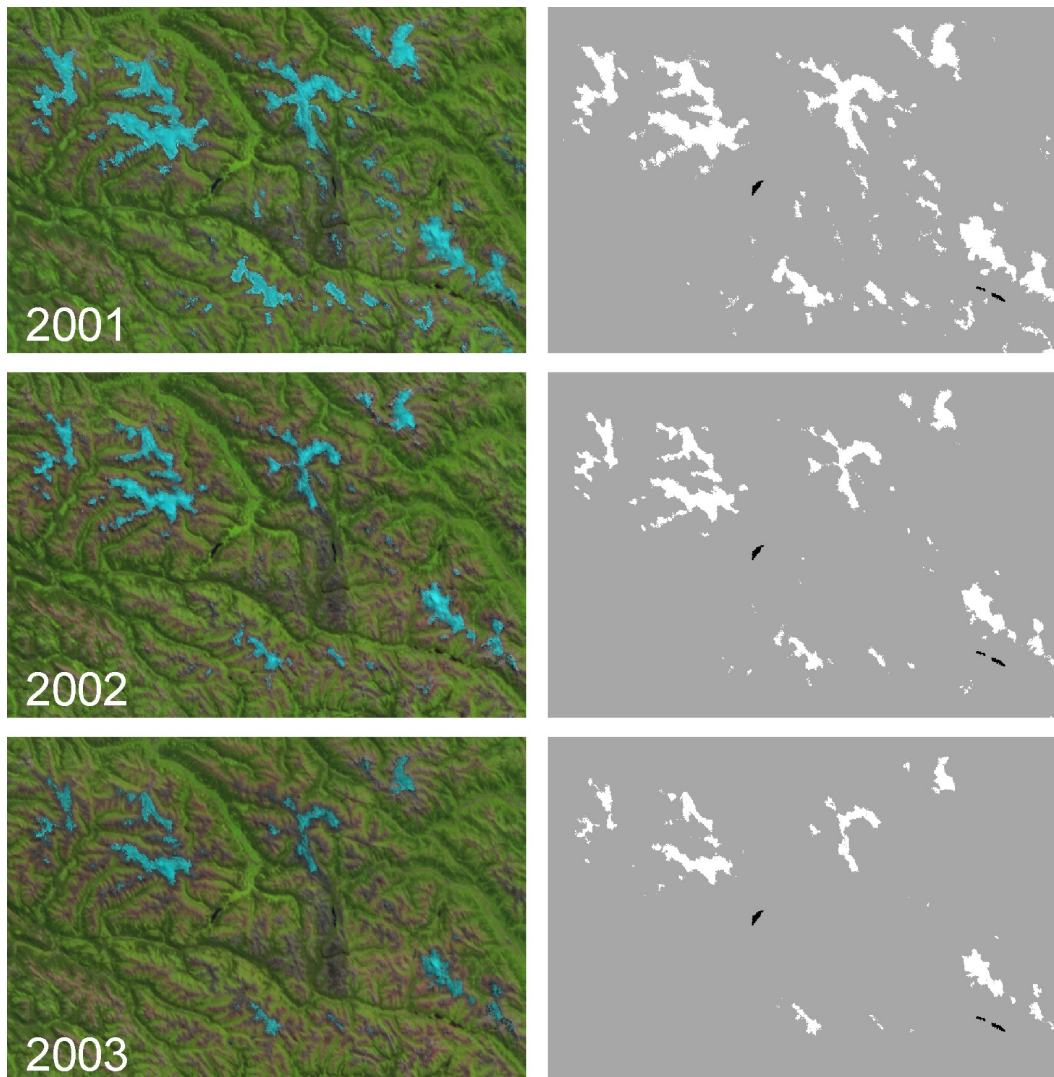
Figure 5.2: *A subset of the European Alps ROI as seen in MODIS circumpolar composites between 2001 and 2003 (left), and the corresponding PSI mask (right, delineated in white). The selected years represent extensive (top), about average (middle), and below average PSI conditions (bottom). The subset covers an area of 150 km×100 km. Water surfaces are marked in black (right).*

Variations in SCA have previously been explained through the close negative relationship between interannual variations of SCA and air temperature (Robinson and Dewey, 1990; Brown, 2000). To place our findings in this context, we investigated the degree to which observed variations in PSI_{MODIS} can be explained by variations in air temperature during the summer season. For that purpose, we computed linear correlation coefficients (r_{Tpos}) between standardized anomalies of both, PSI_{MODIS} and positive degree-days (T_{pos}; threshold 0°C). For the calculation of T_{pos}, 2 m temperature analysis data at 00, 06, 12, and 18 GMT between May and September were consid-
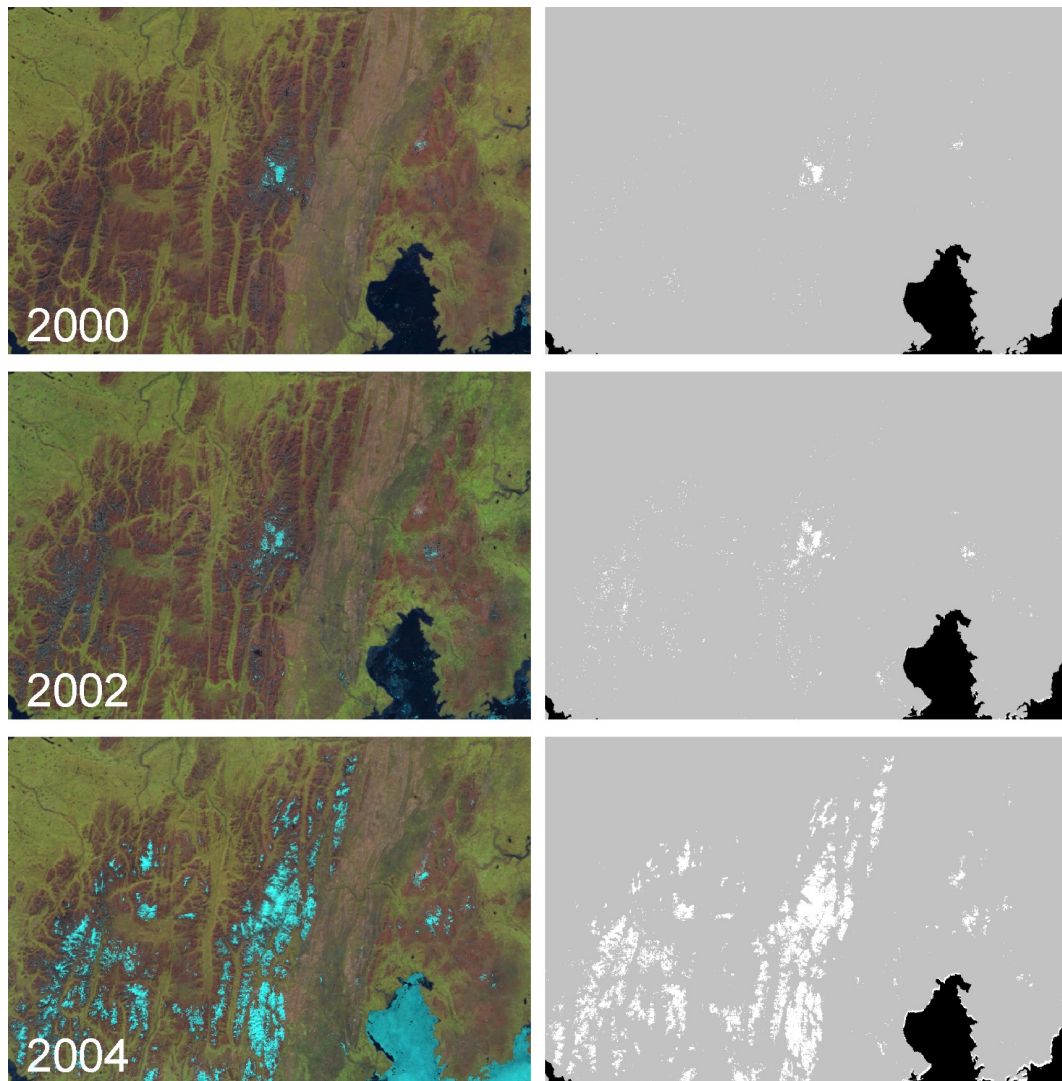
Figure 5.3: *Similar to Figure 5.2, but for a subset of the same areal extent within the Northern Siberia ROI in 2000, 2002, and 2004. Note the sea ice cover that is accounted for by the land/water mask.*

ered for each year (restricted to land surfaces within the ROIs). The temperature data at 0.5° spatial resolution were obtained from the European Centre for Medium-Range Weather Forecasts (ECMWF). Anomalies were standardized with respect to the 2000-2008 period. Results are summarized in Table 5.2. In agreement with the studies as mentioned above, we found strong and statistically significant (p<0.05) negative correlations ($r_{T_{pos}} < -0.66$) between standardized anomalies of T_{pos} and PSI_{MODIS}. In some cases, closest agreements were obtained for positive degree-days in single months, e.g. for Northern Siberia and the Canadian Arctic in August or the Russian Arctic and Svalbard in June. Latter is also in agreement with the findings of Sharp and Wang (2009), who found strong positive correlations between melt durations on glaciers and
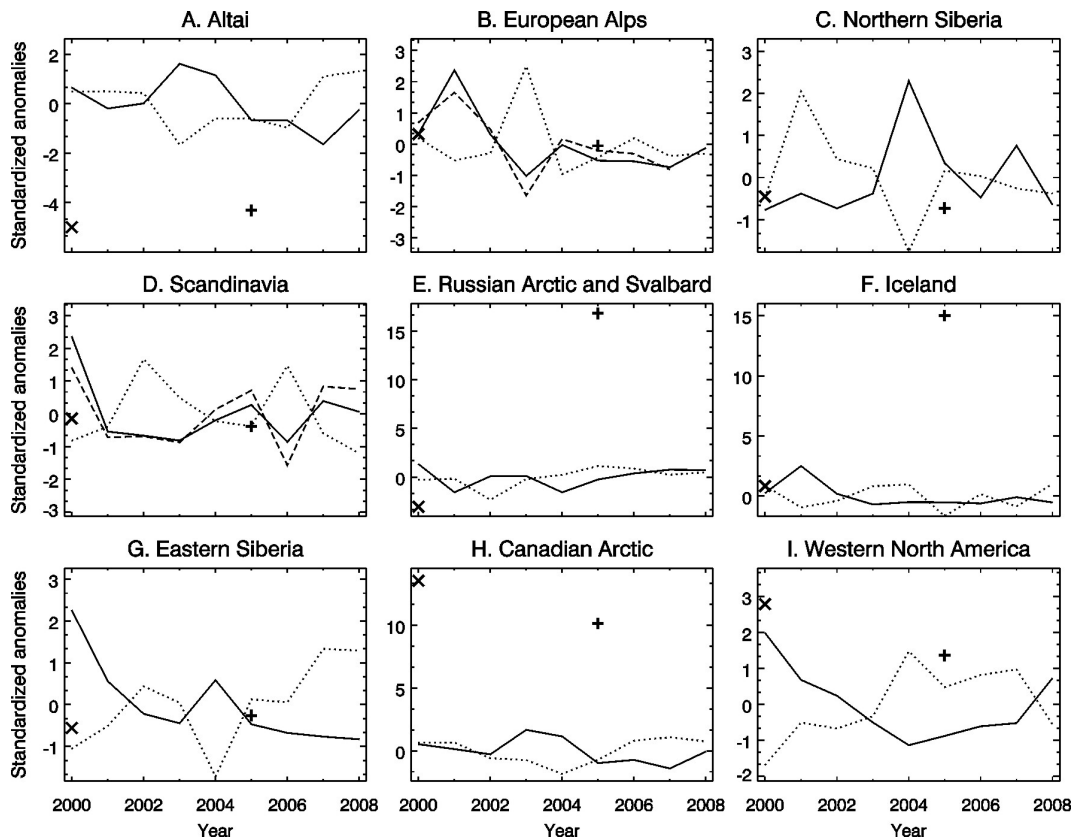
Figure 5.4: *Standardized anomalies of perennial snow and ice (PSI) extent (solid line) and seasonally positive degree-days from May to September (threshold 0°C; dotted line) for all nine regions of interest within the Arctic circumpolar area. Corresponding linear correlation coefficients are provided in Table 5.2. Standardized anomalies of averaged net glacier mass balances (dashed line) are provided for the European Alps and Scandinavia. Net glacier mass balances were compiled for nine (European Alps; 2000-2007) and six glaciers (Scandinavia; 2000-2008). PSI$_{GLC}$ in 2000 ('X'-sign) and PSI$_{GC}$ extent in 2005 ('+'-sign) are also displayed (standardized relative to PSI$_{MODIS}$).*

icecaps in Svalbard, Novaya Zemlya, and Severnaya Zemlya (three archipelagos within ROI E) and temperature at 850 hPa in June. Other ROIs exhibited strongest correlations for positive degree-days over more than one month, e.g. Western North America for the period from May to September, Iceland, Scandinavia, and the European Alps for June and July, or Eastern Siberia for June to September. As an additional illustration, standardized anomalies of PSI$_{MODIS}$ and T$_{pos}$ (May to September) are shown in Figure 5.4. In agreement with the negative values of r$_{Tpos}$ time series of PSI$_{MODIS}$ and T$_{pos}$ exhibit contrary behavior in time.

The negative relationship may in part be explained by the strong snow-albedo feed-back, which has repeatedly been discussed as the driver of SCA variations (e.g. Dery

and Brown, 2007; Groisman et al., 1994), also because the snow–albedo is known to be particularly strong in mountain regions (Giorgi et al., 1997; Fyfe and Flato, 1999). In the northernmost ROIs (C, E, G, and H) sea ice cover is assumed to be a dominant factor governing PSI_{MODIS} (see also Figure 5.3). Sea ice significantly affects climate in polar regions (Lemke et al., 2007), and, through the insulation of the ocean as a source of heat, may influence the duration of the melt season in polar land areas (Sharp and Wang, 2009).

In regard of the close relationship between PSI_{MODIS} and T_{pos}, extreme events such as the summer heat wave in Central Europe in 2003 are of particular interest. In fact, exceptionally warm and dry conditions from May through to the end of August 2003 (Black et al., 2004) as reflected in a strong positive T_{pos} anomaly (Figure 5.4, B) come along with a marked decrease in PSI_{MODIS} in the European Alps in summer 2003. Similarly, a strong decrease in PSI_{MODIS} in 2003 is clearly apparent in Figure 5.2.

Temperature variations are generally the major driver behind snow cover variability by determining snow melt and whether precipitation falls as snow or rain. In other words, PSI_{MODIS} extent is a function of snow accumulation (mainly in winter and spring) and melting/ablation processes during the summer season. Hence, it should be related to another important parameter in mountain regions, which is also governed by the annual meteorological conditions: the net mass balance (b_n) of mountain glaciers. A net glacier mass balance for a specific year and glacier is the sum of the observed winter and summer balances, which both represent a direct and immediate response of the glaciers' thickness and volume to annual atmospheric conditions (Haeberli and Hoelzle, 1995). To test this hypotheses we, therefore, compiled and averaged independently derived net mass balances of nine (European Alps) and six glaciers (Scandinavia) to generate standardized anomalies of mean net glacier mass balance (b_n). These two ROIs were chosen since net glacier mass balance data were available for glaciers well distributed within the respective ROIs and for the entire time period (Scandinavia) and until 2007 (European Alps). Glacier mass balance data were obtained from the World Glacier Monitoring Service (WGMS; www.wgms.ch) and NVE (2009).

Standardized anomalies of b_n are provided in Figure 5.4 (B, D). A close, statistically significant ($p<0.01$), positive relationship between standardized anomalies of PSI_{MODIS} and b_n was obtained, with linear correlation coefficients (r_{b_n}) of $r_{b_n}=0.92$ (European Alps) and $r_{b_n}=0.85$ (Scandinavia).

In a given area we expect the average elevation of the snow line observed at the end of the summer season to be inversely correlated with the extent of PSI_{MODIS} and directly related to the snow line observed on the glacier. The glacier's snow line, on its part, defines the elevation above which the glacier ice is covered by perennial snow

Table 5.3: *Absolute and relative differences of PSI extent as extracted from the Global Land Cover (GLC-2000) as well as Globcover land surface classifications with respect to PSI_{MODIS}. Differences indicated for GLC-2000 (Globcover) refer to PSI_{MODIS} in 2000 (2005). Positive (negative) values denote cases, where the land cover products overestimate (underestimate) PSI extent.*

	PSI_{MODIS} (2000) [km²]	GLC-2000 abs [km²]	GLC-2000 rel [%]	PSI_{MODIS} (2005) [km²]	Globcover (2005) abs [km²]	Globcover (2005) rel [%]
A. Altai	1.45×10^3	-1.06×10^3	-73	1.21×10^3	-6.85×10^2	-57
B. European Alps	2.82×10^3	-5	0	2.25×10^3	3.15×10^2	14
C. Northern Siberia	4.96×10^2	3.31×10^2	67	1.66×10^3	-1.12×10^3	-68
D. Scandinavia	1.08×10^4	-6.22×10^3	-57	5.66×10^3	-1.63×10^3	-29
E. Russian Arctic & Svalbard	1.11×10^5	-2.12×10^4	-19	1.03×10^5	8.25×10^4	80
F. Iceland	1.12×10^4	4.77×10^2	4	1.06×10^4	1.22×10^4	115
G. Eastern Siberia	9.94×10^3	-7.45×10^3	-75	2.72×10^3	5.55×10^2	20
H. Canadian Arctic	2.12×10^5	2.71×10^5	128	1.80×10^5	2.32×10^5	129
I. Western North America	1.67×10^5	1.42×10^4	8	1.16×10^5	3.98×10^4	34
All ROIs	5.26×10^5	2.50×10^5	47	4.23×10^5	3.64×10^5	86

and névé and can be regarded as a rough approximation of the glacier's equilibrium line in a given year (Paterson, 1994). As such, it is directly correlated to the annual b_n. Results, therefore, suggest that PSI_{MODIS}, as a parameter reflecting the areal extent of snow (and ice) cover, can be regarded as an indicator of the (volumetric) parameter b_n in the mountain areas of Scandinavia and the European Alps. These results are of particular interest with regard to the urgent requirement for information on glacier mass balances on larger spatial scales (Lemke et al., 2007) and may represent an alternative to the extrapolation of local measurements made at a few generally small glaciers.

As mentioned earlier, accurate knowledge of PSI extent is required to set up boundary conditions in climate and land surface process models. The MODIS circumpolar imagery at 250 m spatial resolution provides a good opportunity to validate PSI extent as delineated in LSCs in mountain regions. This will be the subject of the following section.

5.3.2   Circumpolar MODIS imagery vs. land surface classifications

Absolute and relative differences between PSI_{GLC} and PSI_{GC} on the one hand and PSI_{MODIS} on the other hand were determined and are provided in Table 5.3. In addition, PSI extent in both LSCs is illustrated in Figure 5.4 (standardized relative to PSI_{MODIS}). While there is a relatively good agreement between PSI_{MODIS} and PSI_{GLC} in certain cases (relative errors <10%), namely for the European Alps, Iceland, and Western North America, in the majority of the cases PSI_{GLC} and PSI_{GC}, in particular, clearly differ from PSI_{MODIS}. For some ROIs such as the Canadian Arctic (both LSCs) or Iceland (Globcover), large differences were obtained (>100%). Added for all ROIs, PSI extent is overestimated in PSI_{GLC} (PSI_{GC}) by 47% (86%). To illustrate the discrepancies between the datasets, Figures 5.5 and 5.6 display subsets of the circumpolar composites (Figures 5.5/5.6, left), corresponding PSI maps (middle), and $PSI_{GLC/GC}$ (right). Except for the Canadian Arctic ROI (Figures 5.5/5.6, A), small subsets were selected to show the PSI extent in more detail. Consistent with the statistics provided in Table 5.3, the overestimation of PSI extent in both LSCs is clearly apparent in the Canadian Arctic ROI. Figure 5.5 (B) demonstrates for a small subset in the European Alps that GLC-2000, overall, accurately classifies PSI in 2000 for this area. In contrast, PSI is underestimated by GLC-2000 in the Altai mountain range (C). Similarly, Figure 5.6 (B) shows an example in the European Alps where the discrepancies between PSI_{MODIS} and PSI_{GC} were small. In Northern Siberia, however, PSI extent was found to be clearly underestimated in the Globcover product (Figure 5.6, C).

The magnitude of the obtained differences in PSI extent for some ROIs was somewhat surprising. Differences in the spatial resolution of the classification are one reason
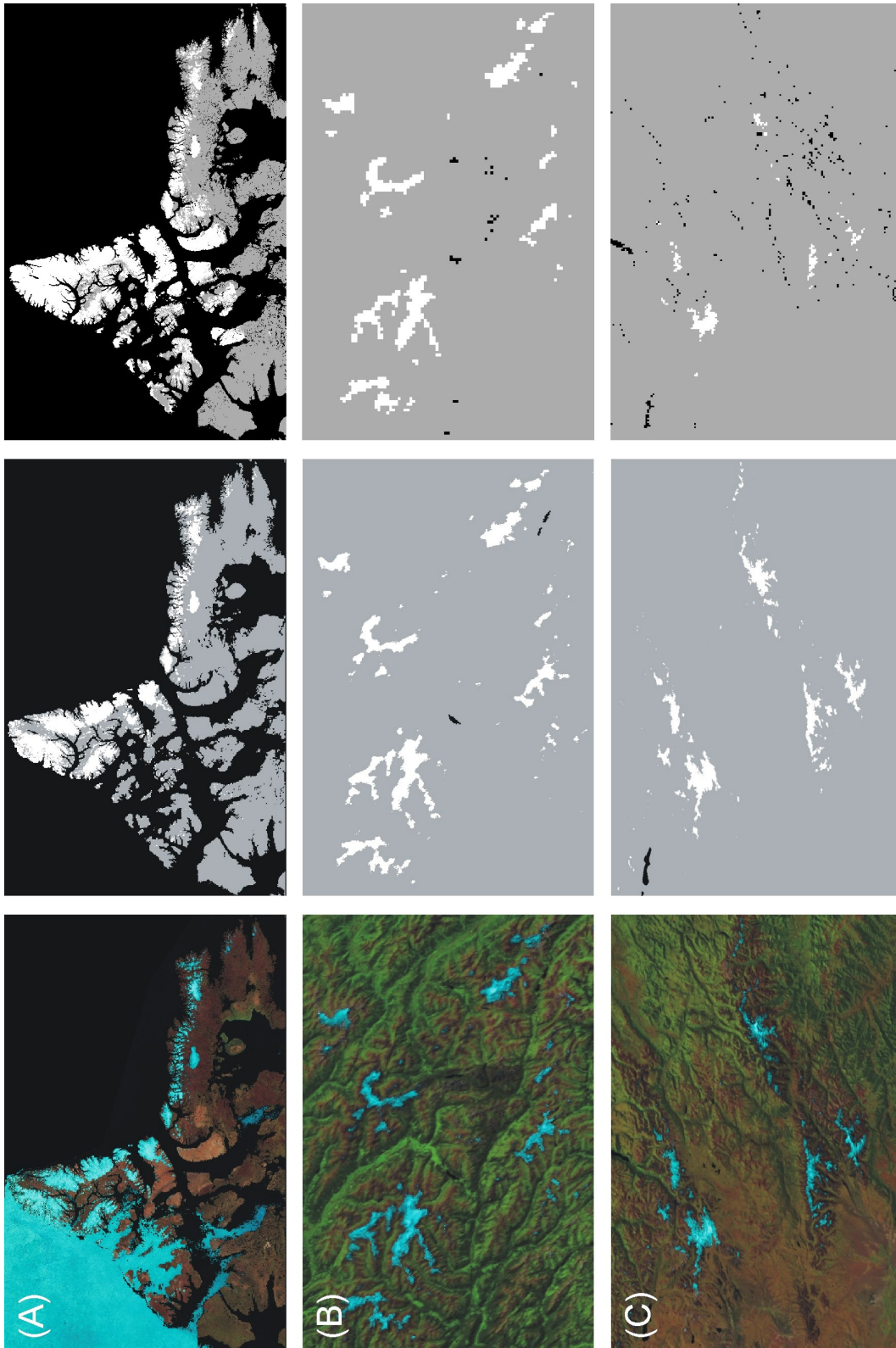
for the observed discrepancies, since small snow patches may not be included in the GLC-2000 product at 1 km spatial resolution. However, this can certainly not explain the large deviations we observed. Regarding the GLC-2000 classification, the maximum Normalized Difference Vegetation Index (NDVI) compositing scheme used to minimize cloud contamination in the data should be discussed as a possible source of error. Clear-sky composite data generated using this compositing scheme served as an input for classification in a number of GLC-2000 regional windows, such as North Eastern Europe (including the Scandinavia ROI) or Northern Eurasia (including the Eastern Siberia as well as the Altai ROIs). The maximum NDVI scheme selects the highest NDVI value within a predefined period based on the assumption that the NDVI is decreased due to the influence of e.g. clouds (Holben, 1986). The problem is, however, that this compositing scheme will generally select cloud observations over snow covered (i.e. PSI) surfaces, since the NDVI of clouds is higher compared to the NDVI of snow. If cloud contaminated observations are subsequently removed and replaced by post-seasonal correction algorithms (Bartholomé and Belward, 2005, and references therein), it will likely lead to errors in the composite data underlying the classification schemes. In this context, it is interesting to note that in the European Alps ROI, where the differences between PSI$_{MODIS}$ and PSI$_{GLC}$ were marginal, a different clear-sky compositing scheme was selected (Vancutsem et al., 2007). In the case of the Canadian Arctic ROI, areas north of approx. 75°N revealed largest discrepancies, which may be explained by inconsistencies due to MODIS imagery being used as input for unsupervised classification between 75°N-80°N and data from the Advanced Very High Resolution Radiometer (AVHRR) between 80°N-90°N (GLC, 2003b). However, to our knowledge no detailed information on the data processing steps in these areas are available.

As for the Globcover classification, sparse data collection of the MERIS instrument due to a smaller swath width compared to MODIS (1150 km vs. 2330 km) may result in discrepancies, as this reduces the chance of a geographic location being observed

---

Figure 5.5 *(facing page)*: *MODIS circumpolar RGB imagery in 2000 (left), corresponding PSI$_{MODIS}$ (middle), and PSI$_{GLC}$ (right). Three areas are displayed: The northern Canada ROI (A; 2750×1775 km^2), a subset of the European Alps ROI (B; 150×100 km^2), and a subset of the Altai mountain range within the Altai ROI (C; 255×166 km^2). While there is a good agreement between PSI$_{MODIS}$ and PSI$_{GLC}$ in the European Alps, the extent of PSI is clearly overestimated (underestimated) in the Canadian Arctic ROI (Altai subset) by the GLC-2000 classification (cf. Table 5.3). Color code for the PSI maps: white, PSI; black, water surfaces, grey, snow/ice free land surfaces.*

(A) (B) (C)
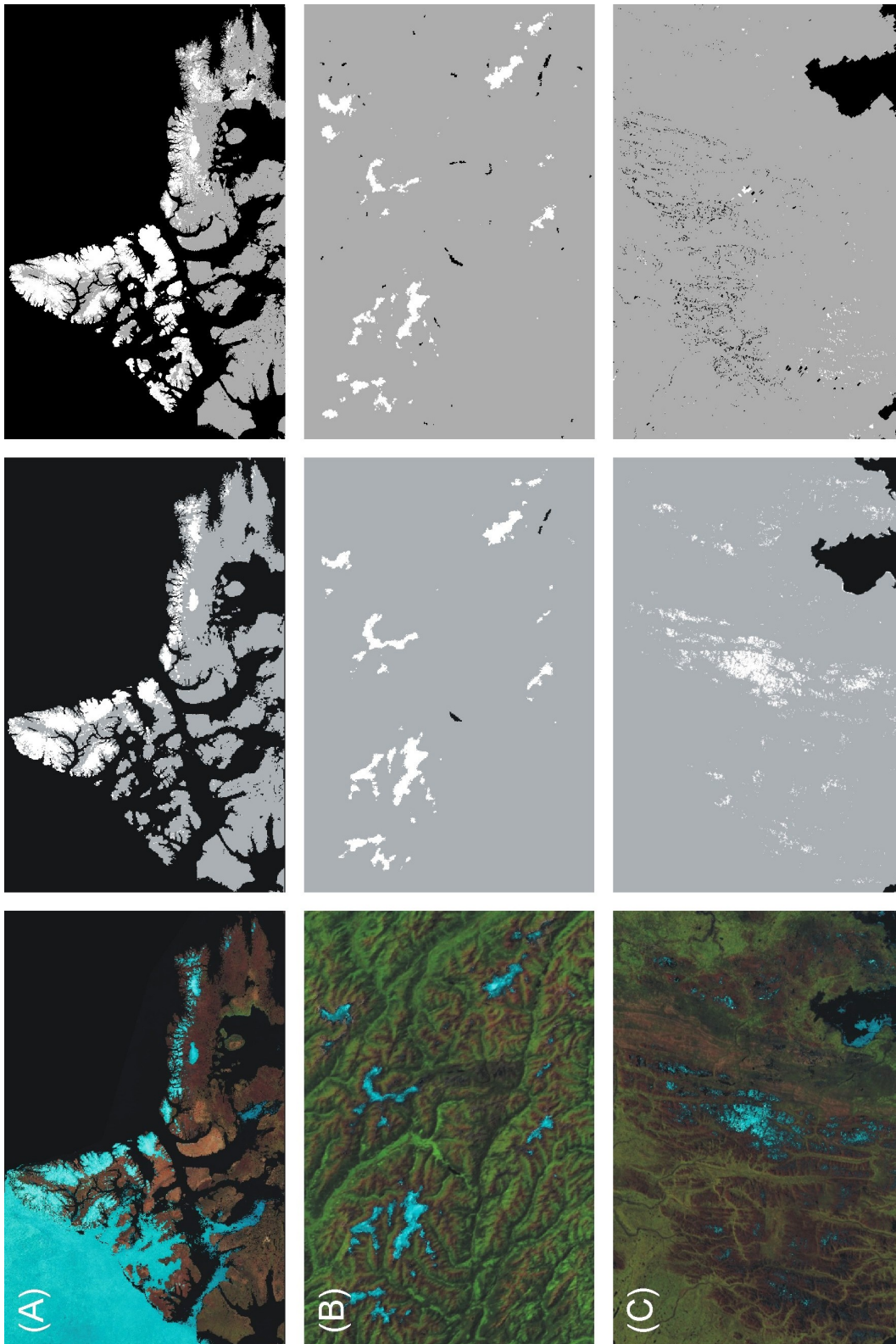
under cloud- and snow-free conditions. Especially in Western North America, Canadian Arctic, and both Siberia ROIs, the number of valid MERIS observations during the considered period is very low ($\leq$10; Bicheron et al., 2008). In addition, MERIS only covers a small range of the electromagnetic spectrum (0.4-0.9μm) compared to the entire solar spectrum measured by MODIS, which presumably limits its ability to discriminate between land cover types. Additional errors are eventually introduced to the Globcover product where a reference dataset was used to fill gaps due to missing data (Bicheron et al., 2008).

With regard to LSCs being used to set up boundary conditions in climate and land surface process models (Hagemann, 2002), the accurate delineation of PSI in land cover products is important, since inaccurate boundary conditions potentially lead to erroneous climate simulations (Hagemann et al., 1999). While the impact of PSI misclassification on the assessment of land surface-atmosphere fluxes may be limited to local scales for ROIs exhibiting small PSI extent (e.g. the Altai mountain range or Northern Siberia), it is likely to be more relevant for simulations at larger scales for ROIs characterized by large areas of PSI (e.g. Canadian Arctic or Western North America). However, the quantification of this impact remains to be addressed in future studies.

5.4 Concluding remarks

Perennial snow and ice extent represents minimum snow and ice conditions in mountain regions at the end of the summer season and, as such, reflects the balance of melting and accumulation processes during the previous seasons. We made use of a newly developed MODIS dataset at 250 m spatial resolution to quantify interannual variations in PSI extent in nine ROIs in the Arctic circumpolar area between 2000 and 2008. Depending on the ROI, large interannual variability of PSI was detected, which could in part be explained by variations in summer air temperature and likely reflects the snow-albedo feedback. Independent time series of averaged net glacier mass balances showed a very close agreement with PSI extent in Scandinavia and in

Figure 5.6 *(facing page): MODIS circumpolar RGB imagery in 2005 (left), corresponding PSI$_{MODIS}$ (middle), and PSI$_{GC}$ (right). Three areas are displayed: The northern Canada ROI (A; 2750 km$\times$1775 km), a subset of the European Alps ROI (B; 150 km$\times$100 km), and a subset of the Northern Siberia ROI (C; 150 km$\times$100 km). The extent of PSI is clearly overestimated in PSI$_{GC}$ for the Canadian Arctic ROI, but underestimated in the European Alps and, in particular, in northern Siberia (cf. Table 5.3). Color code for the PSI maps: white, PSI; black, water surfaces, grey, snow/ice free land surfaces.*

the European Alps, which suggests that PSI variations may serve as an indicator of net glacier mass balances in these areas. This is of particular interest with regard to the need for information on glacier mass balances on broad spatial scales. Finally, the circumpolar MODIS imagery was employed to validate PSI extent in two land surface classifications, GLC-2000 and Globcover. PSI extent was found to be clearly misrepresented in both land surface classifications, which is of interest with regard to the use of such classifications to set up boundary conditions in climate and land surface process models. Inaccurate representation of permanently snow and ice covered areas potentially leads to erroneous model output. This is of particular interest for large ROIs exhibiting extensive PSI coverage, as a misclassification of PSI in these areas may affect model output at large spatial scales through the snow-albedo effect. Circumpolar MODIS imagery has provided interesting and novel insight into PSI variations in several mountain ranges at high spatial resolution. With regard to the importance of snow and ice for many land surface and hydrological processes, the results presented here will enhance our understanding of future climate change impact on mountain regions.

Acknowledgements

References

Barnett, T. P., J. C. Adam, and D. P. Lettenmaier (2005). Potential impacts of a warming climate on water availability in snow-dominated regions. *Nature* **438** (7066), 303–309.

Bartholomé, E. and A. S. Belward (2005). GLC2000: a new approach to global land cover mapping from Earth observation data. *International Journal of Remote Sensing* **26** (9), 1959–1977.

Beniston, M. (2003). Climatic Change in Mountain Regions: A Review of Possible Impacts. *Climatic Change* **59** (1), 5–31.

Bicheron, P., P. Defourny, C. Brockmann, L. Schouten, C. Vancutsem, M. Huc, S. Bontemps, M. Leroy, F. Achard, M. Herold, F. Ranera, and O. Arino (2008). GLOBCOVER: Products Description and Validation Report. available at: http://ionia1.esrin.esa.int/index.asp.

Black, E., M. Blackburn, G. Harrison, B. Hoskins, and J. Methven (2004). Factors contributing to the summer 2003 European heatwave. *Weather* **59** (8), 217–223.

Brown, R. D. (2000, jul). Northern Hemisphere Snow Cover Variability and Change, 1915–1997. *Journal of Climate* **13** (13), 2339–2355.

Dery, S. J. and R. D. Brown (2007). Recent Northern Hemisphere snow cover extent trends and implications for the snow-albedo feedback. *Geophys. Res. Lett.* **34**, –.

Dewey, K. F. (1977). Daily Maximum and Minimum Temperature Forecasts and the Influence of Snow Cover. *Monthly Weather Review* **105** (12), 1594–1597.

Di Gregorio, A. and L. J. M. Jansen (2000). Land Cover Classification System (LCCS): Classification Concepts and User Manual. Available on line at: http://www.fao.org/DOCREP/003/X0596E/X0596e00.htm.

Dozier, J. and T. H. Painter (2004). Multispectral and hyperspectral remote sensing of alpine snow properties. *Annual Review of Earth and Planetary Science* **32** (1), 465–494.

Fritz, S., E. Bartholome, A. Belward, A. Hartley, H. Stibig, E. Hugh, P. Mayaux, S. Bartalev, R. Latifovic, S. Kolmert, P. S. Roy, S. Agrawal, W. Bingfang, X. Wenting, M. Ledwith, J. Pekel, C. Giri, S. Mücher, E. de Badts, R. Tateishi, J. Champeaux, and P. Defourny (2003). Harmonization, mosaicking, and production of the Global Land Cover 2000 database. Ispra, Italy. Joint Research Center (JRC).

Fyfe, J. C. and G. M. Flato (1999). Enhanced Climate Change and Its Detection over the Rocky Mountains. *Journal of Climate* **12** (1), 230–243.

GCOS (2006). Systematic Observation Requirements for Satellite-based Products for Climate: Supplemental details to the satellite-based component of the Implementation plan for the Global Observing System for Climate in support of the UNFCC. GCOS-107, WMO/TD-1338.

Giorgi, F., J. W. Hurrell, M. R. Marinucci, and M. Beniston (1997). Elevation Dependency of the Surface Climate Change Signal: A Model Study. *Journal of Climate* **10** (2), 288–296.

Giri, C., Z. Zhu, and B. Reed (2005). A comparative analysis of the Global Land Cover 2000 and MODIS land cover data sets. *Remote Sensing of Environment* **94**, 123–132.

GLC (2003a). Global Land Cover 2000 database. European Commission, Joint Research Centre. Available online at: http://www.gvm.jrc.it/glc2000.

GLC (2003b). Global Land Cover 2000 database. Update information Version 1. European Commission, Joint Research Centre. Available online at: http://bioval.jrc.ec.europa.eu/products/glc2000/products/Update_version1.pdf.

Globcover (2008). Globcover land cover database. ESA and the ESA Globcover Project, led by MEDIAS-France. Available online at: http://ionia1.esrin.esa.int/.

Groisman, P., T. R. Karl, R. W. Knight, and G. L. Stenchikov (1994). Changes of Snow Cover, Temperature, and Radiative Heat Balance over the Northern Hemisphere. *Journal of Climate* **7**, 1633– 1656.

Haeberli, W. and M. Hoelzle (1995). Application of inventory data for estimating characteristics of and regional climate-change effects on mountain glaciers: a pilot study with the European Alps. *Annals of Glaciology* **21**, 206–212.

Hagemann, S. (2002). An improved land surface parameter dataset for global and regional climate models. Report 336, Max-Planck- Institute for Meteorology, Hamburg.

Hagemann, S., M. Botzet, L. Dümenil, and M. Machenhauer (1999). Derivation of global GCM boundary conditions from 1 km land use satellite data. Report 289, Max-Planck-Institute for Meteorology, Hamburg.

Hall, D. K., G. A. Riggs, V. V. Salomonson, N. E. DiGirolamo, and K. J. Bayr (2002). MODIS snow-cover products. *Remote Sensing of Environment* **83** (1-2), 181–194.

Hansen, M. and B. Reed (2000). A comparison of the IGBP DISCover and University of Maryland 1 km global land cover products. *International Journal of Remote Sensing* **21** (6–7), 1365 –1373.

Hauenstein, W. (2005). Hydropower and Climate Change - Reciprocal Relation: Institutional Energy Issues in Switzerland. *Mountain Research and Development* **25** (4), 321–325.

Hock, R. and B. Holmgren (2005). A distributed surface energy-balance model for complex topography and its application to Storglaciären, Sweden. *Journal of Glaciology* **51**, 25–36.

Holben, B. N. (1986). Characteristics of maximum-value composite images from temporal AVHRR data. *International Journal of Remote Sensing* **7** (11), 1417–1434.

Justice, C. O., E. Vermote, J. R. G. Townshend, R. Defries, D. P. Roy, D. K. Hall, V. V. Salomonson, J. L. Privette, G. Riggs, A. Strahler, W. Lucht, R. B. Myneni, Y. Knyazikhin, S. W. Running, R. R. Nemani, Z. Wan, A. R. Huete, W. van Leeuwen, R. E. Wolfe, L. Giglio, J. Muller, P. Lewis, and M. J. Barnsley (1998). The Moderate Resolution Imaging Spectroradiometer (MODIS): Land Remote Sensing for Global Change Research. *IEEE Transactions on Geoscience and Remote Sensing* **36** (4), 1228–1249.

Kargel, J. S., M. J. Abrams, M. P. Bishop, A. Bush, G. Hamilton, H. Jiskoot, A. Kääb, H. H. Kieffer, E. M. Lee, F. Paul, F. Rau, B. Raup, J. F. Shroder, D. Soltesz, D. Stainforth, L. Stearns, and R. Wessels (2005). Multispectral imaging contributions to global land ice measurements from space. *Remote Sensing of Environment* **99** (1-2), 187–219.

Khlopenkov, K. V. and A. P. Trishchenko (2008). Implementation and evaluation of concurrent gradient search method for reprojection of MODIS level 1B imagery. *IEEE Transaction on Geoscience and Remote Sensing* **46**, 2016–2027.

Kotlarski, S. (2007). *A Subgrid Glacier Parameterisation for Use in Regional Climate Modelling*. Reports on earth system science (42/2007), Max Planck Institute for Meteorology.

Lemke, P., J. Ren, R. Alley, I. Allison, J. Carrasco, G. Flato, Y. Fujii, G. Kaser, P. Mote, R. Thomas, and T. Zhang (2007). Observations: Changes in Snow, Ice and Frozen Ground. In S. Solomon, D. Qin, M. Manning, Z. Chen, M. Marquis, K. B. Averyt, M. Tignor, and H. L. Miller (eds.), *Climate Change 2007: The Physical Science Basis. Contribution of Working Group I to the Fourth Assessment Report of the Intergovernmental Panel on Climate Change*. Cambridge University Press, Cambridge, United Kingdom and New York, NY, USA.

Luo, Y., A. P. Trishchenko, and K. V. Khlopenkov (2008). Developing clear-sky, cloud and cloud shadow mask for producing clear-sky composites at 250-meter spatial resolution for the seven MODIS land bands over Canada and North America. *Remote Sensing of Environment* **112** (12), 4167–4185.

NVE (2009). *Glaciological investigations in Norway in 2008*. (Andreassen, L. M. and Elvehøy, H. and Jackson, M. and Kjøllmoen, B. and Giesen, R. H. and Tvede, A. M.); Report No 2. Norwegian Water Resources and Energy Directorate (NVE), Oslo.

Oerlemans, J. (2001). *Glaciers and Climate Change*. Rotterdam, The Netherlands: Balkema.

Paterson, W. S. B. (1994). *The physics of glaciers*. 3rd edition. Elsevier Science, Oxford, 481 pp.

Paul, F., A. Kääb, and W. Haeberli (2007). Recent glacier changes in the Alps observed by satellite: consequences for future monitoring strategies. *Global and Planetary Change* **56** (1–2), 111–122.

Ramsay, B. H. (1998). The interactive multisensor snow and ice mapping system. *Hydrological Processes* **12**, 1537–46.

Robinson, D. A. and K. F. Dewey (1990). Recent secular variations in the extent of northern hemisphere snow cover. *Geophys. Res. Lett.* **17**, 1557–1560.

Robinson, D. A., K. F. Dewey, and R. R. Heim (1993). Global Snow Cover Monitoring: An Update. *Bulletin of the American Meteorological Society* **74** (9), 1689–1696.

Sharp, M. and L. Wang (2009). A Five-Year Record of Summer Melt on Eurasian Arctic Ice Caps. *Journal of Climate* **22** (1), 133–145.

Sirguey, P., R. Mathieu, and Y. Arnaud (2009). Subpixel monitoring of the seasonal snow cover with MODIS at 250m spatial resolution in the Southern Alps of New Zealand: Methodology and accuracy assessment. *Remote Sensing of Environment* **113** (1), 160–181.

Trishchenko, A. P., Y. Luo, and K. V. Khlopenkov (2006). A method for downscaling MODIS land channels to 250 m spatial resolution using adaptive regression and normalization. In *Proceedings of SPIE - The International Society for Optical Engineering*, Volume v.6366, pp. 8.

Trishchenko, A. P., Y. Luo, K. V. Khlopenkov, W. M. Park, and S. Wang (2009). Arctic circumpolar mosaic at 250 m spatial resolution for IPY by fusion of MODIS/TERRA land bands B1-B7. *International Journal of Remote Sensing* **30** (6), 1635–1641.

UNEP (2007). *Global outlook for snow and ice*. United Nations Environment Programme.

Vancutsem, C., J. Pekel, P. Bogaert, and P. Defourny (2007). Mean Compositing, an alternative strategy for producing temporal syntheses. Concepts and performance assessment for SPOT VEGETATION time series. *International Journal of Remote Sensing* **28** (22), 5123–5141.

Viviroli, D., H. H. Duerr, B. Messerli, M. Meybeck, and R. Weingartner (2007). Mountains of the world, water towers for humanity: Typology, mapping, and global significance. *Water Resources Research* **43**, 1–13.

Viviroli, D., Weingartner R., and B. Messerli (2003). Assessing the Hydrological Significance of the Worlds Mountain. *Mountain Research and Development* **23** (1), 32–40.

Wang, X. and H. Xie (2009). New methods for studying the spatiotemporal variation of snow cover based on combination products of MODIS Terra and Aqua. *Journal of Hydrology* **371** (1-4), 192–200.

Wessel, P. and W. H. F. Smith (1996). A global, self-consistent, hierarchical, high-resolution shoreline database. *Journal of Geophysical Research* **101** (B4), 8741–8743.

Wolfe, R. E., M. Nishihama, A. J. Fleig, J. A. Kuyper, D. P. Roy, J. C. Storey, and F. S. Patt (2002). Achieving sub-pixel geolocation accuracy in support of MODIS land science. *Remote Sensing of Environment* **83** (1-2), 31–49.

Chapter 6

Concluding remarks

Mountain environments are particularly sensitive to variations in the Earth's climatic system and have, therefore, gained increasing importance in the global change discussion. In this context, remote sensing was identified as an integral part of the monitoring strategies. Among a multitude of possible applications based on a wide variety of sensor systems, data from the AVHRR and MODIS sensor systems may be employed to observe land surface parameters at a high temporal resolution and on broad spatial scales. The studies in this thesis have clearly demonstrated the high potential of the AVHRR and MODIS sensors for observations of land surface parameters in mountain regions at various spatial scales. The focus was entirely set on vegetation, snow, and ice, due to the importance of these three land surface types for many mountain environments.

In a first study at local to regional scale, the impact of elevated topography on the geometric accuracy of AVHRR-derived climate data records was investigated with regard to the GCOS geolocation accuracy requirements (Chapter 3). Investigations were based on maximum NDVI composite data. Obtained results emphasize that geometric distortions introduced to satellite imagery through the intertwined effects of observation geometry and surface elevation should be corrected for through the process of orthorectification. Neglecting these effects may lead to important biases in NDVI datasets and to a loss of spatial information at various spatial scales. The study also showed that maximum NDVI composite data originating from the AVHRR GAC data format should be used with caution in future studies of spatially heterogeneous mountain regions. A systematic average positive bias caused by the GAC sampling scheme was identified. This bias likely contributes to the systematic average positive biases we observed relative to our results in AVHRR GAC-based composites from the GIMMS and PPF datasets. The conclusions of this study accentuate the importance of the task on reprocessing AVHRR 1-km imagery for climate studies for two reasons: first,

only few AVHRR processing systems have so far accounted for the geometric distortions introduced to AVHRR imagery by elevated topography, which limits the use of AVHRR-derived climate data records for studies of sensitive mountain regions. Second, GAC-based NDVI data records contain inherent positive biases in spatially heterogeneous mountain regions that cannot be corrected for.

A problem often encountered when using remote sensing imagery for studies of mountain regions is the lack of ground validation data. In this context, the comparative study of satellite and ground based phenology at local scale presented in Chapter 4 made an important contribution. At 15 alpine and subalpine grassland sites, three grassland growth parameters obtained from in situ measurements (melt-out, start of growth, and end or growth) were derived from satellite NDVI time series. All three parameters were estimated consistently by NDVI time series from AVHRR and two newer generation sensors, MODIS and VEGETATION. The study also emphasized the necessity to account for the influence of persistent cloud cover in NDVI time series in mountainous regions through the application of smoothing algorithms. In this regard, a modified version of a commonly used Fourier adjustment algorithm provided better results compared to a Savitzky-Golay filter. Given that in situ data are available since 1998, future studies in this context should be extended back in time and, hence, include various satellites from the NOAA series. This will enable us to validate decade-long time NDVI time series at several alpine grassland sites and to gain more detailed insight into possible reasons for discrepancies between remote sensing and ground measurements. Thoroughly validated NDVI time series will be a great benefit with regard to the exploitation of the extensive RSGB AVHRR data record for studies of vegetation dynamics in the European Alps.

In view of the importance of mountain snow and glaciers for the hydrological cycle and the regional climate in mountains and surrounding low-lands, interannual variations of perennial snow and ice (PSI) extent in nine ROIs were quantified (Chapter 5). A newly developed MODIS dataset covering the Arctic circumpolar area at 250 m spatial resolution in all seven land bands was used. The dataset has proven to be a valuable tool for the quantification of PSI extent variations at regional to continental scale and at high spatial resolution in accordance with the GCOS requirements. Strong negative relationships between PSI extent and positive degree-days during the summer months were observed for some ROIs, which is in line with previous discussions of the snow-albedo feedback in the Northern Hemisphere. The good agreement of PSI extent with net glacier mass balances in Scandinavia and the European Alps showed that MODIS data at 250 m spatial resolution may be used as an indicator of net glacier mass balances in these areas. This close relationship should further be investigated in other regions within the Arctic circumpolar area to assess the potential of circumpolar

MODIS imagery to estimate glacier mass balances in more detail. In addition, the high-resolution MODIS data were employed to validate PSI extent in two commonly used land surface classifications (LSC) in 2000 and 2005. The clear misclassification observed in both LSCs for most ROIs is a potential source of error to be considered with regard to LSCs being used to set up boundary conditions in climate and land surface process models. A decade-long dataset covering the entire Arctic circumpolar area at high spatial resolution will be available for studies of long-term trends and changes, if MODIS continues to be operational until the end of 2009. This dataset will serve as a baseline for the derivation of other land surface parameters, such as albedo, land cover types, or vegetation properties at 250 m spatial resolution consistent with the GCOS requirements for ECVs.

In summary, the overall aim of the thesis — to revise the applicability of AVHRR and MODIS imagery for studies of land surface parameters in mountain regions on various spatial scales and to make a contribution to the understanding of sensitive mountain regions in the context of the global climate change discussion — was achieved.

Acknowledgements

Declaration

under Art. 28 Para. 2 RSL 05

Last, first name: Fontana, Fabio

Matriculation number: 00–105–981

Programme: PhD of Science in Climate Science

Bachelor ☐   Master ☐   Dissertation ☒

Thesis title: From single pixel to continental scale: using AVHRR and MODIS to study land surface parameters in mountain regions

Thesis supervisor: Dr. Stefan Wunderle

I hereby declare that this submission is my own work and that, to the best of my knowledge and belief, it contains no material previously published or written by another person, except where due acknowledgement has been made in the text. In accordance with academic rules and ethical conduct, I have fully cited and referenced all material and results that are not original to this work. I am well aware of the fact that, on the basis of Article 36 Paragraph 1 Letter o of the University Law of 5 September 1996, the Senate is entitled to deny the title awarded on the basis of this work if proven otherwise.

Bern, September 21, 2009

Fabio Fontana

Signature

Curriculum Vitae

Personal	Fabio Matteo Andrea Fontana	
	Austrasse 18, 3084 Wabern, Switzerland	
	Born November 18th, 1980 in Interlaken, Switzerland	

Education	since 2006	PhD student in Climate Sciences, Institute of Geography, University of Bern, Switzerland
	2000–2005	Student of Geography, Biology, and Earth Sciences, University of Bern, Switzerland
	1996–2000	Gymnasium, Interlaken, Switzerland
	1995–1996	Sekundarschule, Interlaken, Switzerland
	1987–1995	Primar- and Sekundarschule, Wengen, Switzerland

Student Exchange	2003–2004	Student of Climatology and Biology, University of Stockholm, Sweden

Internships	08/2008– 10/2008	Canada Centre for Remote Sensing (CCRS), Ottawa, Canada

Professional Experience	11/2005– 07/2006	Research assistant, Institute of Geography University of Bern, Switzerland
	11/2004– 03/2005	Undergraduate research assistant, Institute of Geography University of Bern, Switzerland